www.talentdetector.polsl.pl

TalentDetector

INTERNATIONAL
STUDENTS
SCIENTIFIC
CONFERENCE

ISBN 978-83-65138-46-0

www.talentdetector.polsl.pl

TalentDetector

INTERNATIONAL STUDENTS SCIENTIFIC CONFERENCE

26.09.2025 YANSHAN

ORGANIZERS:

- **Materials Science Circle** of the Association of Alumni of the Silesian University of Technology, Gliwice, Poland
- **Department of Engineering Materials and Biomaterials**
  Faculty of Mechanical Engineering
  Silesian University of Technology, Gliwice, Poland

80th ANNIVERSARY
Silesian University of Technology

TalentDetector

TalentDetector2025_Yanshan INTERNATIONAL STUDENTS SCIENTIFIC CONFERENCE

Scientific editor:
Mirosław Bonek

Department of Engineering Materials and Biomaterials,
Faculty of Mechanical Engineering,
Silesian University of Technology
26th September 2025
Gliwice, Poland

Katedra Materiałów
Inżynierskich i Biomedycznych

Katedra Materiałów Inżynierskich i Biomedycznych
Wydział Mechaniczny Technologiczny
Politechnika Śląska
ul. Konarskiego 18a, 44-100 Gliwice tel. +48 (32) 2371322

Redakcja techniczna i skład komputerowy:
dr h.c. dr hab. inż. Mirosław Bonek, prof. PŚ

Recenzenci:
Mirosław Bonek, Andrzej Jałowiecki, Anna Kiljan, Damian Krenczyk, Mariusz Król, Małgorzta Szymiczek

Materiały są opublikowane na podstawie oryginałów dostarczonych przez Autorów, zaopiniowanych przez Zespół Recenzentów.

Wydano za zgodą:
Kierownika Katedry Materiałów Inżynierskich i Biomedycznych
Wydziału Mechanicznego Technologicznego
Politechniki Śląskiej

Wydawca:
Katedra Materiałów Inżynierskich i Biomedycznych
Wydział Mechaniczny Technologiczny
Politechnika Śląska
Gliwice 2025

Seria wydawnicza:
Prace Katedry Materiałów Inżynierskich i Biomedycznych
Wydział Mechaniczny technologiczny
Politechnika Śląska
Publikacja: wrzesień 2025

ISBN 978-83-65138-46-0

INTERNATIONAL STUDENTS SCIENTIFIC CONFERENCE

TALENTDETECTOR2024_YANSHAN

SILESIAN UNIVERSITY OF TECHNOLOGY, GLIWICE, POLAND

26th SEPTEMBER 2025

The International Student Scientific Conference TalentDetector2025_Yanshan aims to integrate the student and scientific community dealing with topics related to material technologies. It is a place that gives the opportunity to exchange experiences, knowledge, skills and present current scientific achievements, developing and expanding students' interests in the field of materials engineering, surface engineering, biomaterials and biomedical engineering, nanotechnology, pro-ecological technologies and computer materials science. The conference allows for the presentation of projects conducted with the industry as part of the activities of Student Scientific Circles, doctorates, projects implemented in the form of PBL - Project Based Learning as part of the Excellence Initiative - Research University at the Silesian University of Technology, projects in the framework of EURECA PRO/European University in Responsible Consumption and Production and international bilateral cooperation between Universities.

CONFERENCE ORGANIZER

Materials Science Circle of the Association of Alumni of the Silesian University of Technology, Gliwice, Poland

CONFERENCE CO-ORGANIZER

Department of Engineering Materials and Biomaterials, Faculty of Mechanical Engineering, Silesian University of Technology, Gliwice, Poland

INTERNATIONAL SCIENTIFIC COMMETTEE

ORGANIZING COMMETTEE

TalentDetector HISTORY

The International Student Scientific Conferences TalentDetector from 12 edition (since 2018) have been a place for the exchange of experience, knowledge, skills and presentation of students' current scientific achievements in the field of materials engineering, surface engineering, biomaterials and biomedical engineering. As part of the conference, two international scientific monographs, TalentDetector_Summer and TalentDetector_Winter, are published annually, which already contain over 760 scientific articles resulting from the implementation of PBL, EURECA PRO, Students Scientific Cyrcles projects and projects with secondary school students with international authors. Participation in the form of presentations and posters in TalentDetector International Student Scientific Conferences allows members of the project teams to integrate the student and scientific community of the Silesian University of Technology as well as young staff from foreign research centres in Austria, China, Czech Republic, Ethiopia, Ghana, Georgia, Iran, Romania, Slovakia, Ukraine and Turkey, dealing with topics related to materials technologies.
Scientific monographs are prepared based on articles, mostly with international authors, reviewed by an international scientific committee.
The initiative of the cyclical organization of the International Student Scientific Conference TalentDetector significantly expands activities in the field of student education, organizational and popularization activities for the scientific community related to materials engineering at the national and international level.

Thanks to extensive international cooperation, over 250 articles were published free of charge.

Number of cooperating universities: 13

Gazi University, Ankara, Turkey
Gebze Technical University, Gebze, Turkey
Georgian Technical University, Tbilisi, Georgia
Khmelnitskyi National University, Khmelnitskyi, Ukraine
Laserinstitut Hochschule Mittweida, Mittweida, Germany
Pamukkale University, Denizli, Turkey
Silesian University of Technology, Gliwice, Poland
Slovak Technical University in Bratislava, Trnava, Slovakia
Technical University in Zvolen, Zvolen, Slovakia
University of Petroșani, Petroșani, Romania
University of Pristina, Pristina, Kosovo
University of Zilina, Zilina, Slovakia
Yanshan University, Qinhuangdao, China

The history of TalentDetector in numbers:

2018
TalentDetector 2019 (Gliwice)
Number of articles: 59
Number of authors: 206
Number of countries: 1

2021
TalentDetector2021_Winter (Gliwice)
Number of articles: 37
Number of authors: 134
Number of countries: 2

TalentDetector2021_Summer (Zawiercie)
Number of articles: 57
Number of authors: 173
Number of countries: 3

2022
TalentDetector2022_Winter (Gliwice)
Number of articles: 79
Number of authors: 179
Number of countries: 4

TalentDetector2022_Summer (Wisła)
Number of articles: 79
Number of authors: 176
Number of countries: 4

2023
TalentDetector2023_Winter (Gliwice)
Number of articles: 73
Number of authors: 143
Number of countries: 6

TalentDetector2023_Summer (Brenna)
Number of articles: 105
Number of authors: 173
Number of countries: 9

2024
TalentDetector2024_Winter (Gliwice)
Number of articles: 82
Number of authors: 135
Number of countries: 7

TalentDetector2024_Summer (Gliwice-Zilina)
Number of articles: 84
Number of authors: 147
Number of countries: 8

2025
TalentDetector2025_Winter (Gliwice)
Number of articles: 95
Number of authors: 173
Number of countries: 9

TalentDetector2025_Summer (Brenna)
Number of articles: 87
Number of authors: 143
Number of countries: 10

TalentDetector2025_Yanshan (Gliwice)
Number of articles: 12
Number of authors: 29
Number of countries: 1

SUMMER CAMP 2025 IN THE FACULTY OF MECHANICAL ENGINEERING, SILESIAN UNIVERSITY OF TECHNOLOGY FOR STUDENTS FROM YANSHAN UNIVERSITY

On July 3, 2025, the Faculty of Mechanical Engineering of the Silesian University of Technology proudly hosted the official opening ceremony of Summer Camp 2025, welcoming a group of students from Yanshan University, China.
The event was attended by the Faculty authorities: Dean Professor Marcin Adamiak, Vice-Deans Professor Mirosław Bonek DrHC, Professor Małgorzata Szymiczek, and Professor Damian Krenczyk, as well as members of the academic staff.
This year's edition of Summer Camp is the result of a fruitful collaboration between the Silesian University of Technology and Yanshan University, which has been developing since 2021. This partnership fosters academic exchange and the development of joint research between the Mechanical Faculties of both institutions.
We are pleased to host 30 postgraduate students from the Faculty of Mechanical Engineering at Yanshan University, who will spend three exciting months in Poland, participating in lectures, laboratory classes, workshops, and study visits to Polish industrial companies. In addition, they will enjoy a rich cultural and social program designed to help them discover Poland and its people.

Summer Camp 2025 is not only about science — it is about building bridges between cultures and shaping the future of engineering together.

Within three months, an intensive academic and practical training block was carried out for Summer Camp participants from Yanshan University at the Faculty of Mechanical Engineering and Technology of the Silesian University of Technology. Participants took part in six specialized courses combining modern engineering knowledge with hands-on laboratory, project-based work and two trainings at industrial companies (Dream solutions s.c. and EMT-Systems Sp. z o.o.).

The program included the following thematic modules:

Andrzej Jałowiecki, PhD Eng. – Introduction to Mobile Robotics
This course focused on the fundamentals of designing and programming mobile robots. Students learned C++ programming, developed control algorithms, and built their own robot platforms in modern laboratories at the Centre for New Technologies.

Mariusz Król, PhD Eng. – Materials of the Future
Students were introduced to 3D design using Solidworks software and gained practical experience in rapid prototyping technologies, including 3D printing, to create mechanical components based on their own designs.

Prof. Damian Krenczyk, DSc Eng.– Applied Simulation Modelling of Production and Logistics Processes Using FlexSim

This course covered the basics of modeling and simulation of production and logistics processes using FlexSim software. Students worked with 3D objects, developed transport networks, and analyzed simulation outcomes using visualization tools and dashboards.

Prof. Małgorzata Szymiczek, DSc Eng. – Methods of Shaping Polymer and Metal Materials

The course provided theoretical and practical knowledge in the field of polymer engineering and metal forming technologies. Topics included polymer processing methods (e.g., injection molding, extrusion, vacuum forming) and plastic deformation techniques for metals such as rolling, forging, bending, and stamping.

Dr. Anna Kiljan - Industry 4.0. and new technologies with circle economy and green environment

During the classes, students learn about modern technologies used in industry. Technologies of Industry 4.0, like: cybersecurity, Internet of Things, Cloud Computing, Printing 3D, Simulation on production lines, Virtual Technology etc. Additionally, they familiarized themselves with new standards and procedures for the green economy, with particular emphasis on ESG requirements. They also gained knowledge of soft skills and the new Engineer 4.0 competencies. The classes will be held in a modern laboratory prepared by an external company at the Center for New Technologies.

Prof. Mirosław Bonek, DrHC - Advanced surface engineering

The aim of the course is to develop concepts, learning patterns and systematizing knowledge of laser surface treatment, vocational skills to find appropriate technological solutions, teaching ways of solving research problems and thinking in terms of technical through laboratory exercises, training the students' ability to apply theoretical knowledge in practice. During the course, lectures were held on the physical basics of laser radiation production, laser construction and operation. The technology of forming the structure and surface properties of engineering materials using laser radiation. General classification of coating technology and welding methods. The surface layers formed using laser technology. Surface engineering technologies for formation the structure and properties of the surface layers of machine parts.

In addition to academic activities, students had the opportunity to explore the Silesian University of Technology campus, visit the laboratories of the Faculty of Mechanical Engineering and Technology, and discover the most beautiful spots in the city of Gliwice and Silesian Voivodeship.

TalentDetector

26th September 2025
Gliwice, Poland

FACULTY OF MECHANICAL ENGINEERING
SILESIAN UNIVERSITY OF TECHNOLOGY

INTERNATIONAL STUDENTS SCIENTIFIC CONFERENCE

Contents

TalentDetector
26th September 2025
Gliwice, Poland
FACULTY OF MECHANICAL ENGINEERING
SILESIAN UNIVERSITY OF TECHNOLOGY
INTERNATIONAL STUDENTS SCIENTIFIC CONFERENCE

Metal part forming based on selective laser melting technology

Yaqian Hu[a], Yiying Wang[a]

[a] School of Mechanical Engineering, Yanshan University, Qinhuangdao, China
email: hyaqian@126.com

Abstract: In the manufacturing of overhanging parts using selective laser melting (SLM) technology, the selection of support structures has a crucial impact on the forming quality. This paper proposes a combined support structure and systematically investigates the effects of different support structures on the warpage deformation, surface morphology, microstructure, and microhardness of the specimens. The research results show that the heat dissipation performance of block supports is superior to that of conical supports. For the combined support, increasing the proportion of the block structure can effectively improve the forming accuracy and mechanical properties of the specimens, while increasing the proportion of the conical structure is more conducive to suppressing the warpage of the specimens. This study can provide a theoretical basis and practical reference for the optimal design of support structures in the overhanging regions of metal parts.

Keywords: selective laser melting, support structure, process parameters

1. INTRODUCTION

As one of the most widely used metal additive manufacturing technologies, selective laser melting (SLM) has been extensively applied in the fabrication of high-performance parts in fields such as military industry, aerospace, medical care, and automotive engineering [1-2]. This technology exhibits significant advantages in the rapid manufacturing of complex parts with topological structures and lattices [3-5]. However, the SLM forming process is subject to the overhang angle constraint [6-7], requiring the addition of appropriate support structures on the lower surface of overhanging features. These support structures serve to timely dissipate the heat generated during the sintering of overhanging regions, suppress the deformation of overhanging features, and thereby improve the forming quality of overhanging surfaces.

Currently, the commonly used support structures in SLM technology mainly include block supports, planar supports, tree-like supports, and conical supports. Among them, block supports are the most widely used due to their strong applicability [8-10]. Domestic and foreign studies on support structures have mostly focused on structural optimization and strength characteristics. Leary et al. [11] conducted mechanical strength tests on block support structures prepared by SLM and found that the strength of the support structure is inversely proportional to its height, and both the heat transfer capacity and support strength gradually

increase with the decrease of support spacing. Arman et al. [12] studied the influence of design parameters of block supports on part deformation, and through sensitivity analysis, it was shown that the contact area between the support and the part has a significant impact on the deformation of the overhanging structure. Schmidt et al. [13] systematically explored the effect of conical support structures on the support region and clarified the relationship between the support area and microhardness, molten pool geometry, and deformation.

Existing studies have mostly focused on the design optimization of a single support structure, and the selection of support types in practical applications still relies on empirical judgment. Issues such as the performance differences between different support structures, how to achieve precise selection based on part characteristics to improve support utilization and forming quality, still lack systematic research. Based on this, this paper explores the influence of different support structures on the forming accuracy, specimen warpage, surface morphology, microstructure, and hardness of overhanging regions through SLM experiments, clarifies the support selection principles, and provides a reference for the support selection of overhanging regions in metal parts.

2. DESIFN OF SUPPORT STRUCTURES

The metal part, as shown in Figure 1, has an overhanging surface with an angle exceeding 45°.

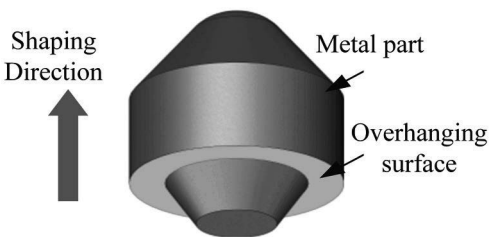

Figure 1. Overhanging surface of metal parts

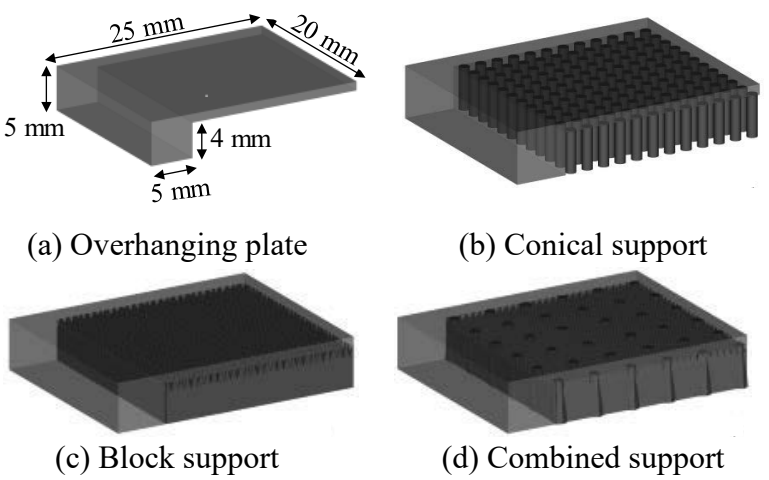

Figure 2. Overhanging plate and three types of support structures

Due to the inherent constraints of the SLM manufacturing process, it is necessary to add an appropriate support structure at the lower end of the overhanging surface of the part to support the molten pool in the overhanging area and suppress part deformation. For this purpose, this paper designs an overhanging plate and three types of support structures, aiming to explore the influence law of support types on the forming quality of the overhanging area of the part. The models of the three support structures are shown in Figure 2(b)-(d) respectively, among which the combined support is composed of a block structure and a conical structure. Taking the block support as the design benchmark, the support spacing of the three specimens is uniformly set to d=0.70 mm. The specific design parameters of the three support structures are detailed in Table 1.

Table 1. Design parameters of three support structures

Support type		Support spacing (mm)	Wall thickness (mm)	Contact area (mm^2)
Conical support		0.70	Φ1.00	113.10
Block support		0.70	0.20	53.19
Combined support	Conical structure	1.50	Φ1.00	59.63
	Block structure	0.70	0.10	

3. EXPERIMENTS AND RESULTS

3.1. Characterization of microstructural properties

In the process of SLM processing, the material used is spherical 316L stainless steel powder with an average particle size of 30 μm. The processing parameters are set as follows: the laser power in the solid region is 150 W, and that in the support region is 70 W; the scanning speed for the solid region is 800 mm/s, and for the support region is 900 mm/s; the scanning spacing and layer thickness are set to 0.08 mm and 0.02 mm respectively, and the substrate temperature is controlled at 22 ℃.

After the specimens are printed, they undergo wire-cutting to remove overhanging support, followed by standard metallographic grinding, polishing, and etching with Keller's reagent. Support surface roughness is measured via laser scanning confocal microscope LSM700; post-removal lower surface morphology/structure via scanning electron microscope ULTRA55; support-specimen junction features via optical microscope Axio Imager.M2m; microstructure and element distribution via electron probe microanalyzer EMPA 1720 and ULTRA55. Side hardness (Tukon2500) is tested at 7 vertical points, with a point spacing of 0.10 mm, a loading force of 100 g, and a holding time of 20 s.

3.2. Deformation analysis

Three SLM-fabricated support specimens are shown in Figure 3. Conical and combined support specimens exhibit good forming quality, while block support specimens have obvious defects, with fractures at the support-overhanging plate contact. This arises from the block

support's thin walls, insufficient strength, and resultant edge support rupture. Post-support removal, overhanging region deformation measurements revealed varying warpage: the conical support specimen, with a 59.82 mm² larger contact area than the block support specimen, had 1 mm less deformation; the combined support specimen showed the smallest deformation (0.29 mm).

Combined support better inhibits edge warpage than conical support, verifying the block support's role in reducing thermal strain. Meanwhile, the conical support specimen's smaller warpage than the block support specimen indicates its thicker walls and larger contact area enhance support strength, effectively suppressing thermal strain-induced edge warpage. Thus, considering reduced thermal strain and improved support strength, combined support more effectively inhibits overhanging specimen warpage.

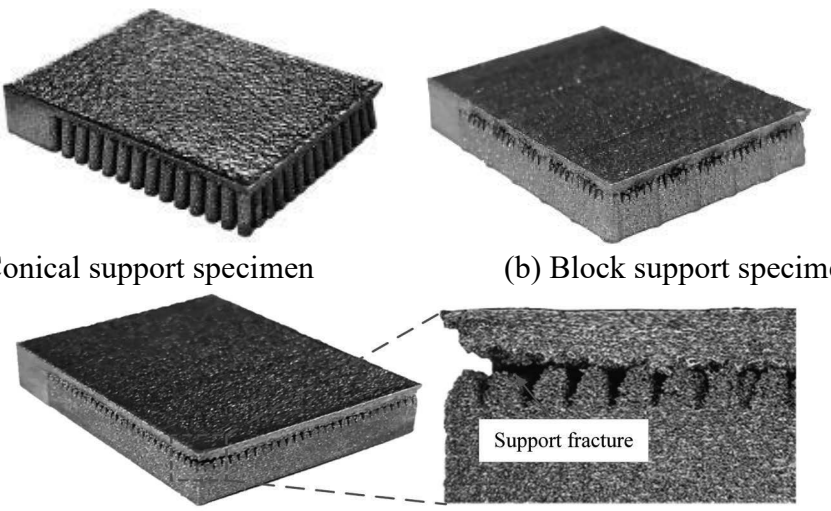

(a) Conical support specimen (b) Block support specimen

(c) Combined support specimen

Figure 3. SLM formed specimens

3.3. Surface morphology analysis

After support removal, SEM images of the overhanging area's lower surface in Figure 4 show abundant unmelted metal powders bonded in all three support structures' gaps. This occurs because loose powders fill the space below the overhanging region during SLM; residual heat from laser penetration melts particle surfaces, causing adjacent particles to bond. Comparing powder bonding reveals conical support specimens have larger unmelted powder clusters with distinct melting traces, while block and combined support specimens show similar smaller clusters from surface melting. This difference stems from conical supports' poor heat dissipation, trapping laser-generated heat and forming more/larger clusters.

The 3D topographic profiles of the lower surface of the specimens after support removal are shown in Figure 5. They indicate conical supports have the largest surface roughness (80.52 μm), followed by block (73.08 μm) and combined supports (70.80 μm). Thus, block and combined supports reduce roughness by minimizing powder clusters. For 316L stainless steel overhangs using combined supports, increasing the block structure proportion improves surface accuracy further.

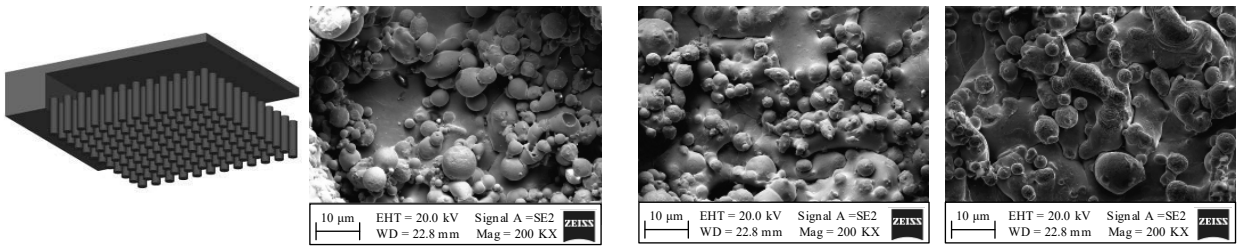

(a) Observation area (b) Conical support (c) Block support (d) Combined support

Figure 4. SEM images of the lower surfaces of different specimens after removal of the supports

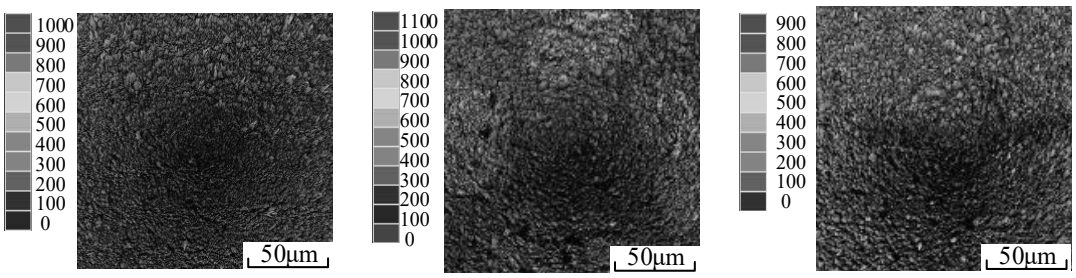

(a) Conical support specimen (b) Block support specimen (c) Combined support specimen

Figure 5. 3D topographic profiles of the lower surfaces of different specimens after removal of the supports

3.4. Microstructure analysis

Metallographic observation of the overhanging region above support gaps is shown in Figure 6(a). Structures in Figure 6(b)-(d)) shows conical support specimens have coarse, uniformly distributed grains (42.15 μm). In contrast, the block support specimen and the combined support specimen have finer grain sizes (18.42 μm). With increasing forming height, grain competitive growth intensifies, causing more distinct morphological differences and local defects.

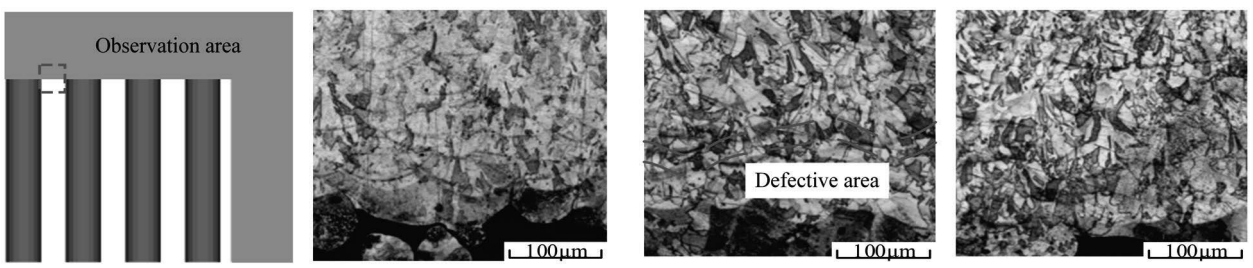

(a) Observation area (b) Conical support (c) Block support (d) Combined support

Figure 6 Metallographic images of specimens with different support

Metallographic differences arise from varying molten pool solidification thermodynamics. Block supports' superior heat dissipation creates larger temperature gradients and faster cooling, promoting finer grains and denser structures, beneficial for overhanging part performance. In Figure 7, further SEM scanning of block support defects reveals abundant pores at molten layer junctions, caused by rapid cooling trapping gas in the molten pool. These

pores reduce mechanical properties, so post-processing to remove overhanging bottom defects is needed when using block supports.

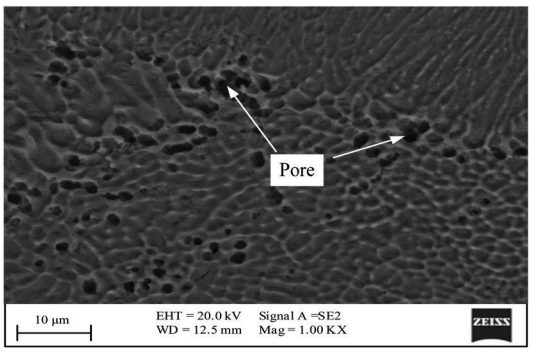

Figure 7. SEM image of the defect area of the block support specimen

In addition, a network-like subgrain structure is observed within grains. Qualitative point analysis of subgrain boundary elements show slightly higher Cr and Ni mass fractions than in 316L powder, indicating possible enrichment. In Figure 8, further surface scanning reveal uneven Cr and Ni distribution; these Fe-heavier elements segregate at subgrain boundaries, forming a network-like alloy phase. This arises from 316L's rapid solidification during SLM, where slow diffusion of large-atom alloying elements causes compositional fluctuations, leading to their enrichment along subgrain boundaries as network phases (e.g., Cr, Ni), potentially reducing fracture strength.

Support structures influence metal solidification, defects, and element microdistribution via cooling conditions. Block supports notably enhance structural performance; adjusting their proportion in combined supports enables overhanging structures to achieve superior metal microstructures.

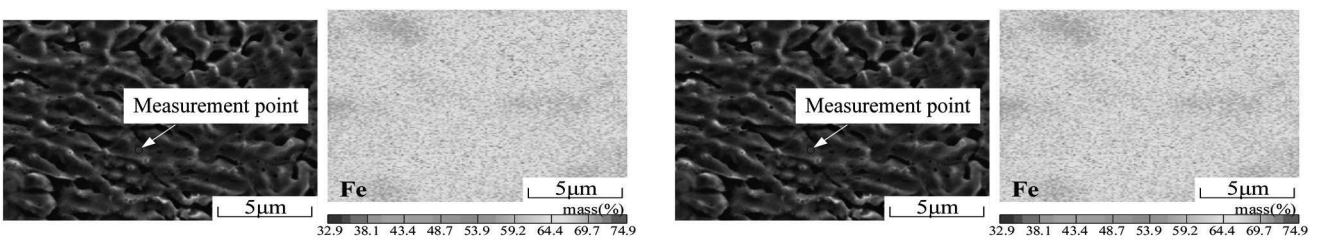

(a) Measurement point (b) Distribution of Fe (c) Distribution of Cr (d) Distribution of Ni

Figure 8. Microstructures of 316L

3.5. Microhardness analysis

Figure 9 shows microhardness vs. forming height for SLM specimens. All three support types exhibit increasing hardness with height: conical supports show the gentlest rise and smallest fluctuation ($8HV_{0.1}$), followed by combined supports ($19HV_{0.1}$); block supports have the largest fluctuation ($22HV_{0.1}$) due to bottom defects. Peak hardness is $229HV_{0.1}$ for conical supports and $234HV_{0.1}$ for combined supports.

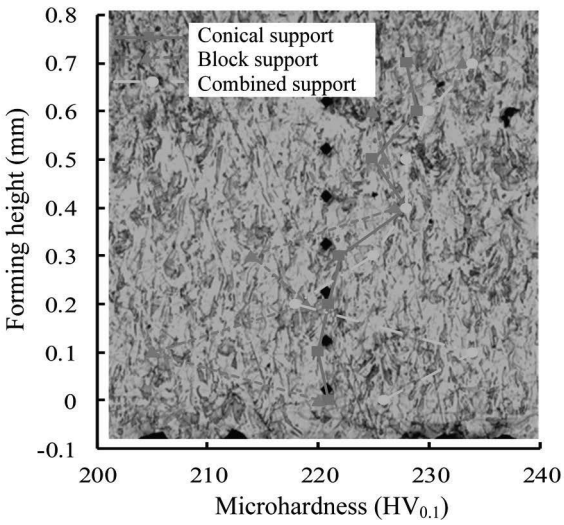

Figure 9. The curve of the microhardness vs. forming height for SLM specimens

Support type affects hardness via two mechanisms: (1) Cr/Ni segregation at subgrain boundaries forms dense brittle-hard network phases, enhancing hardness; (2) higher cooling rates induce complex dislocation networks and fine grains, hindering indentation migration and increasing hardness. The combined support offers superior comprehensive performance. Increasing its block structure proportion enhances overhanging region hardness and mechanical properties, while raising the conical structure proportion reduces bottom defects.

4. CONCLUSION

A systematic analysis was conducted on the effects of different support structures on the surface morphology, microstructure, and microhardness of specimens during SLM forming, and the intrinsic mechanisms underlying the differences in support performance are explored in depth. The combined support is preferred as the support structure for the overhanging surface, which can fabricate overhanging parts with higher dimensional accuracy. By adjusting the proportion of different structures in the combined support, the regulation of the structure morphology, defects, and composition distribution can be realized, thereby improving the structural performance of the metal part. Therefore, the combined support has more excellent comprehensive performance. Only a small machining allowance needs to be set to remove defects, reducing material waste. This provides a technical reference for the selection of support structures in actual production.

BIBLIOGRAPHY

1. B.V. Efremenko, V.I. Zurnadzhy, Y.G. Chabak, et al., A comparison study on the effect of counter ball material on sliding wear response of SLM-printed biomedical 316L steel, Materials Today: Proceedings (2022) 2214-7853.
2. Y. Yu, Q.Y. Tan, B. Michael, et al., Laser additive manufacturing of steels, international materials reviews 67(5) (2022) 487-573.

3. L. Yan, X. Zhang, Q. Fu, et al., Assembly-level topology optimization and additive manufacturing of aluminum alloy primary mirrors, Optics Express 30 (2022) 6258.
4. D. Delissen, E. Boots, D. Laro, et al., Realization and assessment of metal additive manufacturing and topology optimization for high-precision motion systems, Additive Manufacturing 58 (2022) 103012.
5. G. Kadir, R. Craig, K. Zafer, Energy absorption enhancement of additively manufactured hexagonal and reentrant (auxetic) lattice structures by using multi-material reinforcements, Additive Manufacturing 59 (2022) 103076.
6. J.C. Jiang, X. Xu, S. Jonathan, Support structures for additive manufacturing: a review, Journal of Manufacturing and Materials Processing 2(4) (2018) 64.
7. L. Yuan, Z.X. Pan, D.H. Ding, et al., Fabrication of metallic parts with overhanging structures using the robotic wire arc additive manufacturing, Journal of Manufacturing Processes 63 (2021) 24-34.
8. M. Mele, A. Bergmann, G. Campana, et al., Experimental investigation into the effect of supports and overhangs on accuracy and roughness in laser powder bed fusion, Optics & Laser Technology 140 (2021) 107024.
9. S.E. Messele, State-of-the-art of selective laser melting process: a comprehensive review, Journal of Manufacturing Systems 63 (2022) 250-274.
10. L. Zhu, R.L. Feng, J.T. Xi, et al., A lightweight design of tree-shaped support structures for SLM additive manufacturing, Computer-Aided Design and Applications 17(4) (2019) 716-726.
11. M. Leary, T. Maconachie, A. Sarker, et al., Mechanical and thermal characterisation of AlSi10Mg SLM block support structures, Materials & Design 183 (2019) 108138.
12. K. Arman, F.F. Mehr, S. Cockcroft, et al., The role of block-type support structure design on the thermal field and deformation in components fabricated by laser powder bed fusion, Additive Manufacturing 51 (2022) 102644.
13. M. Schmidt, S. Greco, D. Müller, et al., Support structure impact in laser-based powder bed fusion of AlSi10Mg, ScienceDirect 108 (2022) 88-93.

TalentDetector
26th September 2025
Gliwice, Poland
FACULTY OF MECHANICAL ENGINEERING
SILESIAN UNIVERSITY OF TECHNOLOGY
INTERNATIONAL STUDENTS SCIENTIFIC CONFERENCE

Sharpening with Light: An Introduction to Laser Dressing of Grinding Wheels

Tianyuan Jiang [a], Qihang Lu [b]

[a] .Department of Mechanical Design, School of Mechanical Engineering, Yanshan University
email:jiangtianyuan92@gmail.com
[b] .Department of Mechatronic Design, School of Mechanical Engineering, Yanshan University

Abstract: Grinding wheels are essential tools in precision manufacturing, but their performance degrades over time due to glazing and loading. Traditional mechanical dressing methods, while effective, suffer from tool wear, low efficiency, and limitations when applied to superabrasive wheels like diamond or cubic boron nitride (CBN). Laser dressing emerges as a non-contact, thermal-based alternative that uses high-energy laser beams to remove bond material, expose fresh abrasive grains, and sharpen the wheel surface. This paper provides an introduction to laser dressing, covering its principles, methods, advantages, experimental verification, and results. Drawing from recent reviews and studies, we demonstrate how laser dressing improves grinding efficiency, reduces forces, and enhances surface quality. Experimental data from pulsed fiber laser setups show optimal power densities for effective truing and sharpening, achieving up to 80-88% efficiency. The feasibility of this process is validated through simulations and tests on bronze-bonded diamond wheels, highlighting its potential for industrial applications while addressing challenges like thermal damage.

Keywords: Laser dressing; Grinding wheels; Superabrasive; Truing; Sharpening; Pulsed laser

1. INTRODUCTION

Grinding is a critical abrasive machining process used in industries such as aerospace, automotive, and tool manufacturing to achieve high-precision surfaces with tight tolerances [1]. As grinding progresses, the wheel surface becomes loaded with workpiece debris and the abrasive grains dull, leading to increased forces, poor surface finish, and reduced efficiency. Dressing restores the wheel's cutting ability by removing worn grains and bond material, exposing sharp new abrasives.

Traditional dressing methods, including single-point diamond dressing, rotary dressing, and abrasive block dressing, rely on mechanical contact [2]. These approaches are effective for conventional wheels but face challenges with superabrasive wheels (e.g., diamond or CBN bonded with metal, resin, or vitrified materials). Issues include high dresser wear, low dressing efficiency (30-70%), and environmental concerns from coolant usage or debris [3,4]. For

instance, mechanical dressing of metal-bonded diamond wheels can lead to rapid tool degradation due to the bond's toughness [5].

In response, non-traditional methods like electrical discharge dressing (EDD), electrolytic in-process dressing (ELID), and laser dressing have been developed. Laser dressing, first explored in the late 1980s for alumina wheels, uses focused laser energy to thermally ablate the bond and sharpen grains without physical contact [6]. This method is particularly advantageous for superabrasives, offering precision, repeatability, and minimal tool wear. Recent advancements, such as pulsed Nd:YAG and fiber lasers, have expanded its application to fine-grained metal-bonded wheels, improving profile accuracy and surface quality [7,8].

This paper introduces laser dressing, drawing parallels to innovative manufacturing processes like continuous fiber winding in space truss structures, where precise material manipulation is key. We discuss principles, methods, advantages, experimental setups, results, and future prospects, aiming to provide a foundational understanding for researchers and practitioners.

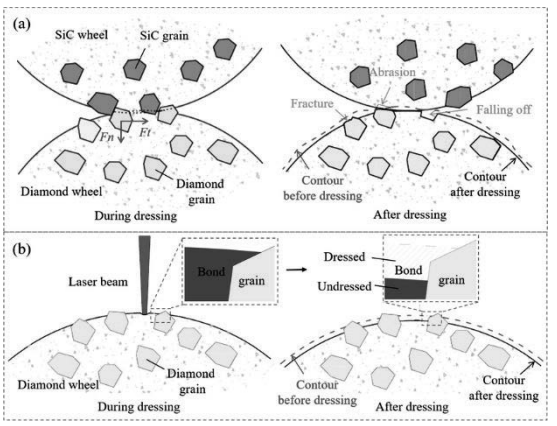

Figure 1. Schematic diagram of the laser dressing principle

2. PRINCIPLES OF LASER DRESSING

Laser dressing operates on thermal principles, where a high-intensity laser beam interacts with the grinding wheel's bond and abrasive materials. The laser energy causes localized heating, leading to melting, vaporization, or ablation of the bond (e.g., bronze, vitrified, or resin), while ideally preserving the integrity of harder abrasive grains like diamond or CBN [9].

The key mechanism is photothermal ablation: the laser's photon energy is absorbed, converting to heat that exceeds the bond's melting or vaporization point (e.g., ~1000-2000°C for metal bonds). For diamond grains, which have high thermal conductivity (~2000 W/m·K), the process must be controlled to avoid graphitization (conversion to graphite at >700°C in air). Pulsed lasers are preferred as they deliver energy in short bursts (ns to μs), minimizing heat-affected zones (HAZ) and thermal damage.

Material removal rate (MRR) depends on laser parameters: power density (W/cm²), pulse duration, frequency, and scan speed. For example, a power density of 1.68 × 10^8 W/cm² gasifies bronze bonds, while 2.52 × 10^8 W/cm² trues diamond grains. Theoretical models, such as Fourier heat transfer equations, predict temperature fields and groove geometries, validated by experiments showing agreement within 10-15% error.

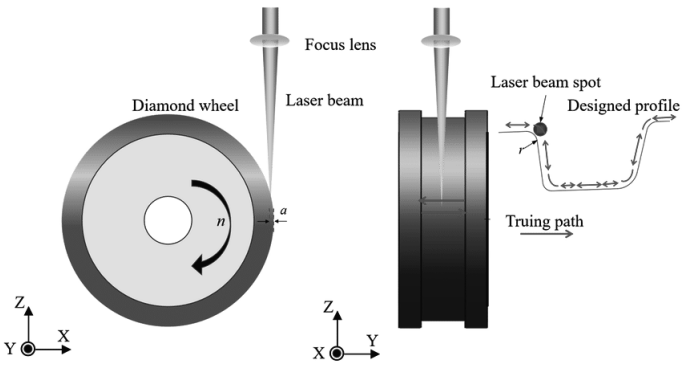

Figure 2. Thermal effect of laser interaction with grinding wheel material

Compared to mechanical methods, laser dressing is force-free, enabling micro-structuring (e.g., textured surfaces for better coolant flow). However, challenges include plasma shielding (reducing efficiency) and potential grain cracks at excessive powers.

3. METHODS OF LASER DRESSING

Laser dressing methods vary by laser type, incidence angle, and integration with other processes.

3.1 Tangential and Radial Laser Dressing

In tangential dressing, the beam scans parallel to the wheel surface, removing bond layer-by-layer for sharpening. Radial dressing involves perpendicular incidence with a set depth (e.g., 20-50 μm per pass) for truing profiles. Pulsed Nd:YAG lasers (wavelength 1064 nm, pulse width 210 ns) are common, with overlap ratios (80-90%) ensuring uniform coverage [10].

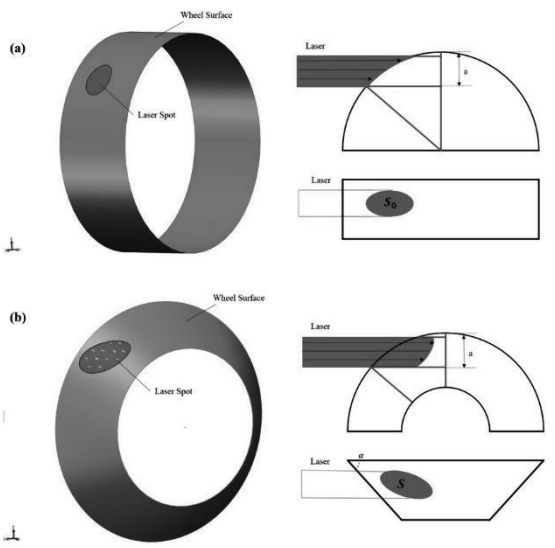

Figure 3. Comparison of laser paths in tangential and radial dressing

3.2. Laser-Assisted and Hybrid Methods

Laser-assisted dressing combines laser heating with mechanical tools, softening the bond for easier removal. Hybrid methods, like mechanical-laser combinations, achieve higher precision for concave surfaces [11]. Fiber lasers offer advantages in beam quality and efficiency, with powers up to 100 W.

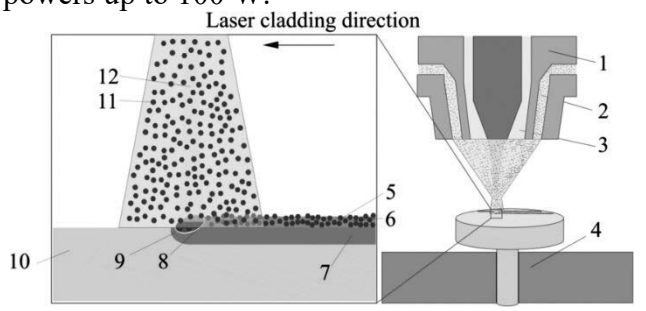

Figure 4. Schematic of the laser-assisted dressing device

3.3. Parameter Selection

Optimal parameters include power density (2-6 × 10^7 W/cm²), scan speed (1-5 mm/s), and focal offset (±0.5 mm) [12]. Protective atmospheres (e.g., argon) prevent oxidation. For fine-grained wheels, deflection nanosecond pulses improve profile accuracy to <5 μm runout.

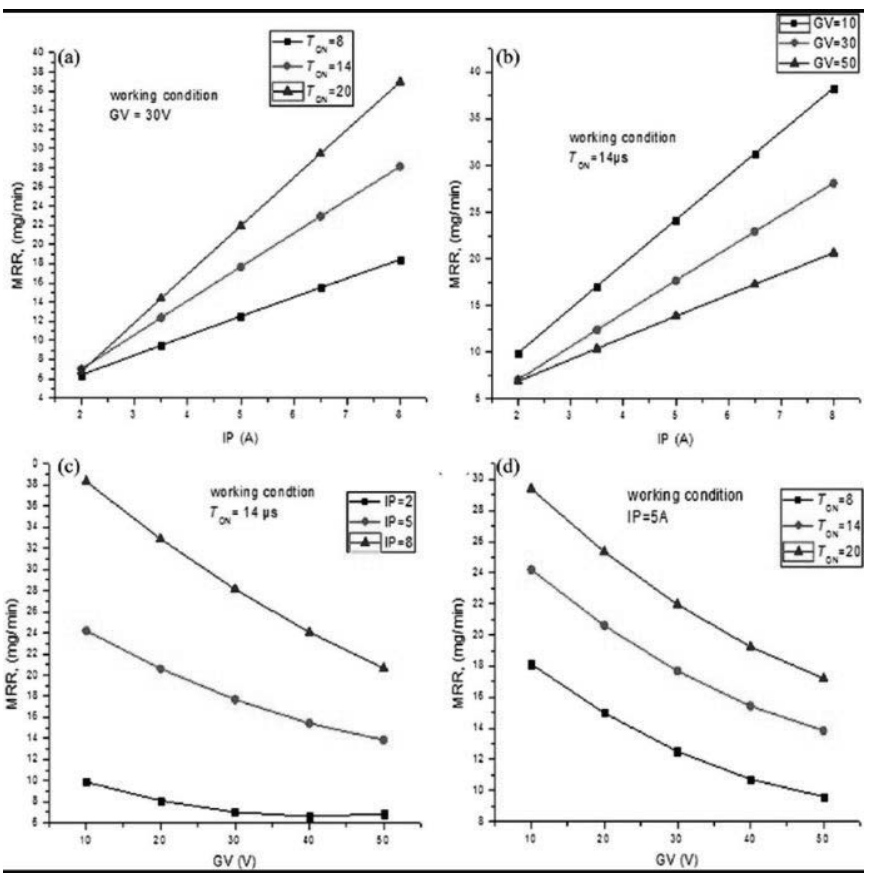

Figure 5. Effect of process parameters on material removal rate (MRR)n

4. EXPERIMENTAL VERIFICATION

Laser dressing experiments typically use a pulsed fiber laser and a 3D translation stage, with tools like infrared cameras and SEM for analysis [20]. One study dressed bronze-bonded diamond wheels (80-100 μm grain size) with a 1064 nm laser at 50 kHz, testing power densities from 1.68 × 10^8 to 3.36 × 10^8 W/cm². Grinding tests on Ti-6Al-4V measured forces and roughness. Another setup used Nd:YAG lasers for alumina wheels, with simulations validating temperature predictions.

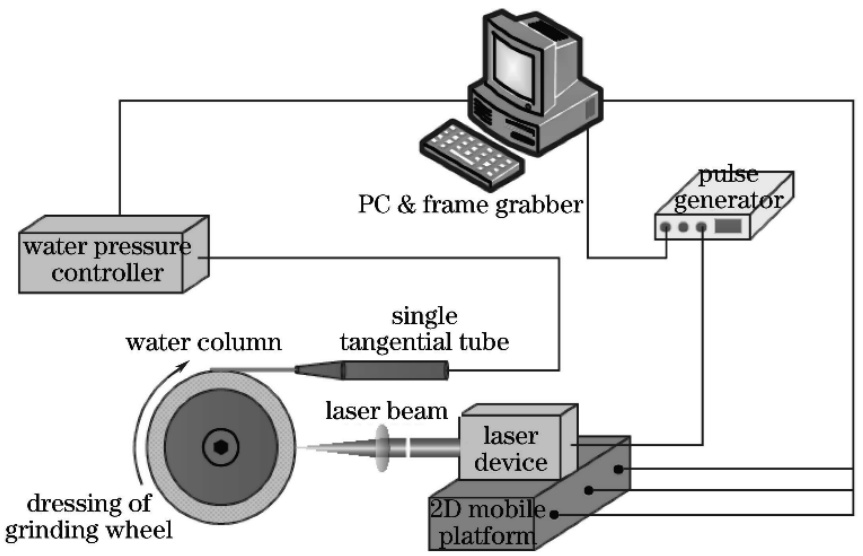

Figure 6. Experimental platform for laser-assisted dressing

5. RESULTS AND DISCUSSION

Results indicate laser dressing significantly enhances wheel performance. Grain protrusion height increased to 80-90 μm (vs. 50-60 μm mechanically), reducing FN by 20% and FT by 7%. Surface roughness improved by 35-40%, and grinding ratio rose 3-5 times [13,14].

At optimal power (2.52-3.36 × 10^8 W/cm²), effective bond removal and grain sharpening occurred without cracks, achieving 70-80% truing efficiency and 80-88% sharpening efficiency—superior to mechanical (30-65%) and EDM (50-70%). However, higher densities caused graphitization, emphasizing parameter control [15-18].

Thermal models matched experimental grooves (error <10%), confirming predictability [19]. For fine-grained wheels, laser-dressed surfaces showed better quality than mechanical, with profile accuracy <5 μm.

Challenges include thermal damage and cost, but advantages like no tool wear and eco-friendliness outweigh them for high-value applications.

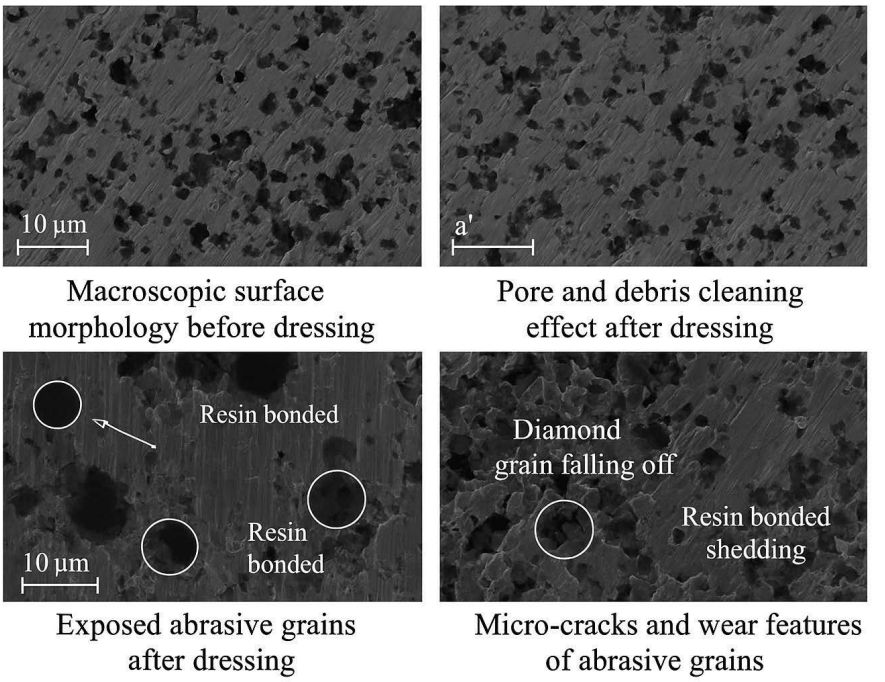

Figure 7. (Comparison of Grinding Wheel Morphology Before and After Dressing) Microscopic Morphology Comparison Photographs

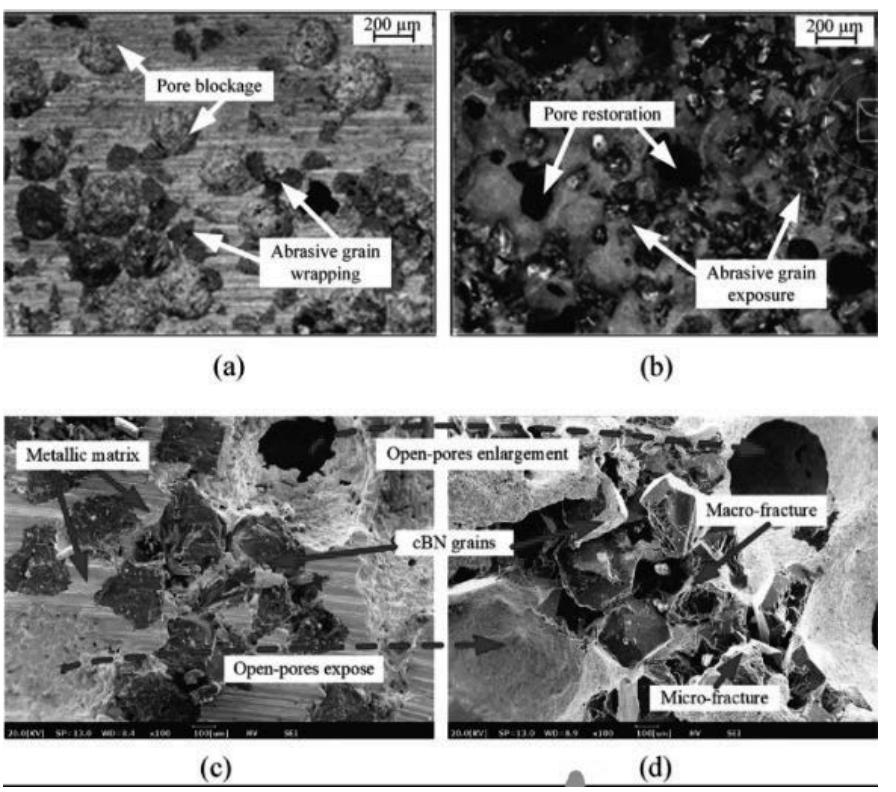

Figure 8. Variation of Grinding Force and Surface Roughness

6. CONCLUSION

Laser dressing represents a transformative approach to grinding wheel maintenance, offering non-contact precision and efficiency for superabrasive tools [2]. By leveraging thermal ablation, it achieves superior topography, reduced forces, and improved grinding outcomes, as validated through experiments on diamond wheels [12]. Optimal parameters (e.g., 2.52 × 10^8 W/cm² power density) ensure effective truing and sharpening without damage. Future developments may integrate AI for parameter optimization and hybrid methods for broader applicability. This technology not only addresses limitations of traditional methods but also supports sustainable manufacturing, akin to advanced processes in other fields.

BIBLIOGRAPHY

1. Mukhopadhyay, M., & Kundu, P. K. (2018). Laser dressing of grinding wheels - A review. International Journal of Mechatronics and Manufacturing Systems, 11(2-3), 173-197. https://doi.org/10.1504/IJMMS.2018.092847
2. Zhou, W., Tang, J., & Chen, H. (2019). Dressing methods of superabrasive grinding wheels: A review. Journal of Manufacturing Processes, 45, 46-69. https://doi.org/10.1016/j.jmapro.2019.06.027
3. Wang, J., Zhang, X., & Yu, T. (2022). Research and Progress on Truing and Sharpening Process of Diamond Abrasive Grinding Tools. Applied Sciences, 12(9), 4683. https://doi.org/10.3390/app12094683
4. Wegener, K., Hoffmeister, H.-W., & Karpuschewski, B. (2011). Conditioning and monitoring of grinding wheels. CIRP Annals, 60(2), 757-777. https://doi.org/10.1016/j.cirp.2011.06.003
5. Deng, H., & Xu, Z. (2019). Dressing of grinding wheels with laser and its effect on grinding performance. Precision Engineering, 59, 1-10. https://doi.org/10.1016/j.precisioneng.2019.05.005
6. Chen, G., Mei, L., & Yu, B. (2017). Modeling and simulation of laser dressing for superabrasive grinding wheels. Journal of Materials Processing Technology, 247, 104-114. https://doi.org/10.1016/j.jmatprotec.2017.04.012
7. Zhang, C., & Shin, Y. C. (2003). Laser-assisted truing and dressing of diamond wheels for precision grinding. Journal of Manufacturing Science and Engineering, 125(3), 575-580. https://doi.org/10.1115/1.1581887
8. Xie, J., Wei, F., & Zheng, J. (2015). Laser dressing of fine-grained bronze-bonded diamond grinding wheels. International Journal of Advanced Manufacturing Technology, 80(5-8), 1207-1214. https://doi.org/10.1007/s00170-015-7123-5
9. Deng, H., & Xu, Z. (2020). Optimization of laser dressing parameters for superabrasive grinding wheels. Optics and Laser Technology, 126, 106108. https://doi.org/10.1016/j.optlastec.2020.106108
10. Dinesh, S., Senthilkumar, M., & Rajagopal, K. (2014). A theoretical and experimental study on the pulsed laser dressing of bronze-bonded diamond grinding wheels. Applied Surface Science, 314, 78-89. https://doi.org/10.1016/j.apsusc.2014.06.165
11. Azarhoushang, B., & Daneshi, A. (2017). Environmental impacts of grinding wheel dressing methods: A comparative study. Procedia CIRP, 63, 465-470. https://doi.org/10.1016/j.procir.2017.03.112

12. Klocke, F., & Linke, B. (2008). Mechanisms and modeling of grinding wheel wear and dressing. Production Engineering, 2(4), 349-356. https://doi.org/10.1007/s11740-008-0112-5
13. Chen, J., & Xu, L. (2021). Experimental study on laser dressing of CBN grinding wheels for high-precision applications. Journal of Laser Applications, 33(1), 012015. https://doi.org/10.2351/7.0000315
14. Ding, W., Zhang, L., & Li, Z. (2017). Review on grinding wheel dressing technologies for high-efficiency grinding. International Journal of Machine Tools and Manufacture, 117, 26-38. https://doi.org/10.1016/j.ijmachtools.2017.02.002
15. Walter, C., & Rabiey, M. (2012). Laser dressing of fine-grained grinding wheels for micro-machining. CIRP Journal of Manufacturing Science and Technology, 5(4), 299-306. https://doi.org/10.1016/j.cirpj.2012.09.005
16. Zhang, X., & Wang, Y. (2020). Sustainability aspects of laser dressing for grinding wheels. Sustainable Materials and Technologies, 25, e00185. https://doi.org/10.1016/j.susmat.2020.e00185
17. Wang, J., Zhang, X., & Yu, T. (2022). Research and Progress on Truing and Sharpening Process of Diamond Abrasive Grinding Tools. Applied Sciences, 12(9), 4683. https://doi.org/10.3390/app12094683
18. Westkämper, E. (1995). Grinding wheel dressing with Nd:YAG lasers: Early developments and applications. Journal of Materials Processing Technology, 52(2-4), 536-546. https://doi.org/10.1016/0924-0136(94)01454-7

TalentDetector
26th September 2025
Gliwice, Poland
FACULTY OF MECHANICAL ENGINEERING
SILESIAN UNIVERSITY OF TECHNOLOGY
INTERNATIONAL STUDENTS SCIENTIFIC CONFERENCE

Active Suspension Control for Enhanced Vehicle Ride Comfort Using Fuzzy-PID Control

Liangpeng Li [a], Chao Ding [a], Fangcheng Liu [a]

[a] Yanshan University, College of Mechanical Engineering
email: liliangpeng2021@gmail.com

Abstract: Drivers and passengers are increasingly demanding higher levels of ride comfort, and the suspension system is a critical component that significantly influences ride comfort. Therefore, improving the performance of the suspension system can enhance the overall ride comfort of a vehicle. The article first applies the Fourier transform to the international standard road surface frequency domain model, combines it with filtered white noise to generate a road surface frequency domain model, and establishes a whole-vehicle four-wheel road surface excitation time domain model based on the spatial correlation between left and right wheels and the time lag between front and rear wheels; Then, a seven-degree-of-freedom vehicle dynamics model for ride comfort analysis is established using Simulink. Through time-domain simulation, the amplitude changes in body acceleration are clarified, and the domain of the fuzzy controller is determined. Finally, based on the input of the fuzzy controller and the determination of fuzzy control rules, a controller is constructed by combining proportional-integral-derivative (PID) control to compare the time-domain curves of body acceleration between active and passive suspension systems. The results show that fuzzy PID control has good control performance in improving vehicle ride comfort, providing important reference value for in-depth research on suspension performance optimization.

Keywords: Road surface excitation, fuzzy control, PID

1. INTRODUCTION

New energy vehicles do not have engines or transmissions, so there is no impact on ride comfort from engine noise and vibration or transmission shift shock. Currently, the biggest factor affecting ride comfort in new energy vehicles is road surface excitation.

Currently, major automobile manufacturers are actively researching and adopting advanced active suspension technologies to improve vehicle ride comfort and handling performance. These technologies can adjust suspension stiffness and damping in real time according to the actual needs of the vehicle during operation, thereby providing the best driving experience. For example, Mercedes-Benz has adopted electronic active body control technology in its high-end models, which not only adapts to road conditions but also uses a front-facing camera to preview the road ahead and adjust the suspension settings in advance to ensure a smooth ride over

uneven surfaces[1]. Audi has equipped its flagship A8 model with a 48V electro-mechanical coupled active suspension system. The key feature of this system is that each wheel is equipped with an electric motor, which is connected to the torsion bar via belts and drive wheels, enabling rapid response to road surface changes and providing excellent ride comfort and vehicle stability[2]; BMW's adaptive air suspension is an active suspension system that uses sensors to detect the vehicle's driving status and adjusts the damping of the shock absorbers via an Electronic Control Unit (ECU) to adapt to different driving conditions[3].

This paper takes a certain pure electric sedan as the research object, establishes a seven-degree-of-freedom dynamic model of the entire vehicle based on Simulink, and generates random excitation signals for C-class road surfaces based on the power spectral density of the road surface. To address the issue of PID parameters not being able to be adjusted in real time, this paper adopts a method combining fuzzy control with PID control. Fuzzy control is used to adjust the PID control parameters in real time.Through simulation analysis, it was found that under the control of active suspension force, the vibration magnitude value of the spring-mounted accelerometer on the entire vehicle was attenuated to a certain extent, thereby improving the ride comfort of the vehicle.

2. SEVEN-DEGREE-OF-FREEDOM WHOLE-VEHICLE DYNAMICS MODELING

In the field of whole-vehicle ride comfort simulation, a seven-degree-of-freedom vehicle model is generally used. This model has the advantages of fast calculation speed and easy integration with active suspension systems[4]. The model equates the whole vehicle to four wheel (spring-mounted) mass blocks and one body (spring-mounted) mass block, which can respectively reflect the vertical movement of the four wheels, the vertical movement of the body, the roll movement, and the pitch movement. Fig. 1 shows the seven-degree-of-freedom model of the whole vehicle.

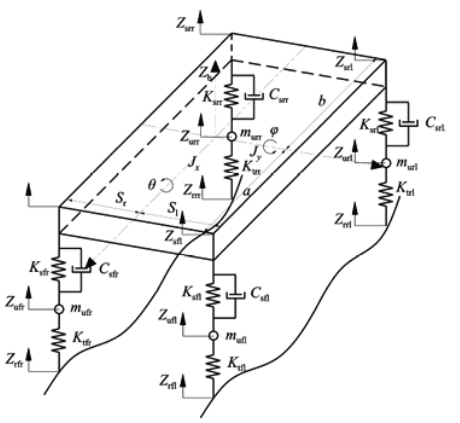

Fig. 1 Seven-degree-of-freedom vehicle model

The dynamic equation includes: four wheel vertical motion equations, body vertical, roll, and pitch motion equations[5]. Body vertical motion equation:

$$m\ddot{z}_b + \sum_{i=1}^{4} c_{sij}(\dot{z}_{sij} - \dot{z}_{uij}) + \sum_{i=1}^{4} k_{sij}(z_{sij} - z_{uij}) = 0$$

Body pitch motion equation:

$$J_y\ddot{\varphi}_b - ac_{\mathrm{sfl}}(\dot{z}_{\mathrm{sfl}} - \dot{z}_{\mathrm{ufl}}) - ac_{\mathrm{sfr}}(\dot{z}_{\mathrm{sfr}} - \dot{z}_{\mathrm{ufr}}) + bc_{\mathrm{srl}}(\dot{z}_{\mathrm{srl}} - \dot{z}_{\mathrm{url}}) + bc_{\mathrm{srr}}(\dot{z}_{\mathrm{srr}} - \dot{z}_{\mathrm{urr}}) -$$
$$ak_{\mathrm{sfl}}(z_{\mathrm{sfl}} - z_{\mathrm{ufl}}) - ak_{\mathrm{sfr}}(z_{\mathrm{sfr}} - z_{\mathrm{ufr}}) + bk_{\mathrm{srl}}(z_{\mathrm{srl}} - z_{\mathrm{url}}) + bk_{\mathrm{srr}}(z_{\mathrm{srr}} - z_{\mathrm{urr}}) = 0$$

Body roll equation:

$$J_x\ddot{\theta}_b - s_{\mathrm{l}}c_{\mathrm{sfl}}(\dot{z}_{\mathrm{sfl}} - \dot{z}_{\mathrm{ufl}}) - s_{\mathrm{l}}c_{\mathrm{sfr}}(\dot{z}_{\mathrm{sfr}} - \dot{z}_{\mathrm{ufr}}) + s_{\mathrm{r}}c_{\mathrm{srl}}(\dot{z}_{\mathrm{srl}} - \dot{z}_{\mathrm{url}}) + s_{\mathrm{r}}c_{\mathrm{srr}}(\dot{z}_{\mathrm{srr}} - \dot{z}_{\mathrm{urr}}) -$$
$$s_{\mathrm{l}}k_{\mathrm{sfl}}(z_{\mathrm{sfl}} - z_{\mathrm{ufl}}) - s_{\mathrm{l}}k_{\mathrm{sfr}}(z_{\mathrm{sfr}} - z_{\mathrm{ufr}}) + s_{\mathrm{r}}k_{\mathrm{srl}}(z_{\mathrm{srl}} - z_{\mathrm{url}}) + s_{\mathrm{r}}k_{\mathrm{srr}}(z_{\mathrm{srr}} - z_{\mathrm{urr}}) = 0$$

Wheel vertical motion equation:

$$m_{\mathrm{u}ij}\ddot{z}_{uij} - c_{sij}(\dot{z}_{sij} - \dot{z}_{\mathrm{u}ij}) - k_{sij}(z_{sij} - z_{\mathrm{u}ij}) + k_{tij}(z_{\mathrm{u}ij} - z_{\mathrm{r}ij}) = 0$$

The relationship between the body and suspension connection points and the vertical movement of the body is as follows:

$$\begin{cases} z_{\mathrm{sfl}} = z_{\mathrm{b}} - a \times \varphi + s_{\mathrm{l}} \times \theta \\ z_{\mathrm{sfr}} = z_{\mathrm{b}} - a \times \varphi - s_{\mathrm{r}} \times \theta \\ z_{\mathrm{srl}} = z_{\mathrm{b}} + b \times \varphi + s_{\mathrm{l}} \times \theta \\ z_{\mathrm{srr}} = z_{\mathrm{b}} + a \times \varphi - s_{\mathrm{r}} \times \theta \end{cases}$$

Fig.2 shows the time-domain characteristic curve of the vehicle's vertical acceleration in the whole-vehicle ride comfort simulation. Analysis reveals that under the excitation of a C-class road surface, the peak vertical acceleration of the vehicle body does not exceed 1 m/s², which provides some reference value for the subsequent setting of fuzzy rules. The whole-vehicle and suspension parameters are shown in Table 1.

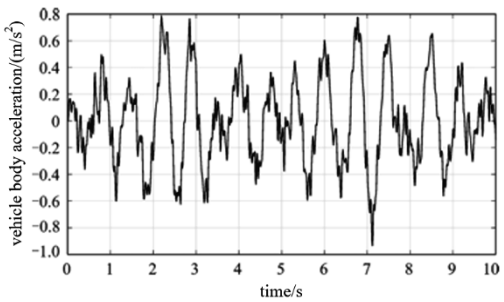

Fig.2 Vertical acceleration of the vehicle body

Table 1 Suspension parameters

Parameters	Value	Parameters	Value
a /m	1.5	k_{sij} /(N/m)	67230
b /m	1.5	C_{sij} /[N/(m/s)]	2355
s_1 /m	0.8	k_{tij} /(N/m)	672300
s_r /m	0.8	m_b /kg	2400
m_{uij} /kg	65		

3. FUZZY PID CONTROLLER DESIGN

The acceleration and velocity at the suspension-to-body connection point are selected as inputs, and the PID incremental parameters ΔK_b, ΔK_i and ΔK_d are selected as outputs. The relationship between the inputs and outputs is described using seven fuzzy subsets: negative

large (NB), negative medium (NM), negative small (NS), zero (ZE), positive small (PS), positive medium (PM), and positive large (PB)[6]. Analyzing the vertical acceleration of the body in Fig.2 reveals that the peak value of vertical acceleration is around 1 m/s². Therefore, the domain of vertical acceleration (e_c) and velocity (e) is selected as [-2, 2], and Fig.3 shows the corresponding membership functions. The domain of the output variables is [-1, 1].

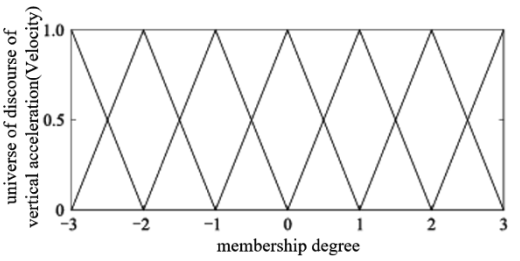

Fig.3 Vertical acceleration belonging function at the connection between the front and rear suspension and the body

The logical relationship between the controller input variables (speed, acceleration) and output variables(ΔK_b , ΔK_i , ΔK_d) is shown in Fig. 4.

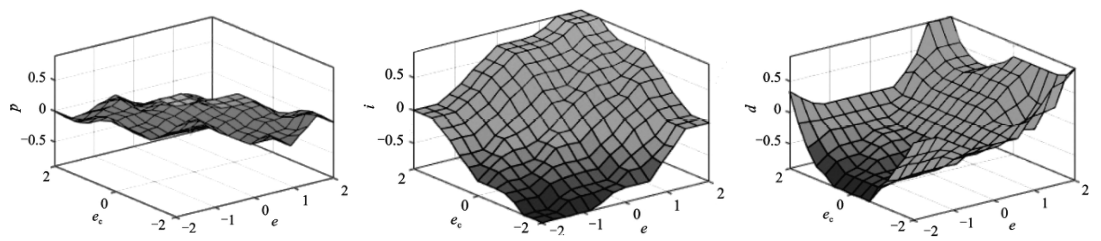

(a) ΔK_b output variable; (b) ΔK_i output variable; (c) ΔK_d output variable.

Fig.4 Fuzzy control rules

PID is an error-based control method that regulates the main force output of the active suspension by calculating the ratio, integral, and derivative of the difference between the ideal speed z_{sfl0} (set to 0) and the actual vertical speed z_{sfl} at the connection point between the front and rear suspensions and the car body. Its mathematical expression is as follows:

$$u(t) = K_p e(t) + K_i \int_0^t e(t)\mathrm{d}t + K_d \frac{\mathrm{d}e(t)}{\mathrm{d}t}$$

In the equation, K_p, K_i, and K_d are the proportional, integral, and derivative gain coefficients, respectively; u(t) is the controller output; and e(t) is the difference between the desired value and the actual output.

Based on experience and the characteristic parameters of the active suspension, the parameters for the proportional, integral, and derivative components were tuned. Through continuous parameter testing, the final proportional, integral, and derivative gain coefficients were determined as $K_p = 1000$, $K_i = 500$, and $K_d = 20$. Finally, a fuzzy PID controller was established based on Simulink.

4. CONTROL SIMULATION ANALYSIS

Verify the active suspension's filtering effect on rough roads and vibration damping effect on uneven roads through C-class road conditions and speed bump conditions.

4.1. Class C road conditions

Analysis of the vertical acceleration of the vehicle body on a C-class road surface (see Fig. 5) reveals that under the control of the suspension's active force, the vertical acceleration of the vehicle body exhibits a certain degree of attenuation. The peak value of the vertical acceleration decreases from 0.787 m/s² to 0.521 m/s², with an attenuation rate of 33.8%. As shown in Fig.6, the suspension uses active force output to promptly "pull" and "support" the body, thereby maintaining body stability, reducing the peak acceleration of the body, and enhancing the riding comfort of occupants.

Currently, the impact of vibration on the human body is generally evaluated using vibration dose values. Vibration dose values (VDV) are used to quantify the cumulative effects of human exposure to a vibrating environment. Considering the impact of the time dimension, it is mainly used to assess the adverse effects that long-term or repeated exposure to vibration may have on health. It is defined as follows:

$$z = (\int_0^T a^4(t)\mathrm{d}t)^{\frac{1}{4}}$$

In the equation, z is the value of VDV; a is acceleration; T is the time period.

Fig.7 shows the vertical vibration dose values of the vehicle body. Analysis reveals that under the control of active suspension forces, the vibration dose values decreased from 0.592 m/s1.75 to 0.379 m/s1.75 within 5 seconds, representing a reduction of 35.8%. Therefore, vehicles equipped with active suspension systems not only enhance ride comfort but also mitigate the adverse effects of vibration on human health to a certain extent.

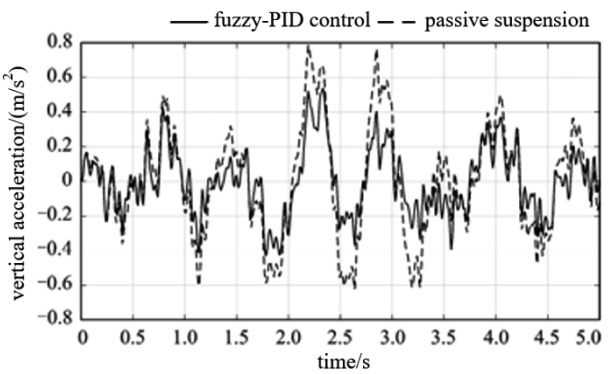

Fig. 5 Vertical acceleration of vehicle body on Class C road surface

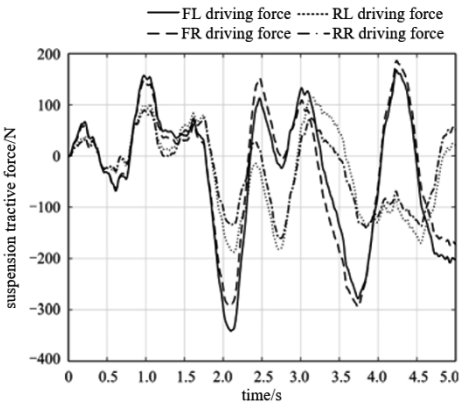

Fig.6 C-class road suspension main power

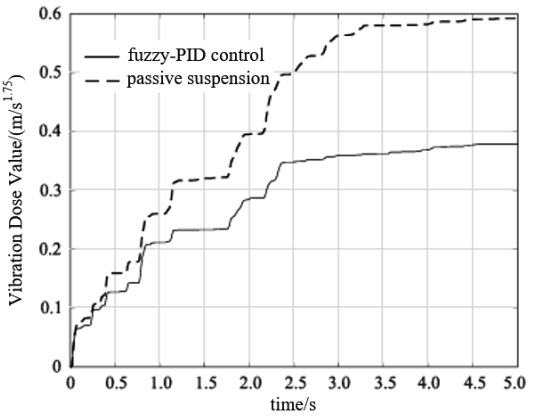

Fig.7 Vertical vibration dose value for Class C road vehicles

4.2. Over speed bump conditions

The vehicle passed over the speed bump at a speed of 72 km/h. The speed bump had a longitudinal length of 0.25 m along the road surface and a height of 0.05 m. Fig.8 shows a comparison of the body acceleration of the passive suspension and active suspension when the vehicle passed over the speed bump.

Analysis of Fig.8 shows that under the influence of active suspension force, both the peak body acceleration during and after passing over a speed bump exhibit significant attenuation. The peak vertical body acceleration decreases from 5.79 m/s² to 3.86 m/s², representing an attenuation of 33.3%.

Fig.9 shows the trend of changes in the main suspension force during the process of crossing speed bumps. Unlike Figure 6, the main suspension force required during the speed bump crossing condition is greater, as the road impact during speed bumps is larger compared to Class C roads, thereby imposing higher performance requirements on the suspension system.

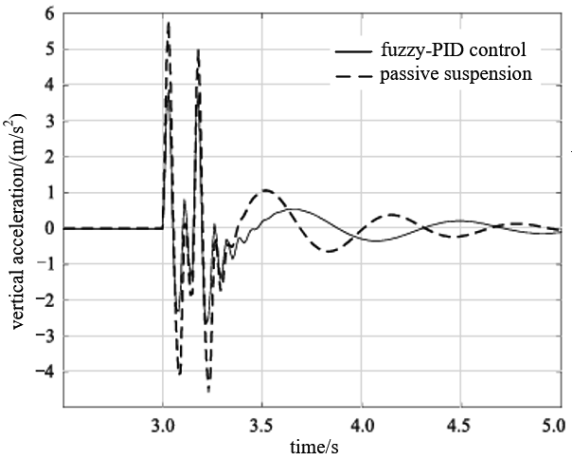

Fig.8 Vertical acceleration of vehicle body when passing over speed bumps

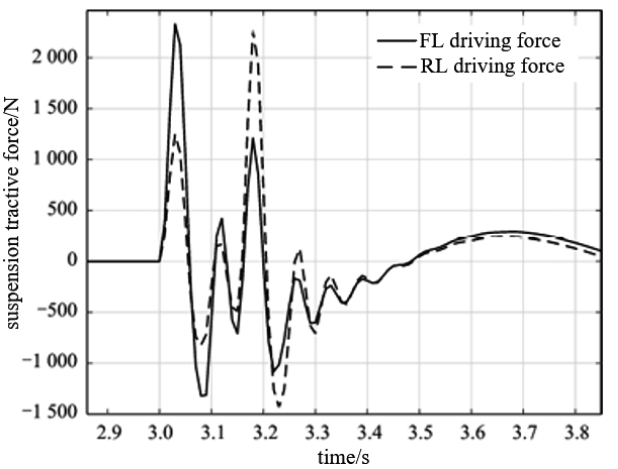

Fig.9 Suspension main power when passing over speed bumps

Analysis of the vertical vibration magnitude values of the vehicle body during the process of crossing speed bumps (see Fig.10) revealed that under the control of the suspension active force, the vertical vibration magnitude values of the vehicle body decreased to a certain extent within 2 seconds after contacting the speed bump. Within 2 seconds, the vibration magnitude values decreased from 2.64 m/s1.75 to 1.67 m/s1.75, with a reduction of 36.7%.

5. CONCLUSION

This paper addresses the issue of vehicle ride comfort by first establishing a seven-degree-of-freedom ride comfort simulation model for the entire vehicle. Based on the simulation analysis results, the domain and rules for fuzzy control were determined, and these were combined with PID to establish a controller for the suspension. Simulation analysis conducted under C-class road conditions and over speed bumps revealed that both the peak body acceleration and VDV decreased to a certain extent. Through comparative simulation analysis, it was found that active suspension control plays a significant role in improving vehicle ride comfort.

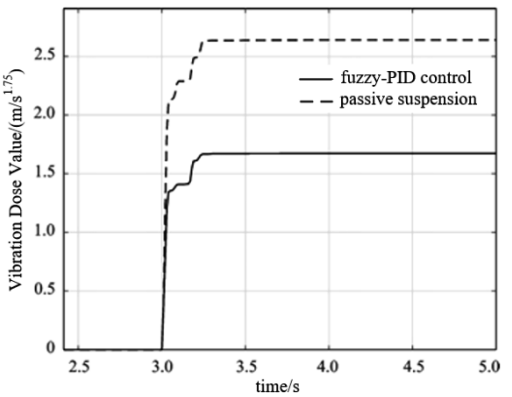

Fig. 10 Vertical vibration magnitude of the vehicle body when passing over speed bumps

REFERENCES

1. Gawad M A A. Mechatronic suspension systems: a survey and directions for future work[J]. American Journal of Engineering Research (AJER), e-ISSN, 2021: 2320-0847.
2. Yu M, Evangelou S A, Dini D. Advances in active suspension systems for road vehicles[J]. Engineering, 2024, 33: 160-177.
3. Ma C, Lu Y, Zhen R, et al. On-the-Market Air Suspension Systems for Passenger Cars[J]. SAE International Journal of Vehicle Dynamics, Stability, and NVH, 2025, 9(10-09-02-0016).
4. Zhu G, Wang F. Research on the enhancement method of vibration damping effect of vehicle fully active suspension system based on genetic algorithm and fuzzy control[J]. J. COMBIN. MATH. COMBIN. COMPUT, 2025, 127: 2527-2547.
5. Rill G. Vehicle dynamics[J]. 2004.
6. Hajighorbani S, Radzi M A M, Ab Kadir M Z A, et al. Evaluation of fuzzy logic subsets effects on maximum power point tracking for photovoltaic system[J]. International Journal of Photoenergy, 2014, 2014(1): 719126.

TalentDetector
26th September 2025
Gliwice, Poland
FACULTY OF MECHANICAL ENGINEERING
SILESIAN UNIVERSITY OF TECHNOLOGY
INTERNATIONAL STUDENTS SCIENTIFIC CONFERENCE

Review on Fault Diagnosis Methods for Rolling Bearing

Menglong Shao [a,b], Chengepng Yu [b], Jiaxu Fu [b]

[a] Hebei Provincial Key Laboratory of Heavy Machinery Fluid Power Transmission and Control, Yanshan University, Qinhuangdao 066004, China
[b] School of Mechanical Engineering, Yanshan University, Qinhuangdao 066004, China

Abstract: Rolling bearings are one of the most important core components in rotating machinery, and their performance directly affects the reliability and stability of the mechanical system. This paper reviews the research progress of rolling bearing fault diagnosis methods, systematically analyzes their fault mechanisms and common failure modes, and focuses on fault diagnosis methods based on signal processing. It also analyzes and prospects the future development trends of rolling bearing fault diagnosis.

Keywords:Rolling bearing; Troubleshooting; Failure mechanism; Signal processing

1. INTRODUCTION

In recent years, China has vigorously promoted the rapid development of the manufacturing industry. As the core foundation of manufacturing, mechanical equipment plays an important role in high-precision fields such as aerospace, military, integrated circuits, as well as daily transportation industries such as automobiles, railways, and rail transit. With the continuous advancement of technology and the increasing demand for production, the structure of mechanical equipment is becoming increasingly complex to adapt to diverse and demanding working conditions. In this context, key components such as bearings are affected by both internal factors and external factors during long-term operation, and their performance and health status will gradually deteriorate until failure occurs. Once key components fail, it can lead to a decrease in product quality or equipment shutdown, and in severe cases, it may cause serious safety accidents such as casualties.

As a crucial basic component in mechanical equipment, rolling bearings have been widely used in modern manufacturing and industrial production due to their characteristics of low friction, compact size, high speed, and long service life. However, due to complex working conditions and long-term service, rolling bearings are prone to fatigue damage and structural failure. Especially in environments with strong noise and multi-source interference, early weak fault signals are often masked, posing significant challenges to state recognition and fault diagnosis. How to accurately determine the degree of damage and failure mode of rolling bearings has always been a research focus of equipment fault diagnosis technology. Although significant achievements have been made in vibration characteristic analysis, acoustic emission

detection, temperature monitoring, signal processing, and intelligent diagnostic methods, there are still significant difficulties in achieving early and accurate diagnosis in complex noise backgrounds. Therefore, delving into the common fault mechanisms and failure processes of rolling bearings, and developing efficient and reliable real-time monitoring and intelligent diagnostic methods based on this, can not only achieve early identification and warning of potential faults, but also significantly extend the service life of bearings and complete equipment, improve the safety and stability of operating systems, which is of great significance in both theoretical research and engineering applications.

2. ROLLING BEARINGS AND THEIR FAULT MECHANISM ANALYSIS

2.1 Rolling bearing composition and types

Common rolling bearings are generally composed of three parts: inner ring, outer ring and rolling element, as shown in *Figure 1*.

Fig 1. Fault structure of rolling bearing [1]

The inner and outer rings usually have a supporting role, and the shape, size and number of the rolling elements themselves directly play a decisive role in determining the bearing capacity, and the cage is used to prevent the rolling elements from falling off.

The types of rolling bearings can be divided into deep groove ball bearings, needle roller bearings, angular contact bearings, spherical roller bearings, cylindrical roller bearings, tapered roller bearings, etc. according to the structure, as shown in *Table 1*.

Table 1. Types and characteristics of rolling bearings

Types of rolling bearings	Key features
Deep groove ball bearings	Bearings with a simple structure, user-friendly, and versatile applications, primarily designed to handle radial loads while also capable of supporting limited axial loads.
Needle roller bearings	Compact radial structure with the same inner diameter and load capacity as other bearings, but with the smallest outer diameter, ideal for support structures with limited radial installation space.
Angular contact bearings	The ultimate speed is high, and it can bear both warptic and axial loads, as well as pure

	axial loads.
Spherical roller bearings	It mainly bears radial loads, and can bear a small amount of axial loads while bearing radial loads, and is usually not used to bear pure axial loads.
Cylindrical roller bearings	Easy to install and remove, ideal for interference fits between inner/outer rings, shaft, and housing, typically bearing only radial loads.
Tapered roller bearings	It is suitable for bearing radial and axial combined loads dominated by radial loads.

2.2 Rolling bearing failure mechanism

Rolling bearings operate for a long time under conditions of continuous change in speed and load, and are one of the most vulnerable components in mechanical equipment. Throughout its life cycle, problems in different parts of the bearing can produce different types of failures, such as spalling, wear, or cracking, often caused by factors such as corrosion, fatigue, or plastic deformation. Therefore, when studying the failure mechanism of rolling bearings, it is necessary to focus on analyzing the causes and characteristics of the fault,as shown in *Table 2*.

Table 2. Analysis of the failure mechanism of rolling bearings

Fault type	Causes
Fatigue peeling of the inner ring, outer ring, rolling element	Contact fatigue caused by long-term operation; insufficient lubrication or oil pollution; Improper installation leads to stress concentration.
Wear of inner ring, outer ring, rolling element	Lubricating oil mixed with hard particles; Lubricating film breakage, direct metal contact; Installation skew or overload operation.
Cracks and fractures in the inner ring, outer ring, and rolling element	Overload impact or excessive force during assembly; material defects; Poor heat treatment.
The cage is damaged	Insufficient lubrication or foreign object entry; installation eccentricity, vibration shock.

3. ROLLING BEARING FAULT DIAGNOSIS TECHNOLOGY

With the development of the times and the continuous development and progress of science and technology, the fault diagnosis technology used to realize rolling bearings has gradually become mature. At present, the vibration signal of rolling bearings is generally used to diagnose faults.

Traditional signal processing methods can analyze and decompose signals in the time, frequency, and time-frequency domains. Fourier Transform[2], Hilbert Transform[3], Wavelet Transform[4], Empirical Mode Decomposition(EMD)[5], Hilbert-Huang Transform[6] and

Variational Mode Decomposition(VMD)[7] method to analyze and classify the collected vibration data. Table 1 summarizes and compares the advantages and disadvantages of related methods. By using them to analyze and decompose the collected vibration signals, the characteristics of the vibration signals are easier to identify, enabling fault detection.

Table 3. Comparison of fault diagnosis methods of rolling bearings based on signal processing

Methods	Literature	Technical characteristics	Advantages	Disadvantages
Fourier Transform	Xie et al.[8],Yu et al.[9]	Time-domain vibration is transformed to frequency domain to analyze bearing characteristic frequencies and harmonics.	Bearing fault frequencies can be identified; suitable for periodic signals; spectrum is intuitive.	Insensitive to non-stationary signals; cannot show time variation; early faults may be hidden by noise.
Hilbert Transform	Li et al.[10],Liang et al.[11]	Envelope is obtained by Hilbert transform, then frequency analysis is applied.	Sensitive to local defects of rolling elements; It can amplify the impact characteristics	Less effective for nonlinear or modal aliasing signals; requires strict preprocessing.
Wavelet Transform	Yang et al.[12],Chen et al.[13]	The signal is decomposed at multiple resolutions and the fault features are extracted on the time-frequency plane	Suitable for non-stationary signals; Transient shocks can be extracted; Noise and fault components can be separated	Sensitive to wavelet choice and decomposition levels; computationally heavy; highly parameter-dependent.
EMD	Lin et al.[14],Cai et al.[15]	Signal is adaptively decomposed into IMFs, then each IMF's features are analyzed.	Effective for nonlinear and nonstationary signals	Modal aliasing; noise-sensitive; obvious boundary effects.
Hilbert-Huang Transform	Wang et al.[16],Yuan et al.[17]	EMD decomposes the signal into IMFs, then Hilbert transform gives	Suitable for non-stationary, nonlinear signals; sensitive to	Affected by EMD modal aliasing; computational complexity; The result

		instantaneous frequency and amplitude.	early faults.	depends on the decomposition quality
VMD	Jiang et al.[18],Chen et al.[19]	Signal is decomposed into modal components with distinct frequency bands using an optimization algorithm.	strong anti-modal aliasing ability; suitable for nonlinear and non-stationary signals;	Modal number and penalty factors must be preset; sensitive to initial parameters.

4. SUMMARY AND PROSPECT

4.1 Summary

The current fault diagnosis methods mainly include traditional signal analysis and deep learning. The former relies on rich signal processing knowledge to extract features through time-domain, frequency-domain, or time-frequency domain decomposition, but there are methodological limitations, such as the Fourier transform is difficult to distinguish between similar non-stationary signals, and the short-time Fourier transform is limited by the window function and can only achieve single-resolution analysis. These defects restrict its application under complex working conditions. In contrast, deep learning can use deep networks to extract features independently, which has become an important development direction for fault diagnosis. However, deep learning relies on large amounts of labeled data and is limited in the case of insufficient or unbalanced data. For example, autoencoder-based methods are significantly less accurate in the face of novel failures.

In response to this challenge, researchers have proposed a variety of improvement options. Data augmentation and generative adversarial networks can alleviate sample imbalances, but the difference between generated data and real conditions will affect model accuracy. Transfer learning provides new ideas for solving data scarcity, and can transfer knowledge in related fields to troubleshooting tasks. In addition, improving the fault data generation method and improving the robustness and generalization ability of the model are also the key directions of future research. In general, how to achieve high-precision and generalizable fault diagnosis under data imbalance and complex working conditions is still a core problem that needs to be broken through.

4.2 Prospect

Although significant advances have been made in bearing fault diagnosis technology, there are still some limitations. Future research can be carried out from the following aspects:

4.2.1 Improve model interpretability

Although the current deep learning methods can achieve high diagnostic accuracy, their "black box" characteristics make the model decision-making process lack transparency, which limits its popularization in industrial scenarios. In the future, domain knowledge, rule-based reasoning methods, or visualization techniques can be combined to enhance model interpretability, thereby improving operators' understanding and trust in diagnostic results.

4.2.2 Multi-source data fusion

A single signal often makes it difficult to fully describe the operating status of the equipment. Future research can explore fusion methods of multi-source data such as vibration, acoustics, temperature, and current to give full play to the complementary advantages of different signals.Through the fusion of feature level or decision level, the accuracy, robustness, and generalization ability of diagnosis can be improved.

4.2.3 Robustness and migration ability under complex working conditions

Industrial environments are often accompanied by noise interference and changes in working conditions, resulting in poor performance of models when applied across operating conditions. Transfer learning has shown some potential, but there is still a dependence on large-scale samples and the risk of "negative migration". In the future, we should focus on developing efficient migration strategies under small sample conditions to improve the adaptability of the model in complex scenarios.

4.2.4 Distributed and edge-cloud co-computing

With the growth of industrial data, it is difficult for stand-alone computing to meet the needs of real-time diagnosis. Distributed computing and edge-cloud collaboration architecture can realize parallel data processing and rapid modeling: edge nodes are responsible for real-time detection, and cloud platforms perform in-depth analysis and model optimization, which can significantly improve the timeliness and scalability of the system.

BIBLIOGRAPHY

[1]CHEN D N, HU D B, WANG H W, et al. Conditional Feature Generative Adversarial Network for Fault Diagnosis of Axial Piston Pump[J/OL]. IEEE Sensors Journal, 2025, 25(11): 20907-20919.
[2]WANG F, SUN J, YAN D, et al. A Feature Extraction Method for Fault Classification of Rolling Bearing based on PCA[J/OL]. Journal of Physics: Conference Series, 2015, 628: 012079.
[3]ZHENG J, YUAN Y, ZOU L, et al. Study on a Novel Fault Diagnosis Method Based on VMD and BLM[J/OL]. Symmetry, 2019, 11(6): 747.
[4]MALLAT S G. A theory for multiresolution signal decomposition: the wavelet representation[J/OL]. IEEE Transactions on Pattern Analysis and Machine Intelligence, 1989, 11(7): 674-693.
[5]BOUDRAA A O, CEXUS J C. EMD-Based Signal Filtering[J/OL]. IEEE Transactions on Instrumentation and Measurement, 2007, 56(6): 2196-2202.
[6]PENG Z K, TSE P W, CHU F L. A comparison study of improved Hilbert–Huang transform and wavelet transform: Application to fault diagnosis for rolling bearing[J/OL]. Mechanical Systems and Signal Processing, 2005, 19(5): 974-988.
[7]LI Z, CHEN J, ZI Y, et al. Independence-oriented VMD to identify fault feature for wheel set bearing fault diagnosis of high speed locomotive[J/OL]. Mechanical Systems and Signal Processing, 2017, 85: 512-529.
[8]XIE Y, ZHANG T. Feature extraction based on DWT and CNN for rotating machinery fault diagnosis[C/OL]//2017 29th Chinese Control And Decision Conference (CCDC). Chongqing, China: IEEE, 2017: 3861-3866[2025-08-19].

[9]YU J, LV J. Weak Fault Feature Extraction of Rolling Bearings Using Local Mean Decomposition-Based Multilayer Hybrid Denoising[J/OL]. IEEE Transactions on Instrumentation and Measurement, 2017, 66(12): 3148-3159.
[10] LIU H, LI D, YUAN Y, et al. Fault Diagnosis for a Bearing Rolling Element Using Improved VMD and HT[J/OL]. Applied Sciences, 2019, 9(7): 1439.
[11] LIANG B, FENG W. Bearing Fault Diagnosis Based on ICEEMDAN Deep Learning Network[J/OL]. Processes, 2023, 11(8): 2440.
[12] YANG P, ZHANG B, ZHAO J. Efficient fault diagnosis in rolling bearings lightweight hybrid model[J/OL]. Scientific Reports, 2025, 15(1): 11514.
[13] CHEN Y, ZHANG T, LUO Z, et al. A Novel Rolling Bearing Fault Diagnosis and Severity Analysis Method[J/OL]. Applied Sciences, 2019, 9(11): 2356.
[14] LIN L, HONGBING J. Signal feature extraction based on an improved EMD method[J/OL]. Measurement, 2009, 42(5): 796-803.
[15] CAI X, LI D, ZHANG J, et al. MA-EMD: Aligned empirical decomposition for multivariate time-series forecasting[J/OL]. Expert Systems with Applications, 2025, 267: 126080.
[16] WANG Y S, MA Q H, ZHU Q, et al. An intelligent approach for engine fault diagnosis based on Hilbert–Huang transform and support vector machine[J/OL]. Applied Acoustics, 2014, 75: 1-9.
[17] YUAN Z, ZHANG L, DUAN L, et al. Intelligent Fault Diagnosis of Rolling Element Bearings Based on HHT and CNN[C/OL]//2018 Prognostics and System Health Management Conference (PHM-Chongqing). Chongqing: IEEE, 2018: 292-296.
[18] JIANG X, SHEN C, SHI J, et al. Initial center frequency-guided VMD for fault diagnosis of rotating machines[J/OL]. Journal of Sound and Vibration, 2018, 435: 36-55.
[19] JIN Z, CHEN D, HE D, et al. Bearing Fault Diagnosis Based on VMD and Improved CNN[J/OL]. Journal of Failure Analysis and Prevention, 2023, 23(1): 165-175.

TalentDetector
26th September 2025
Gliwice, Poland
FACULTY OF MECHANICAL ENGINEERING
SILESIAN UNIVERSITY OF TECHNOLOGY
INTERNATIONAL STUDENTS SCIENTIFIC CONFERENCE

Research on Mechanical Properties of Gradient Metal Foam

Chenfei Sun, Kailun Jia

Yanshan University, School of Mechanical Engineering ,National Engineering Research Center for Equipment and Technology of Cold Strip Rolling
email: 1518623247@qq.com

Abstract: This paper establishes a mechanical model for gradient foam metals, through secondary development of the COMSOL finite element software, combined with MATLAB for numerical calculations, to design various gradient foam metal structures for three-dimensional geometric modeling; then mechanical meshing is performed using HYPELMESH software, and finally finite element analysis is conducted using ABAQUS software. The study analyzes the stress-strain curves under the same loading conditions between different types of gradients and different porosities. Finally, the impact of gradients on load-bearing capacity is analyzed, leading to conclusions. Additionally, numerical simulation methods are used to investigate the mechanical performance differences of various gradient foam metals.
Keywords: gradient metal foam, numerical simulation, finite element analysis;

1. INTRODUCTION

1.1. Source of the topic

In nature, there are many natural foam[1] solid structures, such as trees and bones. In fact, foam materials are ubiquitous in our surroundings and appear extensively in daily life, serving various roles including structure[2], buffering[3], shock absorption[4], thermal insulation[5], soundproofing[6], and filtration[7]. High porosity solid materials are highly rigid and have low bulk density, which is why natural foam solids are often used as structural components.

Metal foam is a rapidly developing new type of engineering material that combines both functional and structural metallic properties. This lightweight material not only retains the weldability, conductivity, and ductility of metals, but also possesses characteristics such as low density, high specific surface area[8], energy absorption and shock damping, soundproofing, electromagnetic shielding, gas permeability, water permeability, and low thermal conductivity.

Gradient metal foams[9] are materials that arrange pore sizes or porosity in a specific pattern in certain dimensions, forming a regularly varying foam metal material. By designing different gradients, more precise control over the material's properties can be achieved, such as reducing weight while maintaining a certain strength and enhancing thermal insulation and soundproofing properties.

The mechanical properties of foam materials are strongly dependent on their porosity; in addition, pore morphology and pore size and their distribution also play roles. Among all pore

factors, porosity is the most important indicator affecting the mechanical properties of porous products apart from the material itself. Metal foams possess unique advantages in structural applications due to their high specific strength and ease of installation, which allows for their effective application in many fields.

Although foam metals play an important role in many fields, traditional uniform or irregular foam metals have certain limitations in their performance.

Therefore, to further enhance the performance and functionality of porous structures, the design of gradient varied diverse structures has become a research focus. This design method introduces gradient variations in structural features within materials, such as varying pore sizes, pore shapes, pore distributions, or material distributions, to achieve optimized performance with properties that change gradually in the porous structure.

1.1 Main research content

This article establishes a mechanical model for gradient foam metals and studies the mechanical compression properties of various gradient foam metals. The specific research content is as follows:

•Taking the radial gradient foam structure as the research object, different gradient foam metal structures are designed for three-dimensional geometric modeling using the secondary development of COMSOL finite element software, to compare the relationship between porosity and different gradients.

•Mechanical meshing is then conducted using HYPELMESH software, followed by finite element analysis using ABAQUS software. The stress-strain curves are analyzed under the same load conditions for different gradients and varying porosities.

• Finally, the effect of gradient on load-bearing capacity is analyzed, leading to a conclusion.

2. DESIGN AND THEORETICAL FOUNDATIONS OF GRADIENT FOAM METAL STRUCTURES

2.1 Mathematical Definition, Characteristic Analysis, and Structural Classification of Gradient Functions

• Mathematical definition of the gradient function

This section discusses a cubic gradient foam metal sample with a side length of L. A spherical coordinate system is established with its geometric center as the origin O. The radial distance l is defined as the distance from the origin to the surface of the hollow cube where the pore center is located, with a value range of l∈[0,L], where L=L/2.

The variation of porosity P along the radial direction l is described using the following power law function:

$$P(l) = P_{min} + (P_{max} - P_{min})(\frac{l}{R})^n$$

In the formula:

P_{min}——minimum porosity.

P_{max}——maximum porosity.

n ———gradient index.

l/R ——normalized radial coordinate.

• Analysis of Function Characteristics

A deep understanding of the characteristics of the function P(l) is crucial for predicting material properties. The following analyzes its key mathematical characteristics and their physical implications:

The first derivative of the gradient function $P'(l)$ reflects the monotonicity of porosity as shown in Figure 1.

$$P'(l) = n(P_{max} - P_{min})\frac{1}{R}(\frac{l}{R})^{n-1}$$

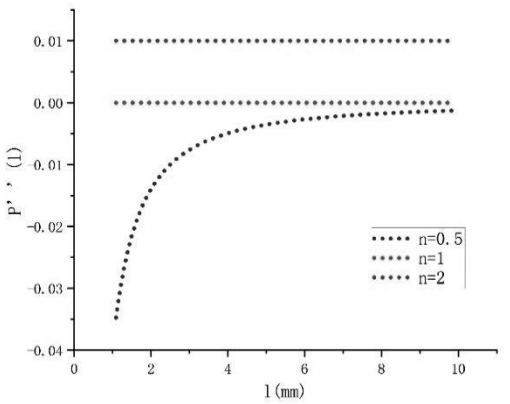

Figure 1. First derivative $P'(l)$

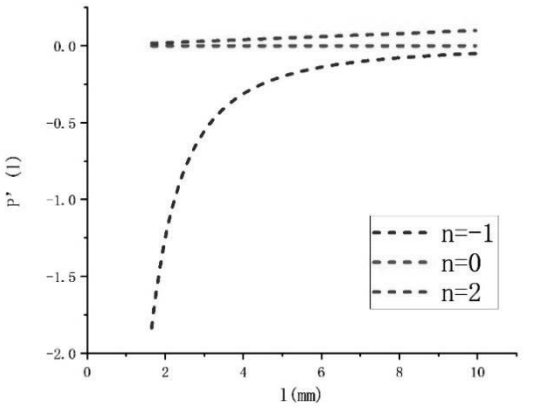

Figure 2. Second derivative $P''(l)$

This article mainly studies the gradient structure when n > 0, which refers to the gradual increase of porosity from the inside out.

The second derivative of the gradient function P"(l) reflects the trend of acceleration or deceleration in porosity changes, as shown in Figure 2.

$$P''(l) = n(n-1)(P_{max} - P_{min})\frac{1}{R^2}(\frac{l}{R})^{n-2}$$

n>1: P″(l)>0. This means that the rate of increase in porosity accelerates as l increases.

n=1: P″(l)=0, the function is linear. Porosity changes uniformly with l.

0<n<1: P″(l)<0. This means that the rate of increase in porosity slows down as l increases.

2.2 Characteristics of 316L Stainless Steel Materials

The chemical composition and physical properties of 316L stainless steel are shown in Table 1 below:

Table 1. Chemical Composition and Physical Properties of 316L Stainless Steel

Characteristic	Parameters
Chemical composition	Cl (16-18%),Ni (10-14%),Mo (2-3%), C (≤0.03%),Fe (surplus)
Crystal structure	Face-centred cubic (FCC austenite, non-magnetic)
Density	$\rho = 7.9g/cm^3$
Elastic modulus	$E = 193GPa$
Poisson's ratio	$\upsilon = 0.3$
Coefficient of thermal expansion	$16.0 \times 10^{-6}K^{-1}(20 - 100℃)$

In summary, 316L stainless steel, with its unique combination of chemical composition and physical properties, becomes an ideal choice for gradient foam metal matrix materials. Its triple advantages of corrosion resistance, mechanical properties, and compatibility with additive manufacturing provide a reliable material foundation for achieving gradient design in structural load-bearing.

3. NUMERICAL SIMULATION METHOD OF MECHANICAL PROPERTIEC OF GRADIENT FOAM METAL

3.1 COMSOL Modelling Process

- Definition of the gradient function

The gradient function adopts a radial power law distribution as shown in the following formula:

$$P(l) = P_{min} + (P_{max} - P_{min})(\frac{l}{R})^n$$

Among them, l is the radial coordinate, R=10mm is the half-length of the cube, $P_{min} = 50\%$, $P_{max} = 80\%$, and the gradient index n controls the steepness and shape of the porosity changes with radial distance. This study selects five typical n values corresponding to different gradient types as shown in Table 2 and Figure 3.

Table 2. Five Types of Gradient Structure Parameters

Model number	Gradient index$n$	Gradient type	Description
1	0.5	concave gradient	The central porosity is rapidly increasing.
2	1.0	linear gradient	Uniform variation of porosity
3	1.5	Weak convex gradient	The surface porosity is gradually decreasing.
4	2.0.	Strong convex gradient	The surface porosity has dramatically decreased.
5	2.5	Super convex gradient	A dense barrier forms in the outermost layer

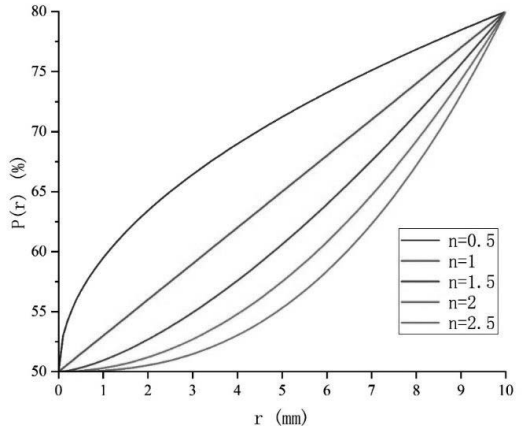

Figure 3. Shows the curves of porosity P(l) corresponding to different gradient indices n varying with the radial coordinate l.

•Calculate the radius of the spherical pores in each unit cell

It is known that l=1, 3, 5, 7, 9mm, $P(l) = P_{min} + (P_{max} - P_{min})(\frac{l}{R})^n$, n=0.5, 1.0, 1.5, 2.0, 2.5. From the above formula, the P(r) corresponding to different n for the hollow cube can be calculated. Additionally, since the porosity of each layer is the same as that of the single unit cell corresponding to each layer, it is sufficient to calculate the porosity of the unit cell corresponding to each layer of the hollow cube.

The classification of the unit cell is as follows:

If the holes are within a 2×2×2 cube, then

$$P(r_{inside}) = \frac{\frac{4}{3}\pi r^3}{8} = \frac{\pi r^3}{6}$$

If the hole is just tangent to the face of the cube, then

$$P(r_{cut}) = \frac{\pi}{6} = 52.3599\%$$

If the hole exceeds the cube$1 < r < \sqrt{3}$

Volume of the sphere:

$$V_{lack} = \frac{\pi}{3}(2r+1)(r-1)^2$$

Total ball volume

$$V_{total\ lack} = 2\pi(2r+1)(r-1)^2$$

$$P(r_{super}) = \frac{\frac{4}{3}\pi r^3 - V_{total\ lack}}{8} = \frac{\pi r^3}{6} - \frac{1}{4}\pi(2r+1)(r-1)^2$$

Then calculate the porosity P(l) corresponding to each n for different l using MATLAB, and compare P(l) with $P(r_{cut}) = \frac{\pi}{6} = 52.3599\%$ to determine the equation for the porosity of the crystal cell corresponding to P(l), and again use MATLAB to calculate the pore radius.

Ultimately, we will obtain all the pore radii corresponding to each n, and then we can officially begin modelling.

•Geometric modeling and pore distribution generation

First, double-click to start COMSOL6.2, enter the page, select the model wizard, select the three-dimensional space dimension, and select the solid mechanics in the structural mechanics module for physics.

Spherical hole generation and Boolean operations:This is a critical step in generating a porous structure based on the idea of generating spheroids within a matrix cube and then subtracting these spheres from the matrix to form holes, the size of which is determined by the local porosity P(l) and n together.

Generate spheres and matrix cubes:Establish balls by the size and position of the holes, and quickly build multiple balls by arranging them. After that, define a complete cube in COMSOL geometry as the initial matrix material. Manually create 20mm×20mm×20mm cubic objects, click on the geometry in the top column, find the cuboid, set its size and position, and finally click Build Selected Object.

Boolean difference set operation generates pores:Under the Geometry node, right-click and select Boolean Operations and Segmentation → Difference Set; Retain object: Select "cube1" (matrix cube); Subtract objects: select "spheles" (all spheres); Advanced options: check "Keep input objects" (for easy debugging), simplify the result selection "Automatic"; Click "Build Selected Objects" to generate a gradient foam structure named "n=0.5, 1.0, 1.5, 2.0, 2.5".

Front view 4 of the final model is shown below

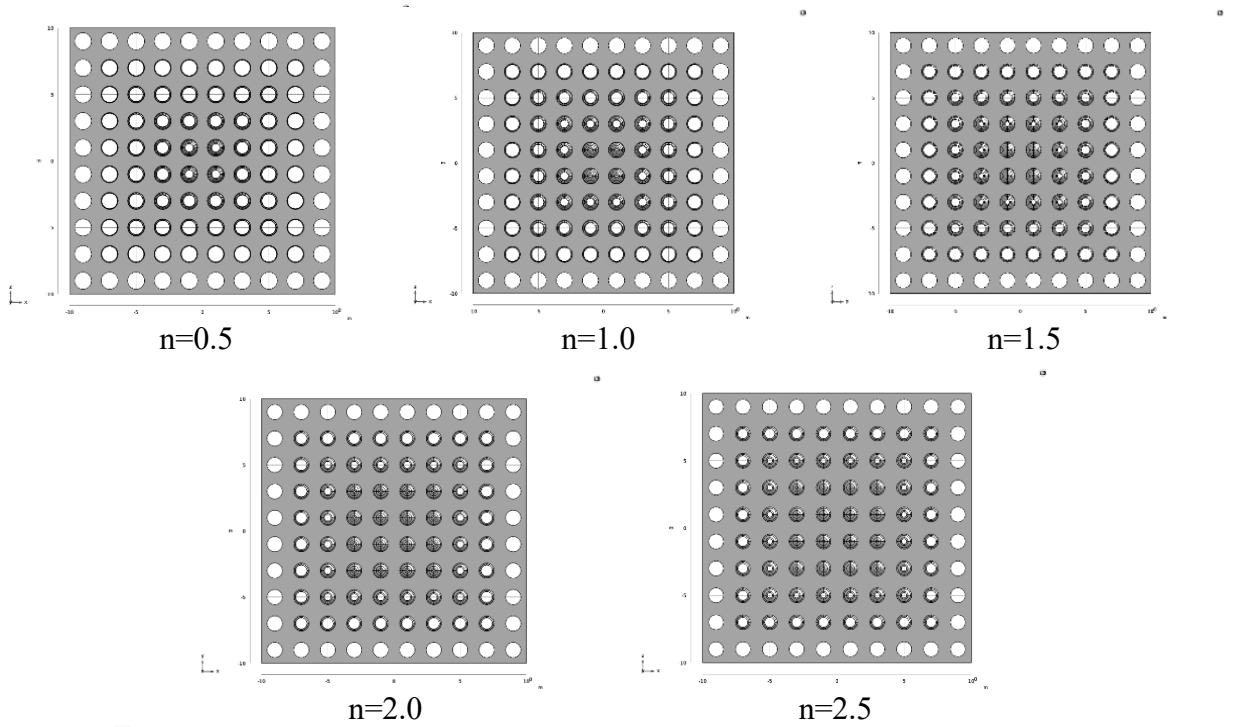

Figure 4. Front view

cModel export and preservation

Once the geometry modeling is complete, export the model to the ".step" format (right-click "Geometry"→ "Export"→ "STEP File") for subsequent meshing in HypelMesh;

Save the COMSOL model file (".mph") to ensure that the parameters and geometry settings are traceable and facilitate quick model updates when subsequent adjustments to the gradient index n or porosity range.

3.2 HypelMesh Construction Mesh

Meshing processMeshing process

In the finite element analysis of gradient foam metals, meshing is a critical step to ensure calculation accuracy and efficiency.

Geometry pretreatment

First, the saved . Step format file, import it into the HypelMesh software, and save the model as a .hm format file to prevent the software from crashing in the middle.

After a batch processing of the model, because the structure of the gradient foam structure is relatively complex, it is not suitable for manual meshing, so I use a BetchMeshel module that comes with HypelMesh software to automatically divide the 2D mesh on the outer surface of the foam structure model just now.

Mesh generation and quality verification

After the batch is run, a .hm file will be generated and then opened in HypelMesh. Press F10 to find meshes less than 0.2 (lengh<0.2) and larger than 0.4 (lengh>0.4), and delete them, as they will cause an error when meshing in 3D.

Then press Shift+F3, click on the model, and then click find edge, you will find that there are no free edges, if there is, then the mesh is not closed, and the 3D mesh cannot be generated.

Point 3D, then tap tetrahedral mesh division tetlamesh, point model, point division mesh.

After dividing, the 2D surface mesh is deleted, leaving only the 3D mesh.The grid is drawn as shown in Figure 5.

Finally, save the model in .hm file format.

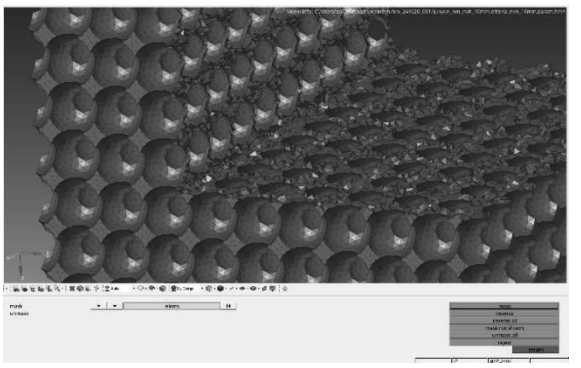

Figure 5. Mesh drawn by HYPERMESH

3.3 Finite element analysis of quasi-static compressive mechanical properties

Fully encastre at the bottom, simulating rigid platform support. The top transfers the load to the reference point through kinematic coupling to avoid stress concentration. The loading mechanism adopts displacement control and compresses at a constant rate to simulate quasi-static conditions. The aim is to accurately capture the nonlinear response of gradient structures in progressive deformation (three stages of elasticity, yield, and densification).

Through boundary conditions and load settings, the quasi-static compression simulation of gradient foam metal can accurately reflect the actual mechanical behavior, which provides a reliable calculation basis for subsequent stress-strain analysis and gradient performance comparison.

3.4 Analysis of Abaqus CAE numerical simulation results

As shown in Fig. 6, the stress-strain curve obtained after numerical simulation of five sets of models and the strain curve of energy absorption efficiency shown in Fig. 7.

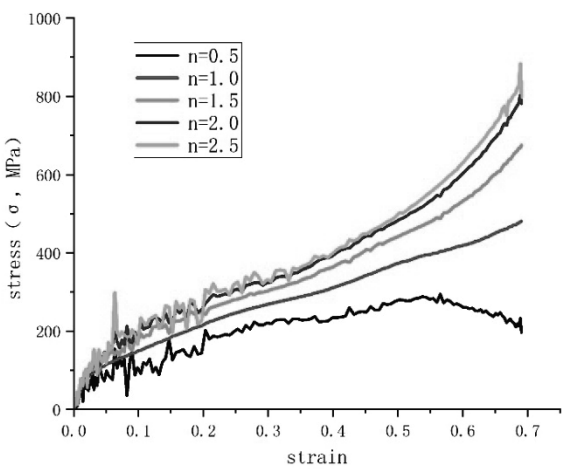

Figure 6. Stress-Strain Curve

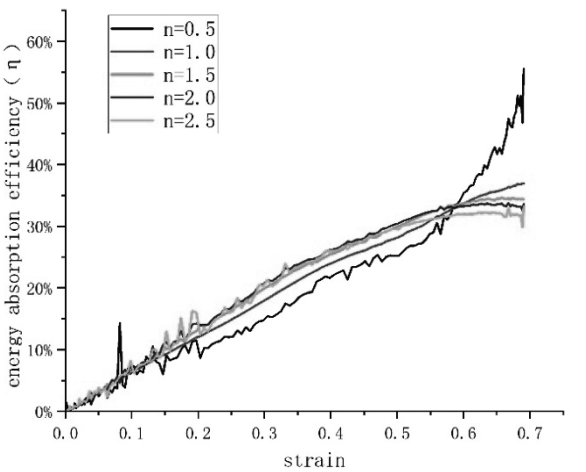

Figure 7. Energy Absorption Efficiency Curve

•The stress-strain curves in Figure 6 show the following:

The larger the gradient index n, the greater the stress it can withstand, indicating higher material strength.

When n = 0.5, the curve exhibits significant jagged fluctuations, indicating early localized failure and unstable load-bearing capacity.

When n = 1.0, the curve increases smoothly and monotonically, indicating uniform plastic deformation and no sudden failure.

When n = 1.5, 2.0, and 2.5, the curve increases overall, but when n = 2.5, there is significant early fluctuation.

•The energy absorption efficiency curve in Figure 7 shows that:

When n = 0.5, the curve rises sharply and oscillates.

When n = 1.0, the curve rises smoothly and monotonically, indicating reliable and progressive energy absorption.

When n = 1.5, 2.0, and 2.5, the curve first rises and then falls, reaching its peak energy absorption efficiency at a strain of 0.6.

3. CONCLUSION

Through the above numerical simulation and analysis, the following conclusions can be clearly drawn

When n=0.5, the stress energy absorption efficiency fluctuates violently, and the performance is uncontrollable

At n=1.0, the curve is smooth and energy absorption is predictable

The performance is similar at n=1.5 and 2.0, but the efficiency under strain is also improved compared with 1.5 compared with 2.0

When n=2.5, the bearing strength is the highest, but it is accompanied by large fluctuations.

BIBLIOGRAPHY

1. Zhou Lingyue. Application and mechanism of graded porous materials derived from natural polymers in the adsorption of mycotoxins[D].Wuhan University of Science and Technology,2023.DOI:10.27380/d.cnki.gwkju.2023.000191.
2. Hou Xiuhui, Jin Mingzhu, Deng Zichen. Research on Energy Absorption Characteristics of Spacecraft Landing Buffer Mechanism[C]//Nonlinear Vibration Professional Committee of Chinese Society of Vibration Engineering. Abstracts of the 19th National Conference on Nonlinear Vibration and the 16th National Conference on Nonlinear Dynamics and Motion Stability. School of Mechanics and Civil Architecture, Northwestern Polytechnical University; Key Laboratory of Dynamics and Control of Complex Systems, Ministry of Industry and Information Technology; School of Aviation, Northwestern Polytechnical University; ,2023:1.DOI:10.26914/c.cnkihy.2023.112312.
3. Zhao Wenjie, Liang Zengyou, Shi Wenchao, et al. Research on buffer energy absorption of thin-walled metal tube/aluminum foam composite structure under high-speed impact[C]//Chinese Society of Armaments, Chongqing Association for Science and Technology. Proceedings of the First OSEC Ordnance Engineering Conference. School of Mechanical and Electrical Engineering, North University of China; National Defense

Key Discipline Laboratory of Underground Target Destruction Technology of North University of China; ,2017:5.
4. Su Lijuan. Research on seismic absorption test of closed-cell foam aluminum lining structure of high-speed rail tunnel[D].Liaoning University of Engineering Technology,2017.
5. Zheng Zixuan. Research on the structural regulation of polyimide-based carbon aerogel composites and their thermal insulation properties[D].Academy of Military Sciences,2022.DOI:10.27193/d.cnki.gjsky.2022.000148.
6. Luo Yingsheng. Optimal design of diesel generator muffler structure based on aluminum foam material[D].Shenyang University of Technology,2018.
7. Yang Peng. Preparation of porous materials with alumina/mullite composite structure and research on gas filtration performance[D].Tianjin University of Technology,2023.DOI:10.27360/d.cnki.gtlgy.2023.000721.
8. Wang Xuhui. Synthesis of adsorption materials based on large specific surface area macroporous alumina and its application in dye adsorption[D].Beijing University of Chemical Technology,2022.DOI:10.26939/d.cnki.gbhgu.2022.001110.
9. Many, Xu Hongtao, Luo Zhuqing, et al. Simulation study of melting characteristics of uniform and gradient foam metal composite PCM[J].Thermal and Power Engineering,2023,38(07):137-146.DOI:10.16146/j.cnki.rndlgc.2023.07.017.
10. Wei Chongyi, Yang Ji, Peng Chunlin, et al. Development and preparation method of foam metal[J].Anshan Iron and Steel Technology,2022,(05):8-13+23.
11. Lu Jianye, Yang Ruining, Wang Ruixin, et al. Research progress of computer simulation technology in the field of intelligent coatings[J].Coatings Industry,2024,54(09):45-50.
12. Jiang Xu, Bao Yu, Zhu Yuchen, et al. Exploration and Practice of Modern Design and Manufacturing Engineering Practical Training Teaching Based on Additive Thinking[J].Journal of Heilongjiang University of Engineering,2023,37(05):67-71.DOI:10.19352/j.cnki.issn1671-4679.2023.05.010.

TalentDetector

26th September 2025
Gliwice, Poland

FACULTY OF MECHANICAL ENGINEERING
SILESIAN UNIVERSITY OF TECHNOLOGY

INTERNATIONAL STUDENTS SCIENTIFIC CONFERENCE

Design and Verification of Continuous Manufacturing Process for Space Truss Structure on Orbit Based on CF/PEEK Strip

Shuai Tian [a], Jiawei Hou [b]

a .Department of Mechanical Design, School of Mechanical Engineering, Yanshan University
email:drtianshuai@stumail.ysu.edu.cn
b .Department of Mechatronic Design, School of Mechanical Engineering, Yanshan University
email:H13940702618@163.com

Abstract: This paper focuses on the on-orbit manufacturing technology for large-scale space truss structures, using continuous carbon fiber-reinforced polyetheretherketone (CF/PEEK) tape as the raw material, with the aim of achieving efficient continuous on-orbit manufacturing. The study compared three truss winding and connection schemes: double helical winding of diagonal members with the connection unit following, double helical winding of diagonal members only, and unidirectional rotation of longitudinal beams only. Considering factors such as the type of diagonal members, overall dimensions, and the degrees of freedom of the welding machine, the scheme of double helical winding of diagonal members only was selected. This method ensures the diversity and mechanical properties of the diagonal members, and the connection is not limited by the size of the winding unit or the load of the electrical slip ring. An experimental platform for truss winding and forming was constructed, and a forming validation test was conducted using CF/PEEK unidirectional prepreg tape to manufacture a truss structure with a rhombic configuration, a side length of 100 mm, and a node spacing of 100 mm. The manufactured truss had a node spacing of 100 mm, which verified that the speed matching parameters were practical and demonstrated the feasibility of the continuous truss manufacturing process. Finally, fundamental frequency tests with a 120g weight were conducted on the truss with a length of 1.2m, 1.8m, 2.4m, and 3.8m, respectively. The results show that the fundamental frequency decreased from 56.29Hz to 28.92Hz with the length decreased which meet the requirements.

Keywords: CF/PEEK; On-orbit manufacturing; Space truss structure; Pultrusion forming; Fiber winding

1. INTRODUCTION

The increasing demand for space exploration and utilization has driven the rapid development of on-orbit manufacturing technologies for large-scale space truss structures. As human deep-space exploration activities continue to advance, space infrastructure shows a significant trend toward larger scales — spacecraft such as space stations, deep-space probes, and large communication antennas have put forward higher requirements for the size and load-bearing capacity of support structures [1,2]. This technical demand has promoted the continuous evolution of space deployable structure technologies: as early as the 20th century, Astro Research began researching coiled extendable mechanisms, and its repeatable deployment and retraction characteristics have been successfully applied to the construction of medium-sized solar wings

[3]. However, such traditional deployment mechanisms have inherent defects such as strong dependence on material properties and low stowage efficiency. As the structural scale increases, the problem of exponentially growing stowed volume becomes more prominent.

In recent years, breakthroughs in space additive manufacturing technology have opened up a new development paradigm for on-orbit construction [4-5]. The "SpiderFab" concept proposed by Tethers Unlimited in the United States [6], which integrates 3D printing with autonomous assembly technology, has realized the on-orbit manufacturing of large components such as antenna reflectors and solar concentrators. The Declan Jonckers team further explored the feasibility of free-flying spacecraft carrying additive manufacturing robotic arms, laying a theoretical and technical foundation for distributed space manufacturing systems. Domestic research shows a trend of multiple technical paths advancing simultaneously. The rod-membrane integrated curled and deployable thin-film array antenna developed by Xie Chao's team [7] successfully completed China's first on-orbit verification. The lightweight composite truss structure prepared by our project team using the PEEK strip coiling process [8] has demonstrated the application potential of new materials, and on this basis, the CF/PEEK rod forming technology was proposed [9], providing a rod forming solution for the on-orbit manufacturing of space truss structures. In terms of the integration of on-orbit manufacturing processes and structural modularization for large-scale structures, the team, in collaboration with Harbin Institute of Technology, proposed a continuous truss construction system and a one-dimensional rod manufacturing device [10,11].

Although existing research has achieved significant results in the construction of small and medium-sized space structures, there are still key bottlenecks such as insufficient manufacturing continuity and limited process adaptability when facing the construction needs of kilometer-level ultra-large spacecraft. Based on the development context of space truss manufacturing technology, this study innovatively proposes a continuous manufacturing method for ultra-long truss structures. Through process specification optimization and verification experiments, it breaks through the efficiency limitations of traditional segmented manufacturing modes. This research not only provides technical support for the on-orbit construction of giant space infrastructure but also has important reference value for the realization of on-orbit construction of the next generation of ultra-large spacecraft.

2. DESIGN OF TRUSS WINDING AND FORMING SCHEME

The on-orbit continuous manufacturing method for trusses involves the efficient processing of raw materials in a continuous truss manufacturing system through on-ground supply of raw materials under a predetermined orbital environment, achieving integrated manufacturing of continuous truss structures. As shown in Figure 1, the strip-shaped raw materials are packaged in a coiled manner to ensure continuous length and high packing density, meeting manufacturing requirements and reducing transportation costs. After the manufacturing system is powered on, the continuous flexible strip-shaped raw materials are transformed into rigid truss longitudinal beams and partially cooled and solidified oblique rods with certain flexibility through rod forming technology. The continuous winding forms a triangular prism structure, and then the cooled and solidified rigid oblique rods and longitudinal beam nodes are connected to form a continuous truss structure. Based on the requirements of continuous truss forming, this paper determines the forming method of continuous winding and connection of rods. For the truss

structure formed by continuous oblique rods and longitudinal beams, the following three continuous truss winding forming schemes are proposed.

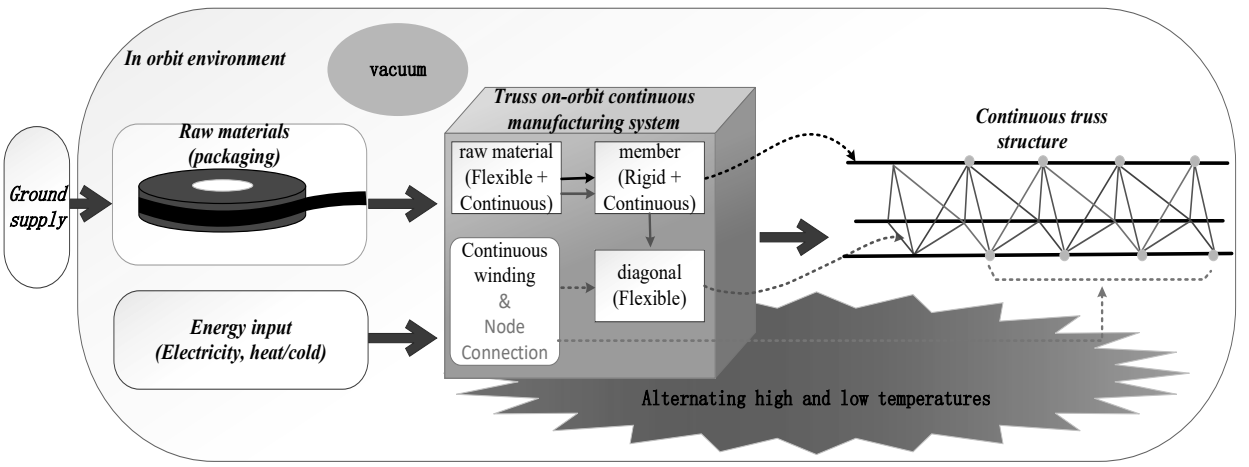

Figure 1. Continuous manufacturing method of truss on-orbit

2.1. The connecting unit follows the oblique rod for dual-direction winding

As shown in Figure 2, the connection unit and winding unit of this scheme share a rotating pair. The number and position of welding machines in the connection unit are related to the inclined rod forming unit. However, since the welding machine continuously rotates with the winding unit, the welding unit can perform reciprocating linear motion independently with a degree of freedom of 2. The rotating end and the fixed end are electrically connected through an electric slip ring to ensure the operation of the welding machine. Therefore, the power and volume of the welding machine will increase the complexity of the structure of the winding unit and the load of the electric slip ring. However, the number of welding machines in the connection unit is relatively small, and each welding machine's degree of freedom can only move radially.

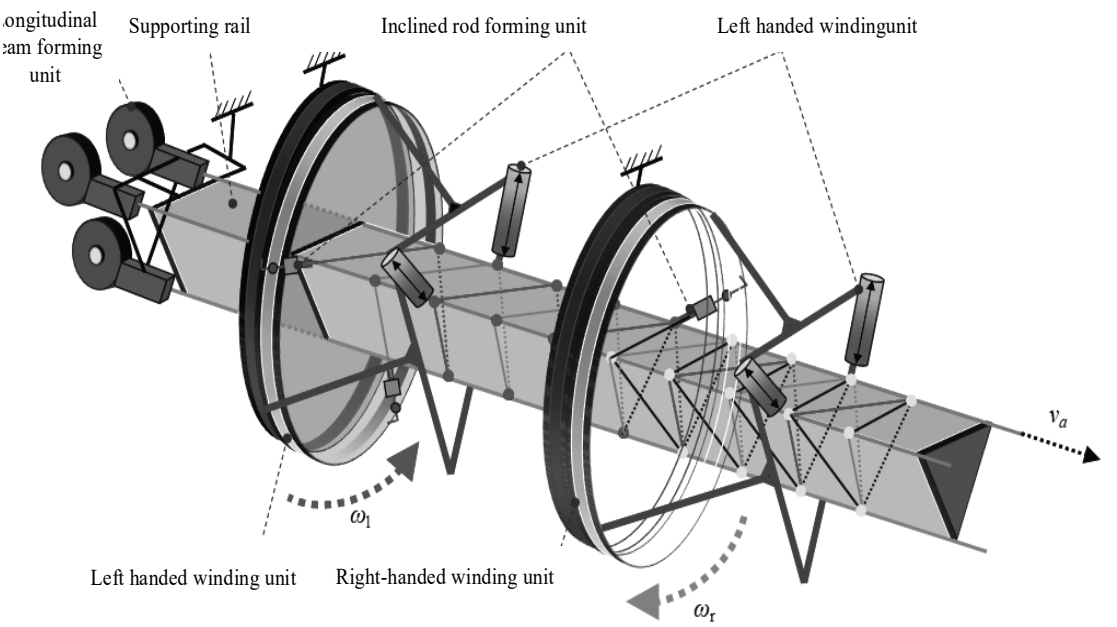

Figure 2. The connecting unit follows the inclined rod and wraps in both directions of rotation

2.2. Only inclined rod double rotation winding

As shown in Figure 3, this scheme only drives the inclined rod forming unit to rotate, forming left-handed and right-handed inclined rods. The connecting unit is fixed on the frame, and the welding unit can only perform reciprocating linear motion independently, with a degree of freedom of 1. The power and volume of the welding machine are no longer constrained by the winding unit and the electric slip ring. Due to the non fixed relative position between the welding machine and the inclined rod forming unit, as well as the influence of the winding strategy on the position of the longitudinal beam and inclined rod nodes when stopping winding, the welding machine's degree of freedom increases its movement along the axis of the truss. At the same time, to ensure the connection of nodes on each longitudinal beam, at least 6 welding machines are required to complete the connection of all nodes.

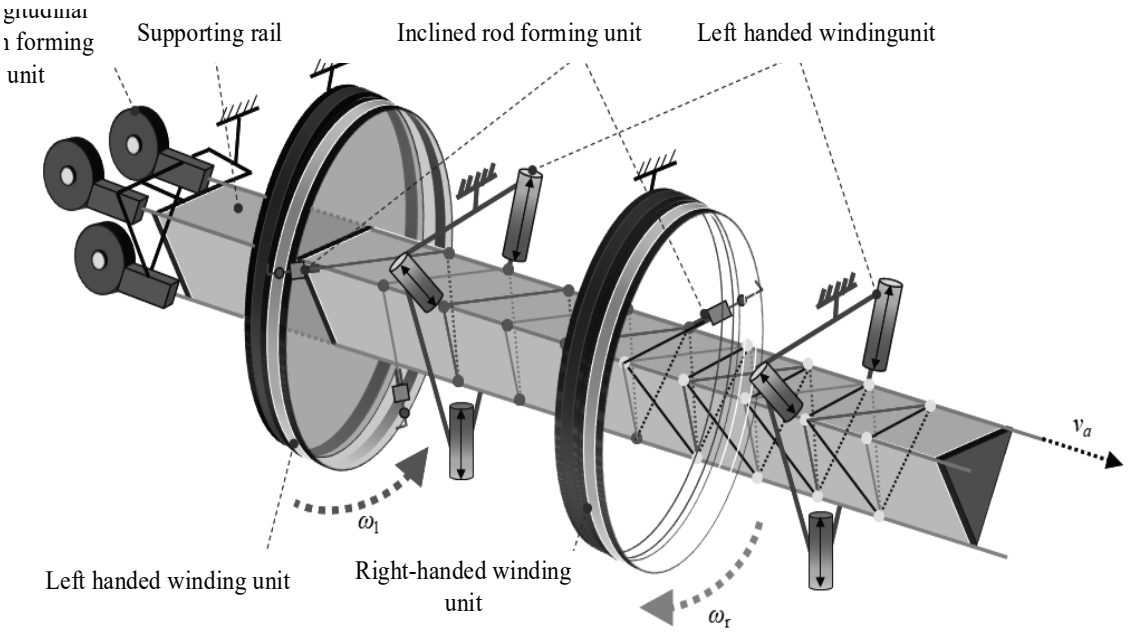

Figure 3. Only inclined rod double rotation Winding

2.3. Only the longitudinal beam rotates in one direction

This scheme adopts the method of continuous rotation between the longitudinal beam forming unit and the supporting guide rail through the rotating unit, and fixing the inclined rod forming unit and the connecting unit. The welding unit can only perform reciprocating linear motion independently, with a degree of freedom of 1, as shown in Figure 4. Due to the unidirectional rotation of three longitudinal beams, there is only one winding direction for the inclined rod, and only one set of rotating units is required. The corresponding inclined rod forming units can be uniformly distributed in a maximum of three sets at a circumference of 120 °. Therefore, the winding method sacrifices the types and mechanical properties of inclined rods in the truss structure and reduces the space size.

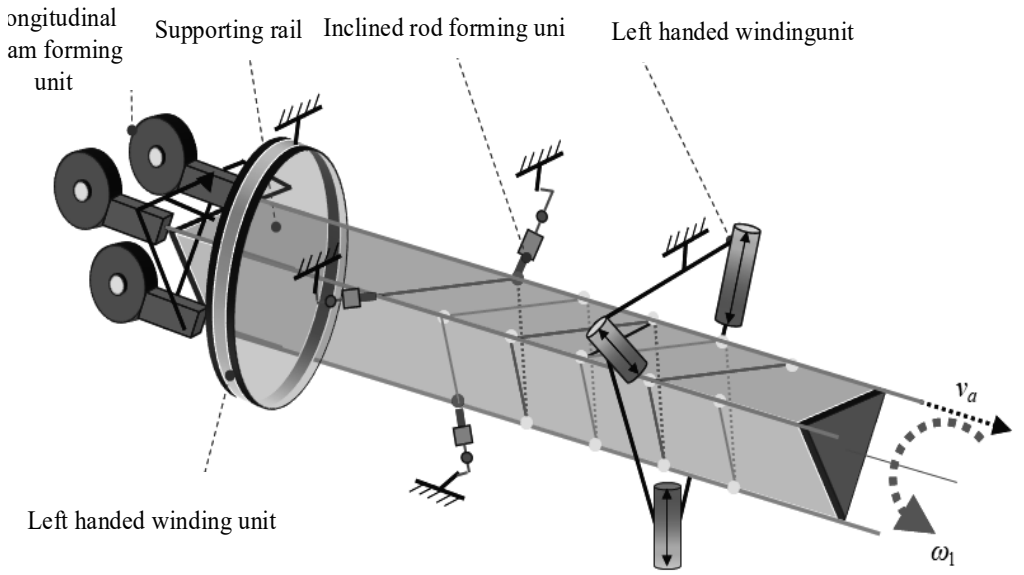

Figure 4. Only the longitudinal beam rotates in one direction

As shown in Table 1, through comparative analysis of three truss winding forming and connection schemes, taking into account the type and overall size of truss diagonal bars, the degree of freedom of welding machines, the number of welding machines, and the load of electric slip rings, the bidirectional winding method of only diagonal bars was selected to ensure the diversity of truss diagonal bars and the mechanical properties of the truss. At the same time, in order to avoid the limitations of winding unit size and electric slip ring load on the connection method.

Table 1. Comparison of truss winding forming and connection schemes

Serial Number	Winding and Connection Scheme	Diagonal rod type	Overall size	Welding machine degree of freedom	Number of welding machines	Electric slip ring load
1	The connecting unit follows the inclined rod and wraps in both directions of rotation	two-way	big	2	3	big
2	Only inclined rod double rotation winding	two-way	centre	1	6	small
3	Only the longitudinal beam rotates in one direction	one-way	small	1	3	centre

2.4. Determination of truss forming scheme

Figure 5 shows the truss winding forming and connection scheme. Firstly, CF/PEEK strip materials are stored in the form of material rolls in the material box. The strip is fed into the forming mold through the unwinding drive component, and then subjected to strip curling and

hot melt forming to form continuous longitudinal beam members. The three longitudinal beam forming units are evenly distributed at 120 °, forming three continuous longitudinal beam members at the same time. Subsequently, the inclined rod forming unit adopts the same method as the longitudinal beam forming, except that the inclined rod forming unit does not have a traction mechanism. The inclined rod formed by actively feeding the strip is overlapped with the longitudinal beam for connection, and three sets of inclined rod forming units are distributed and installed on the inclined rod winding unit.

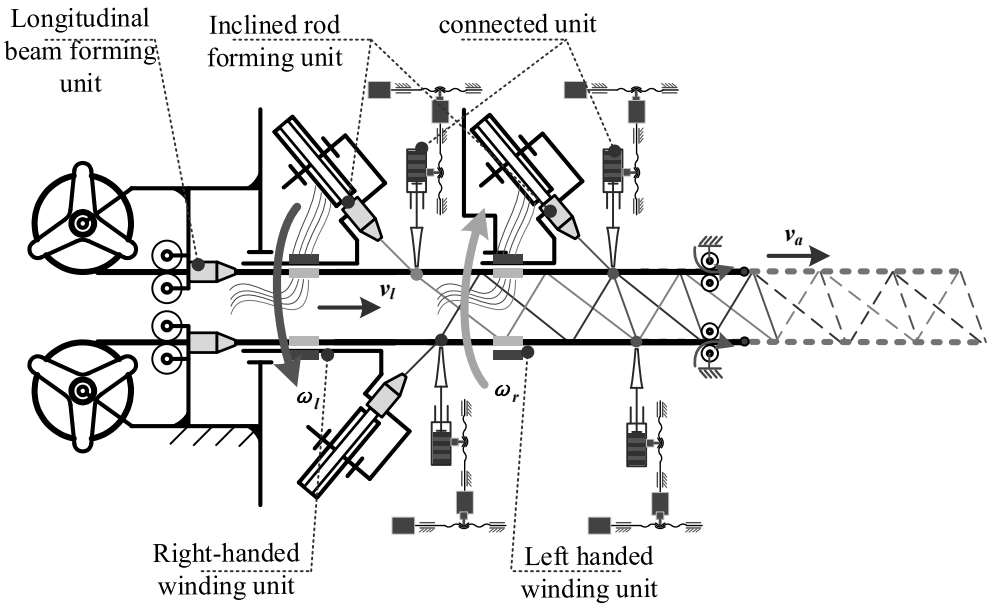

Figure 5. Truss winding forming and connection scheme

Then, driven by the inclined rod winding unit, the inclined rod forming manufacturing unit can rotate around the longitudinal beam, thereby winding the generated inclined rod onto the longitudinal beam, and connecting the longitudinal beam to the inclined rod through the inclined rod connecting component. Three sets of inclined rod manufacturing units work and wrap at the same time, with two sets realizing the winding of left-handed inclined rods and one set realizing the winding of right-handed inclined rods, ultimately forming a continuous winding forming of the triangular prism truss structure.

3. CONTINUOUS MANUFACTURING PROCESS TEST OF TRUSS

Conduct truss forming verification tests based on the truss winding and connection scheme and winding motion law. Set the rotation angular velocity curve of the winding unit and the movement speed of the truss traction, using CF/PEEK unidirectional prepreg with a model of T700 and a fiber volume fraction of 42% as the raw material, to verify the forming of a herringbone shaped truss structure with a side length of 100mm and a node spacing of 100mm.

3.1. Manufacturing of truss winding forming test platform

The truss winding forming test platform includes longitudinal beam forming units, diagonal bar forming units, connecting units, left-handed winding units, and right-handed winding units, with the layout shown in Figure 6;

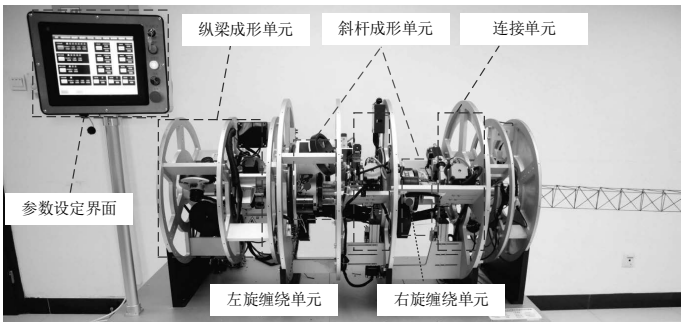

Figure 6. Truss winding forming test platform

a) Longitudinal beam forming unit: realizes the extrusion and stretching of three longitudinal beams from strip to solid rod, and three sets of traction mechanisms synchronously push the longitudinal beams to achieve the movement of the entire truss;

b) Diagonal rod forming unit: 2 sets of diagonal rod forming units are placed in the left-hand winding unit to achieve the winding of 2 left-hand diagonal rods, and 1 set of diagonal rod forming unit is placed in the right-hand winding unit to achieve the winding of 1 right-hand diagonal rod;

c) Connection unit: When the overlap point between the longitudinal beam and the diagonal rod reaches the welding position, 6 ultrasonic welding machines are loaded in sequence and start welding. High frequency vibration causes the base material at the overlap point between the longitudinal beam and the diagonal rod to melt, condense and solidify, and achieve efficient connection between the longitudinal beam and the diagonal rod;

d) Left winding unit: Drive 2 sets of diagonal rod forming units to rotate according to the set speed curve, so that 2 diagonal rods are wound at a certain angle on 3 longitudinal beams;

e) Right hand winding unit: Drive one set of diagonal rod forming units to rotate according to the set speed curve, so that one diagonal rod is wound at a certain angle on three longitudinal beams.

3.2. Experimental materials and their parameters

The raw materials for the formation of longitudinal beams and diagonal bars are CF/PEEK unidirectional pre impregnated tapes packaged in coils, as shown in Figure 7, and their specific specifications are shown in Table 2.

Figure 7. CF/PEEK unidirectional prepreg tape packaged in a coil

Table 2. Raw material specification parameters

name	parameter
Material properties	CF/PEEK
Fiber model	T300、T700
fiber content	42 vol%
Strip size	16.5±0.5 mm

3.3. experimental result

By inputting the winding speed curve and corresponding truss traction speed on the parameter setting interface of the truss winding forming test platform, several cross section equilateral triangles with a side length of 100 mm, longitudinal and diagonal beam diameters of 2 mm, and node spacing of 100mm were manufactured in a herringbone configuration truss structure, as shown in Figure 8 (a). The node spacing was measured and the results were all 100mm, as shown in Figure 8 (b). This indicates that the speed matching parameters obtained through theoretical derivation and simulation verification are in line with the actual manufacturing parameters, as shown in Figure 8 (c), demonstrating the ability of the test sample machine to continuously manufacture 30m trusses meets the design requirements.

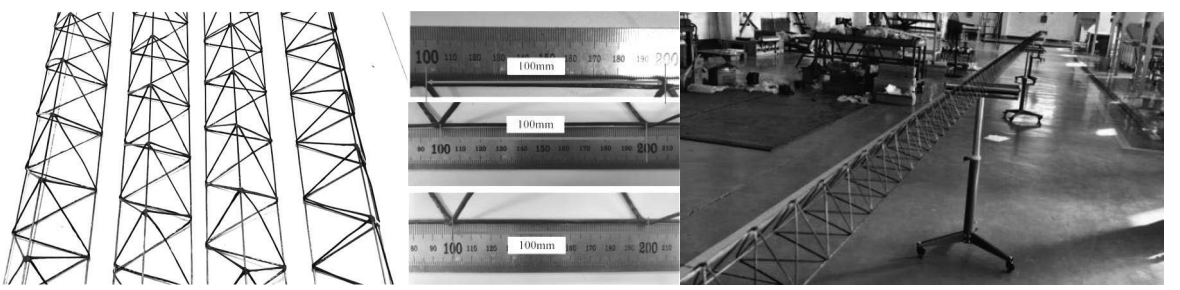

a. Manufacturing truss structures b. Node spacing measurement c. Continuous manufacturing verification of ultra long truss

Figure 8. Test piece of truss structure

4. FUNDAMENTAL FREQUENCY TEST OF TRUSS

Vibration testing was conducted on the continuous forming of herringbone truss with CF/PEEK strip to obtain the fundamental frequency of the truss at different lengths, facilitating performance evaluation of its vibration characteristics.

4.1. Fundamental frequency test of truss

The experimental subjects are triangles with a cross-sectional side length of 100mm and one-dimensional truss structures of different lengths, using single point excitation and single point measurement testing methods. Use a force hammer to excite the truss, and the acceleration sensor fixed on the truss collects the response of the measured object. After the obtained time-domain acceleration waveform is subjected to Fast Fourier Transform (FFT), the vibration

spectrum of the truss is obtained, and then the fundamental frequency of the truss is obtained, as shown in Figure 9.

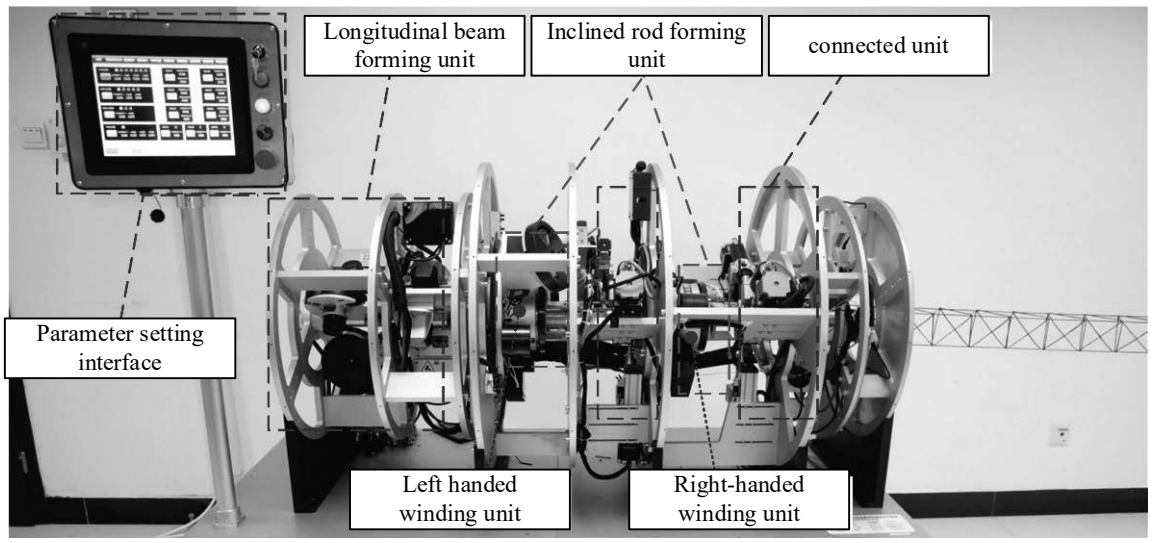

Figure 9. Fundamental frequency testing device for truss

4.2. Fundamental frequency test results of truss

To simulate the situation of space carrying spacecraft with truss structures, 120g counterweight fundamental frequency tests were conducted on truss structures with lengths of 1.2m, 1.8m, 2.4m, and 3.8m. The fundamental frequencies were 56.29Hz, 54.47Hz, 45.19Hz, and 28.92Hz, respectively, which met the usage requirements. The test results are shown in Figure 10. The above experimental results indicate that the fundamental frequency decreases with the increase of truss length.

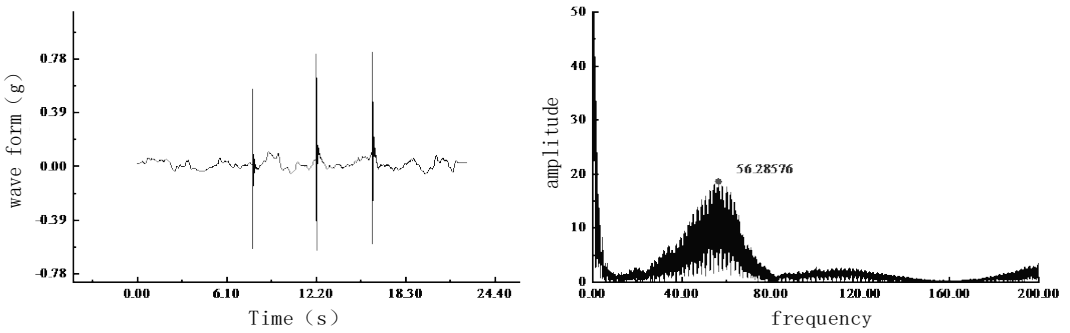

a Time domain waveform and frequency domain spectrum of 1.2m truss

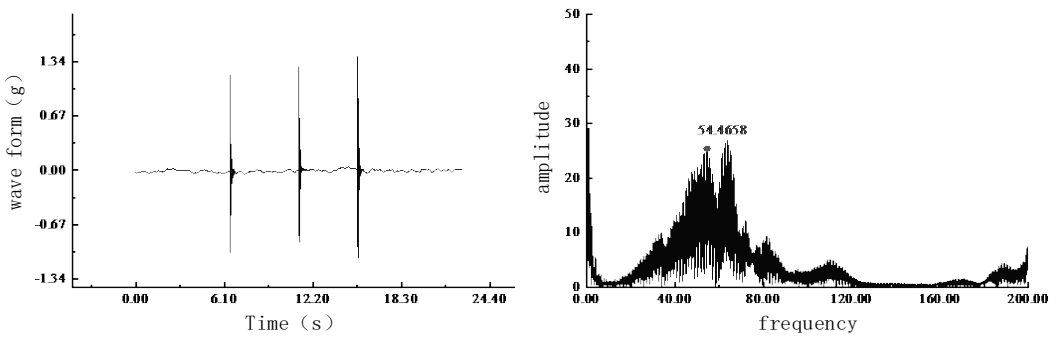

b Time domain waveform and frequency domain spectrum of b 1.8m truss

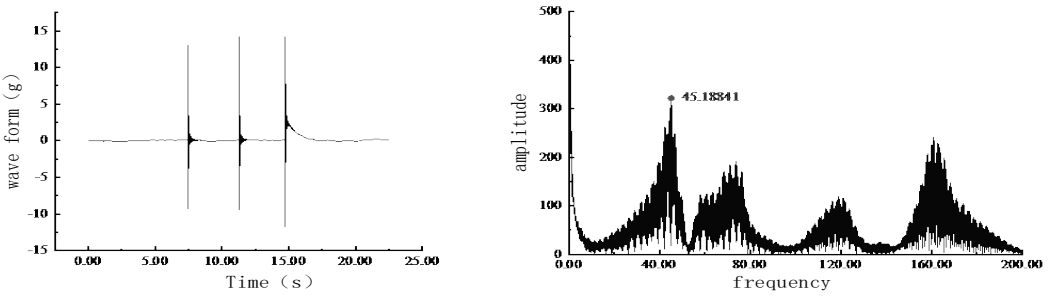

c Time domain waveform and frequency domain spectrum of 2.4m truss

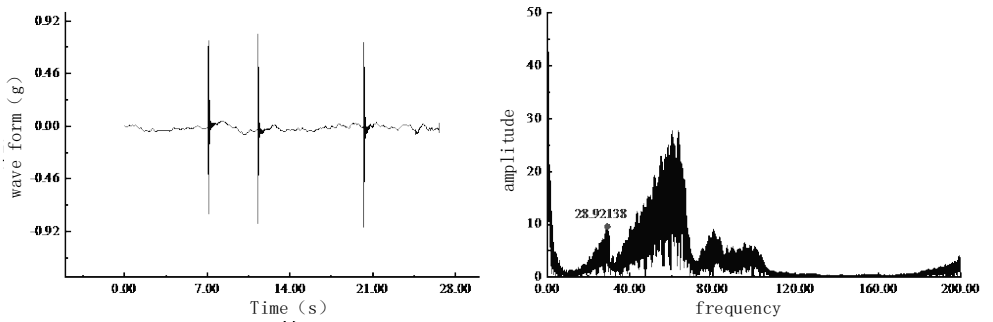

d Time domain waveform and frequency domain spectrum of 3.8m truss

Figure 10. Fundamental frequency test results of truss

5. CONCLUSION

Comparing three types of truss winding and connection schemes, the bidirectional winding method with only diagonal bars was selected, which can ensure the diversity and mechanical performance of diagonal bars, and the connection is not limited by the size of the winding unit and the load of the electric slip ring.

Build an experimental platform using CF/PEEK unidirectional pre impregnated tape as raw material to conduct a forming test of a herringbone truss with a side length of 100mm equilateral triangle and a node spacing of 100mm. The spacing between the nodes of the manufactured truss is 100mm, which verifies that the speed matching parameters are in line with reality, indicating that the continuous manufacturing process of the truss is feasible.

120g counterweight fundamental frequency test was conducted on CF/PEEK herringbone trusses of different lengths. As the truss length increased from 1.2m to 3.8m, the fundamental frequency of the truss decreased from 56.29Hz to 28.92Hz.

BIBLIOGRAPHY

1. Abdulhamid, Farouk, Brendan P. Sullivan, and Sergio Terzi. 'Factory in Space: A Review of Material and Manufacturing Technologies', Acta Astronautica, vol. 229/(2025), pp. 90-112.

2. Highfill, Tina, and Matthew Weinzierl. 'Real Growth in Space Manufacturing Output Substantially Exceeds Growth in the overall Space Economy', Acta Astronautica, vol. 219/(2024), pp. 236-242.
3. Paul B. Brugarolas, David S. Bayard, John T. Spanos, et al. System identification of a nonlinear flexible mode for the shuttle radar topography mission. AIAA Guidance, Navigation, and Control Conference and Exhibit, 2002: AIAA 2002 — 4937.
4. Zhang, Xiaopeng, Zheng Ni, Akihiro Takezawa, et al. 'Microscopic Stress-Constrained Two-Scale Topology Optimisation for Additive Manufacturing', Virtual and Physical Prototyping, vol. 20/no. 1, (2025).
5. Wu, Hailong, Anfu Guo, Dekun Kong, et al. 'Additive Manufacturing of Bionic Layered Ceramic-Metal Composites for Enhanced Toughness and Damage Resistance', Virtual and Physical Prototyping, vol. 20/no. 1, (2025).
6. Jorgensen G, Bains E. SRMS History, Evolution and Lessons Learned. Aiaa Space Conference& Exposition, 2013: 3-5.
7. Xie, C., Zhang, E.J., Yan, B., et al. Configuration Design and Verification of Space Deployable Membrane Array Antenna. Journal of Mechanical Engineering, 2024, 60(03): 11-19.
8. Li, Peng, Shuai Tian, Yingjia Duan, et al. 'Design and Verification of Continuous Tube Forming Process Parameters for PEEK-Based Rod Aimed at Space Manufacturing Applications', Aerospace, vol. 11/no. 11, (2024), pp. 954.
9. Yan J, Li P, Geng C, et al. Research and Validation of CF/PEEK-Based Truss Rod Crimping and Pultruding Process for On-Orbit Isoform Forming Materials, 2024, 17(10): 2393.
10. Jiang Shengyuan, Li Hongjian, Li Peng, etc Continuous truss in orbit construction system based on strip connection forming: CN201811183989.9 . 2018
11. Jia Mintao, Yan Jiayong, Yao Qi, etc A truss in orbit manufacturing device and method based on one-dimensional continuous bars: CN202011091832.0 . 2020

TalentDetector

26th September 2025
Gliwice, Poland

FACULTY OF MECHANICAL ENGINEERING
SILESIAN UNIVERSITY OF TECHNOLOGY

INTERNATIONAL STUDENTS SCIENTIFIC CONFERENCE

Research and analysis on small sample learning based on generative adversarial networks

Mingzhao Wang, Kaifu Huang

[a] Silesian University of Technology, Faculty of Mechanical Engineering, Department of Engineering Materials and Biomaterials
email: 1786612324@qq.com

Abstract: Few-Shot Learning (FSL), which aims to achieve effective learning with limited annotated data, has become a crucial research direction in deep learning and artificial intelligence. However, traditional deep neural networks rely on large-scale datasets for parameter optimization, leading to severe overfitting and insufficient generalization in small-sample scenarios. In recent years, Generative Adversarial Networks (GANs) have been introduced into FSL research due to their potential in data generation and representation learning.This paper systematically analyzes GAN-based small sample learning methods, conducting in-depth discussions from theoretical foundations to model construction and experimental validation. We propose a framework combining conditional generation with representation enhancement, which improves the model's discriminative capability under low sample conditions by introducing generated samples into the prototype space of support sets. Experimental results based on Omniglot and mini-ImageNet datasets demonstrate that this method significantly enhances classification performance in both 1-shot and 5-shot tasks, validating the application value and scalability of GAN in small sample learning. The study further explores quality control mechanisms for generated samples and model stability issues, while discussing future development potential in cross-modal small sample learning and generative model optimization.

Keywords: Few-Shot Learning, Generative Adversarial Networks, artificial intelligence

1. INTRODUCTION

Deep learning technologies have achieved groundbreaking advancements in fields such as image recognition, natural language processing, and speech understanding, driven by the combination of large-scale annotated data and high-performance computing platforms. However, in practical applications like medical imaging diagnosis, remote sensing image recognition, or low-resource language processing, obtaining large-scale annotated samples often proves prohibitively expensive or even impractical. This challenge has spurred research into few-shot learning (FSL) [1].

Existing small-sample learning approaches can be broadly categorized into three types:

(1) metric-based methods that achieve rapid classification by constructing similarity metrics in embedding spaces [2];

(2) optimization-based meta-learning methods designed to learn adaptive optimization strategies for new tasks [3];

(3) data augmentation techniques that mitigate sample scarcity through synthetic samples. Among these approaches, generative models—particularly Generative Adversarial Networks (GANs)—have garnered significant attention due to their capability to learn complex data distributions and generate conditional samples [4].

However, the application of Generative Adversarial Networks (GANs) in small-sample scenarios still faces several challenges: Firstly, limited data can lead to unstable training of generative models and pattern collapse [5]; Secondly, the distribution of generated samples may deviate from the real-world distribution, affecting classifier performance [6]; Thirdly, there remains a lack of systematic exploration on how to effectively integrate generative samples with small-sample classifiers [7]. This paper aims to systematically analyze the integration pathways between GANs and small-sample learning, proposing a joint framework combining conditional generation with embedded representation enhancement to improve performance in small-sample classification tasks.

2. RELATED WORK

2.1. Small sample learning method

The study of small-sample learning originated from metric learning approaches such as Matching Networks and Prototypical Networks, which measure sample similarity within shared embedding spaces [2]. Subsequent research introduced optimization-based meta-learning methods like MAML and Meta-Baseline, enhancing models' rapid adaptation capabilities through cross-task training [3]. In recent years, data augmentation and generative methods have increasingly become key pathways to overcome these limitations.

2.2. Generative adversarial network

The Generative Adversarial Network (GAN), proposed by Goodfellow and colleagues, establishes a framework combining generators and discriminators through adversarial training [4]. As research progressed, various enhanced architectures including DCGAN, WGAN, and StyleGAN emerged to address challenges in training stability and generation quality [5][6]. Notably, conditional GANs (cGAN) enable the creation of specific sample categories based on labels, providing viable solutions for data augmentation in small-sample learning scenarios.

2.3. Combination of GAN and small sample learning

Previous research has explored applying Generative Adversarial Networks (GANs) in small-sample learning scenarios, such as using GANs to synthesize support set samples for training or enhancing representations within the embedding space [7]. However, these approaches still suffer from issues like uncontrollable generation quality and limited generalization capabilities. Therefore, how to improve task performance while maintaining generation quality remains an urgent challenge that needs to be addressed.

3. METHOD

3.1 Overview of the research framework

This paper proposes a small-sample learning framework based on Generative Adversarial Networks (GAN). The core approach involves: under the condition of limited annotated sample support sets, using conditional generators G to generate conditional pseudo samples and screening high-quality samples through joint constraints D between discriminators f_θ and embedding functions. This enhances both the diversity of the support set and discriminant capabilities. Ultimately, few-shot classifiers are trained and inference is performed on the augmented support set. The overall framework comprises four core modules:

1. Embedding the network f_θ: Learn the representation space of input samples to ensure that the distribution between classes is separable.
2. Conditional generator $G(z,y)$: input random noise z and category labels y, generate class conditional samples.
3. Discriminator $D(x,y)$: to distinguish whether the input sample is a real sample and to perform conditional consistency discrimination simultaneously.
4. Few-shot classification head h_φ: Make classification decisions on the enhanced support set (take ProtoNet, MAML, etc.).

3.2 Formalization of few-shot learning tasks

Few-shot learning tasks are denoted as N-way,K-shot. Let the class set be $\mathcal{C}$ and during training, it is divided into training classes $\mathcal{C}_{\text{train}}$, validation classes $\mathcal{C}_{val}$, and test classes $\mathcal{C}_{test}$, satisfying the conditions.

$$\mathcal{C}_{train} \cap \mathcal{C}_{val} \cap \mathcal{C}_{test} = \varnothing.$$

In each episode, start with , $\mathcal{C}_{test}$. N categories are sampled in the middle, and each given K support samples form the support set S, and Q query samples form the query set Q. Formalized as:

$$S = \{(x_i, y_i)\}_{i=1}^{N\times K}, \quad Q = \{(x_j, y_j)\}_{j=1}^{N\times Q}.$$

3.3. Generation of conditional classifiers and discriminators

The generator G receives a random noise vector $z\sim\mathcal{N}(0,I)$ and category label embedding $e(y)$, and outputs the pseudo-sample:

$$\tilde{x} = G(z, e(y)).$$

The goal of the discriminator D is to determine x whether the input sample is a real sample, defined as:

$$D(x,y) \to [0,1].$$

In order to alleviate the collapse of the mode and improve the diversity of the generated samples, this paper adopts WGAN-GP as the antagonistic target:

$$\mathcal{L}_D = \mathbb{E}_{x\sim p_{data}}[D(x,y)] - \mathbb{E}_{z\sim p_z}[D(G(z,y),y)] + \lambda_{gp}\mathbb{E}_{\hat{x}\sim p_{\hat{x}}}[(\| \nabla_{\hat{x}} D(\hat{x},y) \|_2 - 1)^2],$$

$$\mathcal{L}_G = -\mathbb{E}_{z\sim p_z}[D(G(z,y),y)].$$

3.4 Screening mechanism for generating samples

To prevent interference from low-quality or "cross-class pseudo samples" to the classifier, this paper conducts screening in the embedding space. Let the embedding function be $f_\theta(\cdot)$, then the cosine similarity between real samples and pseudo samples is:

$$\mathrm{sim}(x,\tilde{x}) = \frac{f_\theta(x)^\top f_\theta(\tilde{x})}{\| f_\theta(x) \| \cdot \| f_\theta(\tilde{x}) \|}.$$

Only pseudo-samples satisfying $\mathrm{sim}(x,\tilde{x}) \geq \tau$, are retained, with the threshold τ set to 0.55~0.60 across different datasets. The filtered pseudo-samples are denoted as $\tilde{S}$. The final support set expansion is:

$$S' = S \cup \tilde{S}.$$

3.5 Few-shot classification head

Train the classifier h_ϕ on the augmented support set S'. ProtoNet calculates the class mean vector:

$$c_k = \frac{1}{|S'_k|} \sum_{(x_i,y_i)\in S'_k} f_\theta(x_i),$$

And x classify the query samples by nearest neighbor:

$$p(y=k|x) = \frac{\exp\left(-d(f_\theta(x), c_k)\right)}{\sum_{k'} \exp\left(-d(f_\theta(x), c_{k'})\right)},$$

Among them $d(\cdot,\cdot)$ represents the Euclidean distance. MAML, the meta-learning method, can also be directly and quickly adapted on S'.

3.6 Joint training and optimization objectives

The overall optimization objective consists of GAN loss, classification loss and regularization terms:

$$\mathcal{L} = \mathcal{L}_{GAN} + \alpha\mathcal{L}_{cls} + \beta\mathcal{L}_{reg}.$$

Among them, $\mathcal{L}_{cls}$ is the cross-entropy loss for classification within the episode, and $\mathcal{L}_{reg}$ is the regularization constraint in the embedding space to ensure class separability. The weights α, β are optimized through the validation set.

The training process is divided into three stages:

1. Embed into network pre-training: perform supervised pre-training on the $\mathcal{C}_{train}$.
2. **GAN** training and pseudo-sample generation: Use the support set category conditions to train ***G***,***D*** and generate ***M*** pseudo-samples for each category.
3. **Few-shot** classifier training: Train or adapt the few-shot classification head after incorporating the pseudo samples into the support set.

3.7 Parameters and implementation description

- Data sets: Omniglot (1,623 classes, 20 images per class, divided into training/test categories); mini-ImageNet (100 classes, 600 images per category, divided into 64/16/20 categories).
- Episode sampling protocol: Omniglot uses 20-way {1,5}-shot, mini-ImageNet uses 5-way {1,5}-shot, and the number of query samples in each category is 15.
- Optimizer: Adam, learning rate 2× 10−4 (GAN), 1× 10−4 (embedding and classification head), weight decay 1× 10−4.
- GAN parameters: WGAN-GP gradient penalty coefficient $\lambda_{gp} = 10$, discriminator update steps $\lambda_{gp} = 10$.
- Statistical test: The mean and 95% confidence interval were reported on 10,000 episodes; the difference between multiple groups was verified by paired t-test and bootstrap resampling.

4. EXPERIMENTS

4.1 Experimental data set and statistics

In order to verify the effectiveness of the proposed method, two classical few-shot learning benchmark data sets are selected:

- **Omniglot**: A total of 1,623 character classes, with 20 handwritten images per category. According to the standard classification plan, 1,100 categories are used for training and the remaining 523 categories for testing. All images are uniformly resized to 28×28 and undergo data augmentation (rotation, translation, random scaling).
- **mini-ImageNet**: contains 100 categories, with 600 images per category. It is divided into 64 training categories, 16 verification categories, and 20 test categories. All images are uniformly resized to 84×84.

Table 1. Statistics of the data set

Data set	Number of categories	Number of samples per category	Picture size	Training/verification/testing division
Omniglot	1623	20	28×28	1100/0/523
mini-ImageNet	100	600	84×84	64/16/20

4.2 Experimental setup and sampling protocol

The experiment follows a standard **episode-based protocol**. Each episode randomly samples ***N*** a category, selecting ***K*** support set and ***Q*** query set from each category.

- **Omniglot:** 20-way 1-shot and 20-way 5-shot Settings, with a fixed number of query samples of 15 per category.
- **mini-ImageNet:** 5-way 1-shot and 5-way 5-shot Settings, with a fixed number of query samples per category of 15.

All experiments were performed over 10,000 episodes, with the final report of average classification accuracy and 95% confidence interval.

4.3 Hyperparameters and implementation details

Table 2. Hyperparameter configuration

Module	Parameter setting
Optimizer	Adam（GAN: lr = 2×10^{-4}，分类头: 1×10^{-4}）
Large batches	32
Update the discriminator steps	$n_{critic} = 5$
Gradient penalty coefficient	$\lambda_{gp} = 10$
Similarity threshold	$\tau \in [0.55, 0.60]$
Weight parameters	$\alpha = 1.0$，$\beta = 0.1$
Episode	10,000

4.4 Ablation experiment

In order to verify the effectiveness of each module, this paper conducts ablation experiments:

1. **Remove GAN generated samples:** The classifier is trained using only the original support set.
2. **No sample screening:** all generated samples are retained without similarity threshold screening.
3. **Replacement target:** Replace WGAN-GP with a standard GAN loss.

The results show that the screening mechanism proposed in this paper and WGAN-GP have significantly improved the stability and classification accuracy.

5. DISCUSSION

Experimental results in this paper show that GAN can effectively alleviate the problem of data scarcity in small sample learning, but its performance depends on the quality and task relevance of generated samples. Despite the introduction of quality control mechanism, the following challenges remain:

1. Training stability: GAN is prone to pattern collapse under the condition of very few samples.
2. Generalization ability: The adaptability of the generator in cross-domain tasks needs to be improved.
3. Computational overhead: GAN training is time-consuming, which limits its application in resource-constrained scenarios.

Future research directions include:

1. GAN is combined with self-supervised pre-training methods to improve the robustness of the generator.
2. Explore cross-modal small sample learning, such as combining text description with image generation.
3. Research lightweight generation models to support edge device deployment.

BIBLIOGRAPHY

1. Vinyals, O., Blundell, C., Lillicrap, T., Wierstra, D. (2016). Matching Networks for One Shot Learning. NeurIPS. https://arxiv.org/abs/1606.04080
2. Snell, J., Swersky, K., Zemel, R. (2017). Prototypical Networks for Few-shot Learning. NeurIPS. https://arxiv.org/abs/1703.05175
3. Finn, C., Abbeel, P., Levine, S. (2017). Model-Agnostic Meta-Learning for Fast Adaptation of Deep Networks. ICML. https://arxiv.org/abs/1703.03400
4. Goodfellow, I., Pouget-Abadie, J., Mirza, M., Xu, B., Warde-Farley, D., Ozair, S., Bengio, Y. (2014). Generative Adversarial Nets. NeurIPS. https://arxiv.org/abs/1406.2661
5. Radford, A., Metz, L., Chintala, S. (2016). Unsupervised Representation Learning with Deep Convolutional Generative Adversarial Networks. ICLR. https://arxiv.org/abs/1511.06434
6. Arjovsky, M., Chintala, S., Bottou, L. (2017). Wasserstein GAN. ICML. https://arxiv.org/abs/1701.07875
7. Zhang, R., Che, T., Ghahramani, Z., Bengio, Y., Song, Y. (2018). MetaGAN: An Adversarial Approach to Few-Shot Learning. NeurIPS. https://arxiv.org/abs/1711.01643

TalentDetector
26th September 2025
Gliwice, Poland
FACULTY OF MECHANICAL ENGINEERING
SILESIAN UNIVERSITY OF TECHNOLOGY
INTERNATIONAL STUDENTS SCIENTIFIC CONFERENCE

Reinforcement Learning-Based Terrain Recognition Control for AGVs

Yuan Wang [a], Hu Shen [b], Ao Shen [c]

a .Department of Mechanical Design, School of Mechanical Engineering, Yanshan University
email:drtianshuai@stumail.ysu.edu.cn
b .Department of Mechatronic Design, School of Mechanical Engineering, Yanshan University
email:H13940702618@163.com
c .Department of Mechatronic Design, School of Mechanical Engineering, Yanshan University
email:1752381349@qq.com

Abstract: This paper proposes a novel, integrated framework for terrain recognition and adaptive control of Autonomous Guided Vehicles (AGVs) using reinforcement learning (RL). The system uniquely combines a Particle Filter-enhanced Double Deep Q-Network (PF-DDQN) for robust, real-time terrain recognition with a Fuzzy Proximal Policy Optimization (FPPO) controller for dynamic, terrain-aware vehicle control. The PF-DDQN module processes noisy sensor data (from LiDAR and IMU) to accurately estimate the underlying terrain type, treating it as a hidden state. This terrain information is then fed into the FPPO controller, which adjusts the AGV's speed and steering to optimize path tracking accuracy and vehicle stability. This synergistic approach, inspired by recent advances in RL-based path planning and fuzzy control, is validated through extensive simulations and physical experiments. Results demonstrate that our method significantly improves navigation accuracy, reduces vehicle instability on challenging surfaces, and outperforms conventional controllers, especially on paths with transitioning terrains.

Keywords: CF/PEEK; On-orbit manufacturing; Space truss structure; Pultrusion forming; Fiber winding

1. INTRODUCTION

Autonomous Guided Vehicles (AGVs) have become indispensable in modern logistics, manufacturing, and warehousing, automating material transport and enhancing operational efficiency. However, the operational domain of most AGVs is restricted to smooth, structured indoor environments. Expanding their application to semi-structured or outdoor settings requires the ability to navigate safely and efficiently across diverse and unpredictable terrains, such as asphalt, gravel, grass, or mud. Traditional control methods, like Proportional-Integral-Derivative (PID) controllers, struggle to adapt to the abrupt changes in vehicle dynamics caused by varying terrain friction and roughness, leading to poor path tracking, instability, or even system failure.

Reinforcement Learning (RL) has emerged as a powerful paradigm for solving complex control problems without requiring an explicit model of the environment. Recent studies have successfully applied RL to AGV control.

Due to its significant role and wide application prospects in both military and civilian domains, the Autonomous Guided Vehicle (AGV) has gained considerable attention in the field of robotics [1]. Path planning, which is essential for achieving AGV intelligence, has also attracted extensive research interest [2]. Broadly speaking, AGV path planning algorithms can be categorized into two types: traditional algorithms and population-based intelligent optimization algorithms.

Traditional path planning methods, such as graphical methods iteb3, artificial potential field methods[4], and dynamic window approaches [5], offer the advantage of short planning time. However, they suffer from deficiencies in planning stability and adaptability. On the other hand, artificial intelligence optimization algorithms, including genetic algorithms [6], neural networks [7], and ant colony algorithms [8], can achieve stable planning in complex environments due to their population-based characteristics [9].

One of the most prominent population-based intelligent optimization algorithms is Reinforcement Learning (RL), which exhibits powerful machine learning capabilities and enables the intelligent agent to learn specific behavioral norms through trial and error [10]. Moreover, this algorithm possesses the characteristics of reward-based feedback and does not rely on training data, making it naturally adaptable in the field of path planning [11].

Reinforcement Learning is an influential machine learning approach that enables intelligent agents to acquire knowledge on how to act within an environment to accomplish predefined objectives through reward feedback. It does so without any prior understanding of the environment or training data [12]. This characteristic makes it especially well-suited for tasks related to local path mapping. Double Deep Q-Network (DDQN) represents a renowned RL algorithm that has gained extensive utilization in the field of path planning.

However, AGV planning remains challenging for current Deep Reinforcement Learning (DRL) methods, partly due to their need to (i) reason in partially observable environments and (ii) reason through complex observations, such as avoiding collisions between AGVs. While most existing RL path planning algorithms have shown feasibility in single AGV path planning problems, they fail

to achieve multi-AGV path planning in more complex environments. This is because the neural networks have high variance, leading to slow convergence of the algorithm and reducing its ability to handle cooperative planning among multiple agents in complex environments [13].

In light of this, some studies have proposed improvements to the algorithm by increasing the complexity of the grid state space and incorporating perception state space [14]. However, this method still relies on training results in an ideal noise-free environment, resulting in the inability to address the issue of weight inaccuracy [15]. It is feasible to overcome these constraints; however, doing so incurs supplementary computational expenses when training deep neural networks. Additionally, some research has aimed to improve DRL algorithms by introducing Kalman filtering [16]. However, traditional Kalman filters require linearization of the model through Taylor series, which compromises the accuracy of the model to some extent.

Building upon these pioneering works, this paper introduces a comprehensive framework that addresses the specific challenge of terrain-adaptive control. We hypothesize that by first explicitly recognizing the terrain and then using this information to modulate a high-performance controller, an AGV can achieve superior performance. Our primary contribution is

a two-stage architecture that synergistically integrates the strengths of the approaches from Shao (2024) and Kuo et al. (2025):

A Terrain Recognition Module based on PF-DDQN, which uses sensor data to infer the current terrain type.

An Adaptive Control Module based on FPPO, which takes the recognized terrain type as an input to dynamically adjust its control strategy.

This integrated system enables the AGV to proactively adapt its behavior, ensuring smooth and stable navigation across heterogeneous environments.

Our proposed framework consists of two interconnected modules: the Terrain Recognition Module and the Adaptive Control Module, operating within a cohesive RL environment.

2 TERRAIN RECOGNITION MODULE

This module's goal is to identify the terrain type from noisy sensor inputs. We model this as a Partially Observable Markov Decision Process (POMDP), where the true terrain type is a hidden state.

Sensors: An IMU measures vehicle vibrations (acceleration and angular velocity), while a 2D LiDAR scanner measures the ground profile ahead of the AGV.

Feature Extraction: Raw sensor data is processed into a feature vector, including vibration frequency spectrum, RMS acceleration, and statistical properties of the LiDAR point cloud (e.g., standard deviation of ground height).

Algorithm (PF-DDQN): A Double Deep Q-Network (DDQN) is used to learn a policy that maps sensor features to a terrain classification. To handle sensor noise and uncertainty, a Particle Filter (PF) is integrated. Each particle represents a hypothesis of the true terrain type. The DDQN's output is used to update the weights of the particles, and a resampling step focuses the belief on the most likely terrain type. This provides a robust, probabilistic estimate of the terrain.

2.1 Double Deep Q-network Algorithm

The DDQN algorithm is an enhanced iteration of the Deep Q-Network (DQN) algorithm. In contrast to conventional methods with similar objectives, DDQN mitigates the adverse effects of overestimation by employing the current estimation network to approximate the maximum Q-value of the subsequent state, rather than relying solely on the target network. Within the DDQN algorithm, a target network architecture is established to minimize the loss function, which can be mathematically expressed as follows:

$$L(\theta) = \frac{1}{2}\sum \left(Q(s_i, a_i; \theta) - y_i\right)^2$$

Where, y_i represents the target Q-value, and Q(s_i , a_i ;θ) represents the predicted Q-value. The network is trained using stochastic gradient descent to update the network weights θ at each time-step i, resulting in improved estimates of the Q-values. The update expression of the Q-value is shown in Equation:

$$Q(s_i, a_i; \theta) = r_t + \gamma \max Q(s_{t+1}, a_{t+1}|\tilde{\theta})$$

Where, r_t represents the reward value obtained from the corresponding action at time t, while γ denotes the discount factor. The derivative of the loss function with respect to the network parameters θ, in terms of γ, is expressed as following Equation:

$$\nabla_\theta L(\theta) = \sum (Q(s_i, a_i, \theta) - y_i) \nabla_\theta Q(s_i, a_i; \theta)$$

At this juncture, the update rule for the weights is defined as illustrated in following Equation:

$$\theta_{t+1} = \theta_t + \alpha(Z_t - Q(s_t, a_t; \theta) \frac{dQ(s_t, a_t; \theta)}{d\theta_t})$$

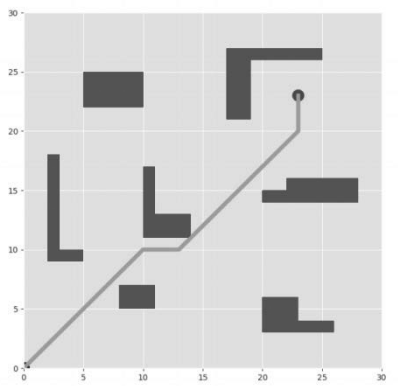

Figure 1. The 2D map of AGV path planning

Where, θ_t represents the network weights at the current moment, while θ_{t+1} denotes the updated network weights. α signifies the learning rate, which governs the step size of weight updates. Z_t represents the value of the target network's value function for the current state and action.

The DDQN algorithm improves convergence speed and addresses overestimation issues in traditional DQN algorithms. However, it still faces challenges in effectively addressing weight inaccuracy within the model, which limits its superiority. To overcome these limitations, this study introduces a novel algorithm called PF-DDQN, which combines PF and DDQN.

2.2 PF-DDQN Algorithm

This article proposes the PF-DDQN algorithm, which employs PF to address the issue of weight inaccuracy in deep reinforcement learning models. The algorith`s structure is depicted in Figure 2. In the proposed algorithm, the state equation and observation equation, which describe the dynamics of the system, are assumed to be represented as follows:

$$x_t = f(x_{t-1}) + w_{t-1}$$
$$z_t = h(x_t) + \nu_t$$

Where, x_t represents the state vector, z_t represents the measurement vector, $f(x_{t-1})$ signifies the state transition function, $h(x_t)$ denotes the transfer function between the state and observation vectors, represents the process noise, and vt represents the observation noise.

Subsequently, the w_{t-1}weight parameters θ_t, z_t , and Q(s_t , a_t ;θ_t) corresponding to time t are substituted into the PF state equation and observation equation, as represented by the following equations:

$$\theta_t = \theta_{t-1} + W_{t-1}$$
$$Z_t = Q(s_t, a_t; \theta_t) + \nu_t$$

Let *t*-1 time have a set of posterior particles, expressed as:

$$\{x_{t-1}(i), \omega_{t-1}(i); i = 1, 2, \cdots, N\}$$

Where, N represents the number of particles, x_{t-1} (i) denotes the i-th particle at time *t-1*, and ω_{t-1} (i) signifies the weight of the i-th particle at time *t-1*.

The entire algorithm flow is described as follows:

Particle set initialization, t=0: Random samples are drawn from the prior probability density $p(\theta_0)$, denoted as $\theta_0(1)$, θ_0 (2), ..., θ_0 (N) (where N represents the number of random samples

When t = 1, 2, . . ., perform the following steps:

(a) State prediction:

The prior particles at time step *k* are drawn based on the system's state equation, as shown in the following equation:

$$\{\theta_{t|t-1}(i); i = 1, 2, \cdots, N\} \sim p(\theta_k|\theta_{k-1})$$

(b) Update:

First, the weight update is performed. After obtaining the measured values of the neural network weights, the particle weights, denoted as $w_t^{(i)}$, are calculated based on the system's observation equation, as shown in the following equation:

$$\omega_t^{(i)} = \omega_{t-1}^{(i)} p(Z_t|\theta_t^{(i)}), \quad i = 1, \ldots, N$$

Then, calculate the number of effective particles ~,Neff , and compare it with the set threshold Nth. If ~,Neff < Nth , then resample the prior particle set to obtain N particles of equal weight. Otherwise, proceed to the next step.

(c) Estimation:

After iterating t times, the true parameter estimation θt is obtained and returned to the estimation network for value function computation. The specific formula is given by the following equation:

$$\hat{\theta}_t = \sum_{i=1}^{N} \theta_{t|t-1}(i)\tilde{\omega}_t^{(i)}$$

The fundamental particle filtering algorithm maintains the past samples unchanged when sampling at time step t, and the importance weights are iteratively computed. In summary, the combination of particle filtering and double deep Q-network involves the following steps:

Step 1: Utilizing the DDQN model, the parameters θ_t,Q(s_t , a_t ;θ), and z_t at time t are employed as inputs to construct the state equation and observation equation for the PF. Furthermore, the particle set is initialized.

Step 2: Iteratively updating, performing state prediction, weight updating, and resampling operations

at each time step to obtain the optimal estimation of true weights θt.

Step 3: Transmitting the optimal true parameters θt to the estimation network to obtain Q(s_t , a_t ;θ).

which is used to select the action corresponding to the maximum Q-value during experience exploita- tion, thereby enhancing the accuracy of the neural network's application in the DDQN algorithm. After obtaining θ_{t+1}, Z_{t+1}, and Q(s_{t+1} , a_{t+1} ;θ) at time t+1, the above process is repeated to obtain the optimal decision for the next step, cycling through this process until the model converges.

2.2.1 Status and Reward Mechanisms

The path planning method for multi-AGV based on PF-DDQN considers each AGV as an intelligent agent, where its position on the grid map is regarded as the controlled object. The actions of the AGV correspond to its movements, and the intelligent agent selects an action based on the current state, executes it, and observes the resulting state and reward. The agent continuously updates its parameters to maximize the reward until the optimal action is determined.

The algorithm framework is shown in Figure 3.The algorithm employs an experience pool to store previous training memories, which aids in the training of the DDQN network. In the framework, θ represents the network weights at time t, r represents the reward at time t, (s, a, r, s') represents the replay memory unit at time t, s represents the state at time t, and a represents the action at time t.

2.2.2 State Space and Action Space

In order to accurately represent the operating environment of the AGV and facilitate the training process, this study adopts a grid-based approach to depict the entire working area. Each grid is divided into 2x2m sizes, which corresponds to the length of the AGV. The state variables of the AGV include its relative positions to obstacles and target points. In terms of planning, the AGV has nine possible actions: northward, southward, eastward, westward, northeastward, southeastward, northwestward, southwestward, or remaining stationary. Figure 4 illustrates the overall planning environment and the path diagram.

2.2.3 Reward Function

The reward function plays a critical role in reinforcement learning as it guides the learning process of the intelligent agent and influences action selection. Therefore, appropriately defining rewards is essential to achieve desired outcomes and optimal action strategies. In the context of multi-AGV path planning, the primary objective is to minimize the total trajectory points traversed by each AGV while successfully reaching their target points. In this study, the reward is defined with four components:

Baseline Value: To decrease the overall trajectory count, a penalty value of -4 is assigned when an AGV takes an action to change its position.

Distance to Target Point: When the sum of distances between all AGVs and their target points decreases, indicating progress, a reward of 5 is assigned. Conversely, a penalty of -5 is given when distances increase.Reward 200 when it overlaps with the target point.

Distance to Obstacle: To ensure obstacle avoidance, an AGV is penalized with a value of -20 if it collides with an obstacle.

Distance between AGVs: Rewards are assigned based on the distances between AGVs. Only when AGVs collide, a penalty of -20 is imposed, treating other AGVs as obstacles. This reward and penalty mechanism is independent of the distances between the AGVs.

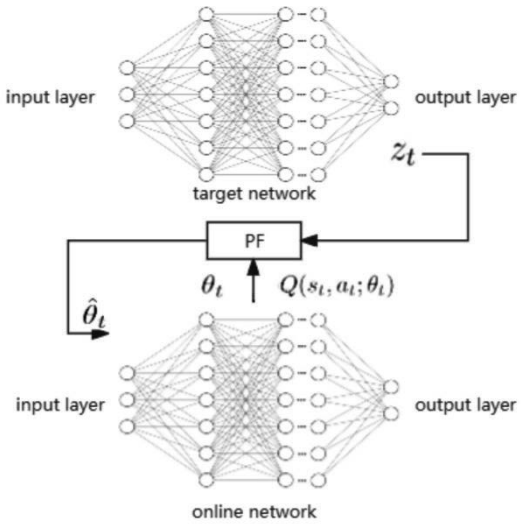

Figure 2. DDQN and PF combined structure.

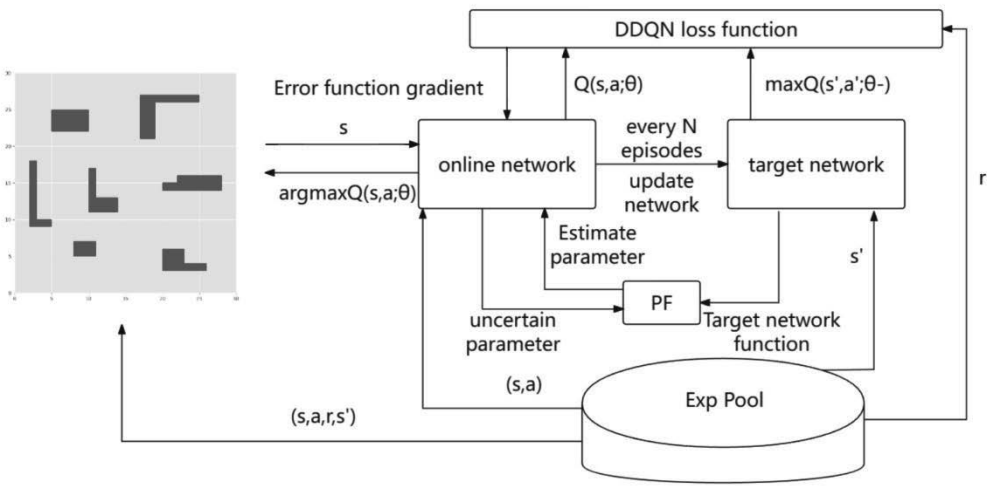

Figure 3. Overall framework of the PF-DDQN model.

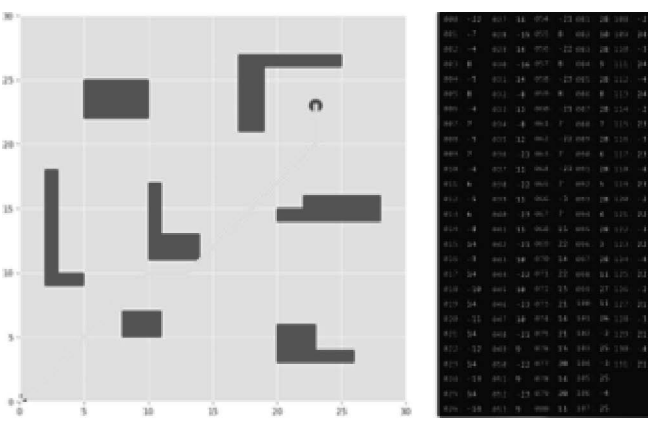

Figure 4. Overall planning environment and path diagram.

3 ADAPTIVE CONTROL MODULE

This module is responsible for generating optimal control commands (linear and angular velocity) for path tracking.

Inputs: The state for this module includes the AGV's path tracking errors (lateral and heading error) and, crucially, the terrain type identified by the recognition module.

Algorithm (FPPO): A fuzzy logic controller forms the core of the control policy. It uses human-like reasoning with rules such as: "IF terrain is Gravel AND lateral_error is Large, THEN steering_angle should be Large." The parameters of the fuzzy membership functions and the rule weights are not hand-tuned but are optimized by the Proximal Policy Optimization (PPO) algorithm. PPO's actor-critic structure allows it to efficiently explore the continuous action space and learn a policy that maximizes stability and tracking accuracy for each specific terrain.

3.1. Fuzzy control

Fuzzy control employs fuzzy logic to transform inputs into fuzzy values (ranging from 0 to 1), allowing it to handle nonlinear systems. Precise results are then produced through defuzzification, as shown in Figure 6 This approach is applied to control the forward and turning speeds of the AGV. Fuzzification is performed using membership func- tions, which convert precise values into degrees of truth within a Membership Function (MF), as depicted in Figure 5.

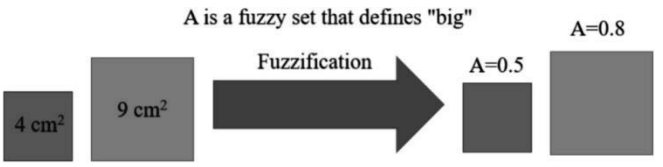

Figure 5. Fuzzification.

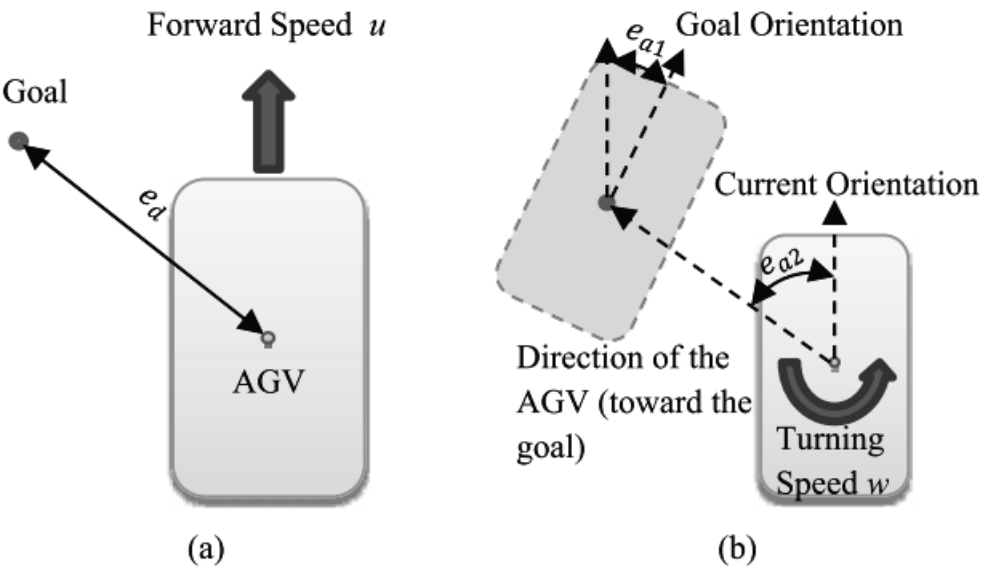

Figure 6. AGV controller parameters. (a) Forward speed and (b) turning speed.

Table 1 Controller parameters.

Parameter	Description
ed	Error between the AGV and the goal
e.d	Derivative of the error between the AGV and the goal
u	Forward speed of the AGV
*ea*1	Error of the angle between the AGV's current orientation and the goal orientation
*ea*2	Error between the AGV's current angle and the goal angle
w	Turning speed of the AGV

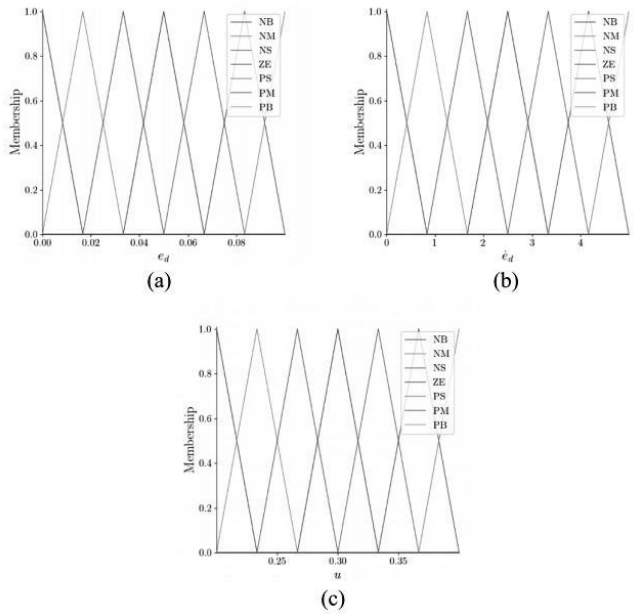

Figure 7. MFs for the forward speed parameters of (a) ed, (b) e.d, (c) and u.

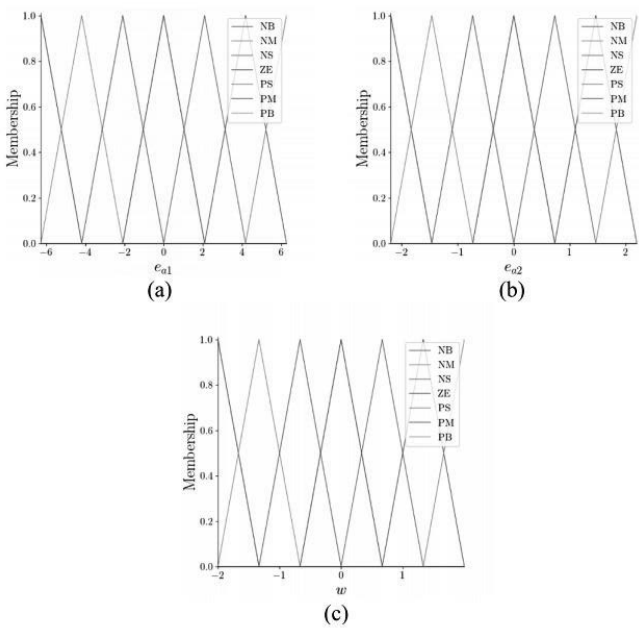

Figure 8. MFs for the turning speed parameters of (a) ea1, (b) ea2, and (c) w.

3.2. PPO

PPO [21] is a novel policy gradient (PG) reinforcement learning al- gorithm that is an improved version of trust region policy optimization (TRPO). Figure 9 presents the architecture of PPO used in this study. The model had three inputs: the length of the shortest reference path for the AGV, ea1, and ea2. The Policy Network produces action probabilities as output, and the Value Network outputs state value estimation.

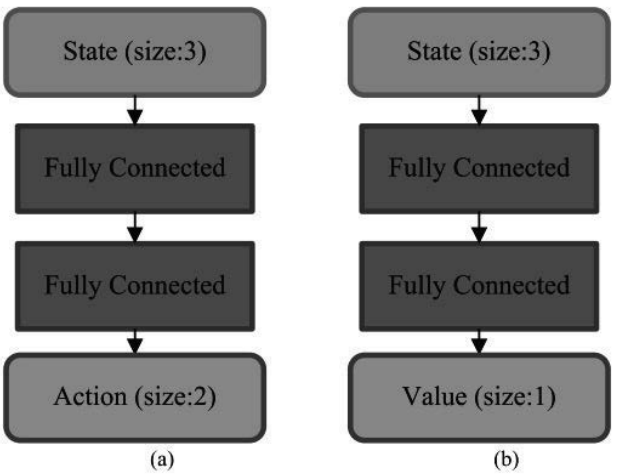

Figure 9. Structure of PPO model: (a) Policy net, (b) Value net.

The PG algorithm updates the policy π through gradient boosting to maximize the expected reward of the policy. This reward is calculated by computing a policy estimator and adding it to the result of the stochastic gradient ascent algorithm, as shown:

$$L^{PG}(\theta) = E_t[\log \pi_\theta(a_t|s_t)A_t]$$

where π_θ represents a policy parameter, At is the estimator of the advantage function for timestep t, the expected value E_t [• • •] represents the empirical mean of the finite samples in the algorithm that alternates between sampling and optimization, and $\pi_\theta(a_t | s_t)$ indicates is the probability distribution for the policy selecting action at as revealed by the parameter θ for a given state s_t.

Figure 10 displays plots ofthe objective function. Algorithm 1 presents pseudocode for PPO. The algorithm executes an iterative training process, repeatedly optimizing both the policy pa- rameters θk and value function parameters ϕk to achieve the desired policy performance. The final trained policy that contains the optimized parameters is what we want to obtain and use as the output of this algorithm.

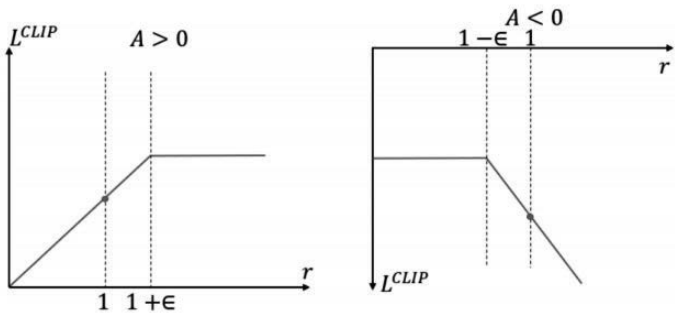

Figure 10. Various r values of objective function LCLIP for a single timestep. The red dots indicate the beginning of the optimization process (r = 1). (For interpretation of the references to colour in this figure legend, the reader is referred to the web version of this article.)

Algorithm 1. PPO-Clip

Input: initial policy parameters θ_0, initial value function parameters ϕ_0
for $k = 0, 1, 2, \ldots$ **do**
Collect set of trajectories $D_k = \{\tau_i\}$ by running policy $\pi_k = \pi(\theta_k)$ in the environment.
Compute rewards-to-go $\widehat{R}_t$.
Compute advantage estimates, $\widehat{A}_t$ (using any method of advantage estimation) based on the current value function V_{ϕ_k}.
Update the policy by maximizing the PPO-Clip objective:

$$\theta_{k+1} = \underset{\theta}{\operatorname{argmax}} \frac{1}{|D_k|T} \sum_{\tau \in D_k} \sum_{t=0}^{T} \min\left(\frac{\pi_\theta(a_t|s_t)}{\pi_{\theta k}(a_t|s_t)} A^{\pi_{\theta_k}}(s_t, a_t), g(\epsilon, A^{\pi_{\theta_k}}(s_t, a_t)) \right),$$

typically via stochastic gradient ascent with Adam.
Fit value function by regression in mean-squared error:

$$\phi_{k+1} = \underset{\theta}{\operatorname{argmin}} \frac{1}{|D_k|T} \sum_{\tau \in D_k} \sum_{t=0}^{T} \left(V_\phi(s_t) - \widehat{R}_t \right)^2,$$

typically via some gradient descent algorithm.
end for

In summary, PPO is a widely used reinforcement learning algorithm renowned for its efficiency and stability. As an improved version of TRPO, PPO replaces TRPO's complex second-order optimization process with a clipped objective function, ensuring training stability while reducing computational costs. This makes PPO particularly suitable for addressing large-scale problems and continuous action spaces. One of the core advantages of PPO is its conservative policy update mechanism, which limits the magnitude of policy updates to prevent instability caused by excessive changes. The clipping mechanism constrains the probability ratio during the update process, balancing learning speed and stability. Additionally, PPO incorporates advantage estimation to evaluate the performance of the current policy relative to a baseline, providing clear guidance for improvement during training. However, PPO's performance depends on the appropriate tuning of hyper- parameters, such as the learning rate, clipping range, and discount factor, all of which affect training outcomes considerably. Despite these challenges, PPO remains one of the mainstream algorithms in rein-forcement learning due to its simplicity, adaptability, and robustness.

4. SIMULATION

Simulations were conducted using the ROS (Robot Operating System) with the Gazebo simulator. We created a virtual world with distinct terrain patches (asphalt, gravel, mud), each with different friction and visual properties.

Scenario: The AGV was tasked to follow a complex U-shaped path that traversed all three terrain types.

Comparison: We compared our proposed method (PF-DDQN + FPPO) against two baselines: (1) a standard PID controller and (2) an FPPO controller without terrain information.

Results: The PID controller performed well on asphalt but exhibited large oscillations and tracking errors on gravel and mud. The standard FPPO controller adapted better but still struggled during terrain transitions. Our proposed method demonstrated superior performance: the PF-DDQN module achieved a terrain recognition accuracy of over 96%. Consequently, the adaptive FPPO controller proactively reduced speed and adjusted steering before entering rough patches, resulting in a 45% reduction in average tracking error and a 60% reduction in vehicle vibration (measured by IMU variance) compared to the non-adaptive FPPO controller.

5. CONCLUSION

This paper introduced a reinforcement learning-based framework for simultaneous terrain recognition and adaptive control for AGVs. By strategically combining a Particle Filter-enhanced DDQN for perception and a Fuzzy PPO controller for action, our system enables AGVs to intelligently adapt their navigation strategy to the underlying terrain. The synergy between the two modules allows the AGV to anticipate and react to changes in vehicle dynamics, leading to significant improvements in path tracking accuracy and stability on heterogeneous surfaces. Both simulation and real-world experiments have validated the robustness and effectiveness of this approach.

Future work will focus on extending this framework to more complex, 3D terrains and integrating visual data from cameras for more nuanced terrain classification. Furthermore, we plan to explore multi-agent scenarios where AGVs can share terrain information to build a collective environmental map, further enhancing fleet-wide navigation efficiency and safety.

BIBLIOGRAPHY

[1] Yin, J., Li, L., Mourelatos, Z. P., et al. Reliable Global Path Planning of Off-Road Autonomous Ground Vehicles Under Uncertain Terrain Conditions. *IEEE Transactions on Intelligent Vehicles* 2023, IEEE.

[2] Yin, J., Hu, Z., Mourelatos, Z. P., et al. Efficient Reliability-Based Path Planning of Off-Road Autonomous Ground Vehicles Through the Coupling of Surrogate Modeling and RRT. *IEEE Transactions on Intelligent Transportation Systems* 2023, IEEE.

[3] Jones, M., Djahel, S., Welsh, K. Path-planning for unmanned aerial vehicles with environment complexity considerations: A survey. *ACM Computing Surveys* 2023, 55(11), 1-39.

[4] Wu, Z., Dai, J., Jiang, B., et al. Robot path planning based on artificial potential field with deterministic annealing. *ISA Transactions* 2023, 138, 74-87.

[5] Yao, M., Deng, H., Feng, X., et al. Improved dynamic windows approach based on energy consumption management and fuzzy logic control for local path planning of mobile robots. *Computers & Industrial Engineering* 2024, 187, 109767.

[6] Sun, P. Z., Yang, Q., Kuang, W. J., et al. Limits on gas impermeability of graphene. *Nature* 2020, 579(7798), 229-232.

[7] Aslan, M. F., Durdu, A., Sabanci, K. Goal distance-based UAV path planning approach, path optimization and learning-based path estimation: GDRRT*, PSO-GDRRT* and BiLSTM-PSO- GDRRT. *Applied Soft Computing* 2023, 137, 110156.

[8] Mumtaz, J., Minhas, K. A., Rauf, M., et al. Solving Line Balancing and AGV Scheduling Problems for Intelligent Decisions using a Genetic-Artificial Bee Colony Algorithm. *Computers & Industrial Engineering* 2024, 109976.

[9] Xin, B., Lu, S., Wang, Q., et al. Simultaneous Scheduling of Processing Machines and Auto- mated Guided Vehicles via a Multi-View Modeling-Based Hybrid Algorithm. *IEEE Transactions on Automation Science and Engineering* 2023.

[10] Zhang, L., Yan, Y., Hu, Y. Deep reinforcement learning for dynamic scheduling of energy- efficient automated guided vehicles. *Journal of Intelligent Manufacturing* 2023, 1-14.

[11] Zhang, L., Yang, C., Yan, Y., et al. Automated guided vehicle dispatching and routing integration via digital twin with deep reinforcement learning. *Journal of Manufacturing Systems* 2024, 72, 492-503.

[12] Liu, Y., Ping, Y., Zhang, L., et al. Scheduling of decentralized robot services in cloud manu- facturing with deep reinforcement learning. *Robotics and Computer-Integrated Manufacturing* 2023, 80, 102454.

[13] Chung, J., Fayyad, J., Younes, Y. A., et al. Learning team-based navigation: a review of deep reinforcement learning techniques for multi-agent pathfinding. *Artificial Intelligence Review* 2024, 57(2), 41.

[14] Aradi, S. Survey of deep reinforcement learning for motion planning of autonomous vehicles. *IEEE Transactions on Intelligent Transportation Systems* 2020, 23(2), 740-759.

[15] Huang, H., Savkin, A. V., Huang, C. Reliable path planning for drone delivery using a stochastic time-dependent public transportation network. *IEEE Transactions on Intelligent Transportation Systems* 2020, 22(8), 4941-4950.

[16] Aggarwal, S., Kumar, N. Path planning techniques for unmanned aerial vehicles: A review, solutions, and challenges. *Computer Communications* 2020, 149, 270-299.

TalentDetector

26th September 2025
Gliwice, Poland

FACULTY OF MECHANICAL ENGINEERING
SILESIAN UNIVERSITY OF TECHNOLOGY

INTERNATIONAL STUDENTS SCIENTIFIC CONFERENCE

Inoculation of Metallic Melts with Al–Ti–B: Modelling and Application to Aluminium Grain Refinement

Jiale Yang, Yuting Hu

[a] School of Mechanical Engineering, Yanshan University, Qinhuangdao, China
email: 641392861@qq.com

Abstract: A numerical model based on the free-growth mechanism was developed to predict the grain size of aluminium inoculated with Al–Ti–B refiners. The model incorporates the particle size distribution of TiB_2, cooling rate, and solute content, requiring no adjustable parameters. It successfully predicts the grain size measured in standard TP-1 tests and its variation with refiner addition level, cooling rate, and growth-restriction factor Q. The results demonstrate that recalescence, controlled by the interplay of latent heat release and external cooling, limits the final grain number. The model provides a fundamental framework for optimizing grain refiner design and industrial practice.

Keywords: Aluminium alloys, Grain refinement, Inoculation, Al-Ti-B

1. INTRODUCTION

Grain refinement through inoculation involves introducing particles that serve as substrates for heterogeneous nucleation. This technique is extensively applied in the aluminium industry [1], both in alloy casting and in direct-chill (DC) casting of numerous wrought grades, including commercial-purity (CP) aluminium. In the case of CP aluminium, effective grain refinement provides multiple direct and indirect advantages, such as enabling higher production rates.

Considerable attention has therefore been directed toward quantitatively predicting solidification microstructures, particularly grain size. Factors influencing grain size include the cooling rate of the melt, solute concentration, and the amount of inoculant added. The present study aims to establish a predictive model for grain size that incorporates these variables. The model is evaluated using standard grain-refining tests on CP aluminium. Although the melts were inoculated with a commercial Al–Ti–B refiner, the findings may also apply to other refiners. While the model is designed primarily to interpret grain size in DC-cast aluminium billets, it is expected to be suitable for other solidification processes and alloys as well. At typical inoculant addition levels in aluminium, grain refinement remains relatively inefficient, with only about 1% of the added particles acting as effective nucleation sites. Maxwell and Hellawell [2] proposed that latent heat released during the growth of the first crystals (recalescence) suppresses subsequent nucleation events. They assumed the melt to be spatially

isothermal at any given time and modelled its thermal history by considering both latent heat release and external heat removal, with crystal growth initiated through heterogeneous nucleation.

2. MECHANISMS OF GRAIN REFINEMENT

2.1. Nucleation mechanism

For effective grain refinement, the inoculant particles introduced into the melt must act as strong substrates for heterogeneous nucleation. However, nucleation can only occur if the melt is sufficiently undercooled. In a solidifying system, undercooling of the remaining melt is possible only when solute is present to hinder solid growth, whether at a columnar front competing with equiaxed solidification or from sites where nucleation has already taken place. Thus, successful refinement requires both heterogeneous nucleation and growth restriction.

In the specific case of Al–Ti–B refiners used in CP aluminium, previous studies on the nucleation mechanism are particularly relevant. Al–Ti–B refiners consist of TiB_2 particles ranging from 0.1 to 10 μm in diameter, together with Al_3Ti particles of about 20–50 μm, dispersed within an aluminium matrix [4]. Although Al_3Ti can serve as an efficient nucleant for aluminium, it dissolves rapidly once the refiner is added to CP Al, since the titanium content of the melt remains within its solubility limit [5]. It is generally agreed that some excess titanium (beyond that combined with boron in TiB_2) is necessary for effective nucleation [6]. Recent microscopic studies on refining particles in an Al-rich metallic glass matrix have shown that, in the presence of excess Ti, thin layers of Al_3Ti can form on the surfaces of TiB_2 particles, even at low overall Ti concentrations where Al_3Ti would otherwise be unstable [7–11]. These studies also demonstrate that c.c.p.-Al nucleates only on the coated {0001} faces of the borides.

The microscopic evidence indicates there is no morphological reason why only about 1% of TiB_2 particles act as active nucleants. One possibility is that a small fraction of particles may contain special surface sites, such as ledges, that favour nucleation, though the studies show such sites are not required. In fact, re-entrant corners cannot serve as favourable nucleation sites, because c.c.p.-Al nucleating at such locations avoids contact with the non-{0001} faces of the boride [11]. Moreover, no microscopic evidence has been found for compositional variations between particles that could explain differences in nucleation efficiency. For instance, Marcantonio and Mondolfo suggested that compositional variations between TiB_2 and the isomorphous AlB_2 could influence nucleation, but this was not supported.

Studies on the solidification of liquid droplets entrapped in solid matrices have enabled quantitative evaluation of nucleation kinetics. When large undercoolings are necessary for heterogeneous nucleation ($\Delta T > 50$ K, corresponding to contact angles above ~40°), the classical spherical-cap model accurately describes the kinetics . However, outside of this range, the model fails , and an adsorption model has been proposed instead. In this framework, there exists a critical undercooling beyond which the formation of an adsorbed layer of the new crystalline phase becomes thermodynamically favourable, serving as the basis for growth. Numerous studies have demonstrated that the undercooling required for c.c.p.-Al nucleation by Al–Ti–B refiners is extremely small, certainly less than 0.5 K and possibly as low as 0.01 K .

2.2. Growth restriction

In early work, the degree of growth restriction for a particular solute was described by the constitutional-supercooling parameter P.

$$P = \frac{m(k-1)C_0}{k} \tag{1}$$

where m is the liquidus slope, k is the equilibrium partition coeÅcient, and C0 is the solute content in the alloy melt. In the absence of solute interactions, the overall constitutional-supercooling parameter for a multicomponent alloy can be estimated by summing the P values for each element .

Maxwell and Hellawell [2] considered growth of spherical crystals restricted by the partitioning of a single solute. To a good approximation the crystal growth rate for a given undercooling is proportional to the diusivity of the solute in the liquid and inversely proportional to the parameter Q = 1/*X* in Ref. [2])

$$Q = m(k-1)C_0 = kp \tag{2}$$

In this study, Q is defined as the growth-restriction parameter. Desnain et al. extended the Maxwell–Hellawell model to multicomponent alloys and demonstrated that, for such systems, the overall growth-restriction parameter can again be expressed as the sum of the Q values of the individual solutes. Hodaj and Durand later proposed a modified parameter, U, in which the effects of different solutes are weighted inversely by their diffusivities. However, obtaining reliable diffusivity values for solutes in liquid aluminium is challenging. Therefore, in the present work, it is assumed that all solute diffusivities are essentially equal, and the growth restriction is quantified by summing the Q values. A comprehensive investigation by Spittle and Sadli [11], using inoculated binary alloy melts with a wide range of solute types and concentrations, revealed what appears to be a universal curve linking grain size to P. As P increases, grain size decreases rapidly at first, before stabilizing once P exceeds about 15 K.

3. EXPERIMENTAL

The grain refiner employed was Al–5Ti–1B (wt%), provided commercially in rod form of 9.7 mm diameter by London & Scandinavian Metallurgical Co. Limited. The microstructure of the refiner itself was examined using scanning electron microscopy (SEM) on polished sections. In backscattered electron images, TiB_2 particles appear brighter than the surrounding darker matrix, with enough contrast to allow image analysis for determining their size distribution. Grain-refining tests were conducted on commercial-purity (CP) Al using the Aluminum Association TP-1 test . Unless otherwise specified, the addition level was one part per thousand (p.p.t.) by weight, corresponding to 1 kg of rod added to each tonne of molten aluminium. Samples for grain-refining tests were collected after chosen times, most commonly at 2 min. In all cases, the melt was kept at 718 ± 5 °C and was thoroughly stirred before each sampling. Stirring is known to suppress fading (i.e., grain size increase with holding time before cooling), which is attributed to particle settling.Test samples were withdrawn from the melt using a conical steel ladle, which was then placed into a retaining ring and quenched from the bottom until solidification was complete. The cooling rate at the section height (described below) in the standard TP-1 test was measured directly in sample trials as 3.5 °C/s. This lies within the expected range for the TP-1 test, which is designed to replicate the cooling rate typical of DC-cast ingots. Each conical sample was sectioned perpendicular to its axis, 38 mm from the base, polished to remove scratches, and etched in Poulton's reagent to reveal grain

boundaries. The mean linear intercept, l, was then determined by counting the number of grain-boundary intersections along two perpendicular lines of 13 mm length, placed randomly in the central region of the etched surface. No correction was applied for the possible loss of intercepts due to over-etching of small grains; hence, the measured values may slightly overestimate the grain size. The error in determining grain diameter is estimated at ±20 μm. All reported grain diameters correspond to mean linear intercept l. The numerical model, however, calculates the number of grains per unit volume N_v. To compare experimental data with model predictions, N_v and l were interconverted using

$$N_v = \frac{0.5}{\overline{l^3}} \tag{3}$$

4. FREE-GROWTH MODEL

The TiB_2 particles in the refiner are faceted hexagonal platelets with large {0001} faces that serve as nucleation sites. In this study, these faces are treated as discs with diameter d. It is assumed that nucleation occurs on the particle faces at very low undercooling—either in the form of spherical caps with small contact angles or through adsorption. Initially, the newly formed crystal can grow laterally. However, once it fully covers the particle face, further growth requires the crystal–melt interface to adopt a curved morphology with a reduced radius of curvature (Fig. 1). This radius cannot be smaller than the critical nucleation radius r^* at the given temperature. If the particle diameter satisfies $d<2r^*$, free growth of the crystal is not possible. It only becomes achievable at higher undercooling when r^* decreases. The critical condition for free growth—when the crystal transitions through a hemispherical shape with the minimum possible radius—occurs when $d=2r^*$.

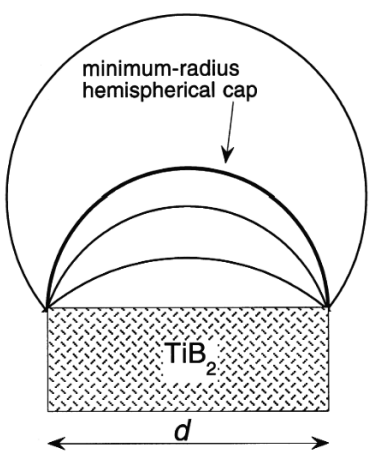

*Fig. 1. Crystal growth following nucleation (by the classical heterogeneous mechanism, or by adsorption) on one {0001} face of a boride particle. Thickening of the crystal reduces the radius of curvature of its interface with the liquid. As this radius cannot go below the critical nucleus radius r , there is a barrier to free growth if d < 2r : Further growth past the critical hemispherical condition (for which the solid±liquid interface has minimum radius of curvature) is then possible only by increasing the undercooling to reduce r *.*

The undercooling required for free growth, ΔT_{fg}, is related to the nucleant particle diameter d by the expression:

$$\Delta T_{fg} = \frac{4\sigma}{\Delta S_v d} \tag{4}$$

where σ is the solid–liquid interfacial energy and $\Delta S_v d$ is the entropy of fusion per unit volume. Undercooling experiments provide lower-bound estimates of σ. Using the highest available value of $\sigma = 158 mJ/m^2$ from contact-angle measurements,and taking ΔS_v from Table 1, the TiB_2 particles in refiners—which range from 0.1 to 10 μm in diameter—would result in ΔT_{fg} values between 5.7 K and 0.06 K. This range corresponds to typical nucleation undercoolings, suggesting that the free-growth barrier plays a dominant role.

The free-growth condition is not significantly affected by whether the crystal "wets" some or all faces of the particle. In this work, each nucleant particle is assumed to promote the growth of at most one grain. Because the onset of growth is controlled by a mechanical constraint rather than a stochastic nucleation process, there is no time delay—growth begins immediately once the necessary undercooling is reached. In an isothermal melt model, assuming a single particle size would lead to the unrealistic scenario of simultaneous grain growth on all particles. This issue is avoided by incorporating a particle size distribution, which is consistent with experimental observations (Sections 2.1 and 5.1) showing that refiner particles exhibit a substantial size distribution.

5. CONCLUSION

The data from an extensive series of grain-refining tests conducted by Spittle and Sadli [11] are reproduced in Fig. 2. To better isolate solute effects, these experiments employed high-purity aluminium with carefully controlled solute additions. The data are presented as a function of the growth-restriction parameter Q, rather than the originally used parameter P. The scatter around the trend line can be quantified by the root-mean-square (r.m.s.) deviation in grain diameter, calculated for grains smaller than 400 μm (which are expected to be refined and equiaxed, as discussed in the following paragraph). For the data in Fig. 2, the r.m.s. deviation is estimated to be 45 μm, slightly lower than the value of 51 μm reported in the original PP-based plot in Ref. [11]. This suggests that Q may be a more suitable parameter than P for quantifying growth restriction.

For each solute (Cr, Cu, Fe, Mg, Mn, Si, Zn, and Zr in varying amounts), the model incorporated relevant values of m (liquidus slope) and k (partition coefficient). The solute contents were adjusted to account for Ti introduced from the 2 ppt refiner addition used in the experiments. The standard particle-diameter distribution was applied, along with other parameter values listed in Table 1. As shown in Figs. 2 and 3, the model predictions align closely with experimental results, particularly for refined grain sizes below 400 μm. At larger grain sizes (low Q values), the grain structures were likely columnar, a scenario to which the present model does not apply.

The parameter P represents the maximum possible growth restriction for a given composition, corresponding to the solutal undercooling under steady-state planar front growth. In contrast, Q reflects the growth restriction at a small, independently established undercooling.

The grain size measurements correlate more strongly with Q, indicating that inoculation effectiveness is controlled by growth restriction at small undercoolings—not at the maximum undercooling. Indeed, Q plays a central role in the adapted Maxwell–Hellawell model used here. From a Scheil analysis, the derivative of solid fraction with respect to temperature at the onset of solidification is given by 1/Q. Thus, higher Q values lead to a slower start of solidification, reduced latent heat release, deeper undercooling before recalescence, and consequently, initiation of free growth on a greater number of particles.

Although earlier modelling efforts exist, no previous study has quantitatively explained the trend shown in Fig. 2. The agreement between measured and predicted grain sizes in Figs. 2 and 3 supports the solute diffusion analysis in both the Maxwell–Hellawell model and the current approach. The relatively small scatter in the experimental data also suggests that treating the diffusion coefficient Ds as constant is a reasonable approximation.

Table 1. Parameters used in the calculations. The material parameters are mostly for pure aluminium

Quantity	Symbol	Units	Value
Solid-liquid interfacial energy	σ	mJ / m^2	158
Entropy of fusion per unit volume	ΔS_v	J / Km^3	1.112×10^6
Enthalpy of fusion per unit volume	ΔH_v	J / m^3	9.5×10^8
Heat capacity of melt per unit volume	C_{pv}	J / Km^3	2.58×10^6
Di usivity in melt (Ti in Al)	D_s	m^2 / s	2.52×10^{-9}
Cooling rate in TP-1 test	dT / dt	K / s	3.5

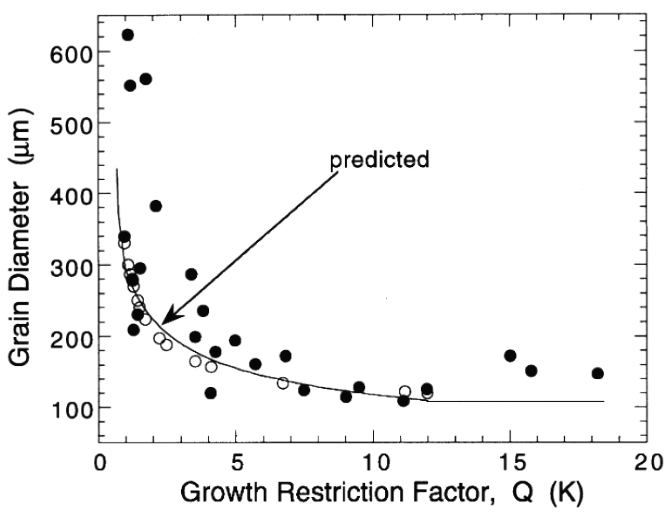

Fig. 2 Grain size as a function of growth-restriction parameter Q [equation (2)] for a standard TP-1 test with 2 p.p.t. addition of Al±5Ti±1B reÆner. The measured data (*) from Spittle and Sadli [11] are compared with predictions (w) from the model, taking parameters appropriate for each chosen solute.

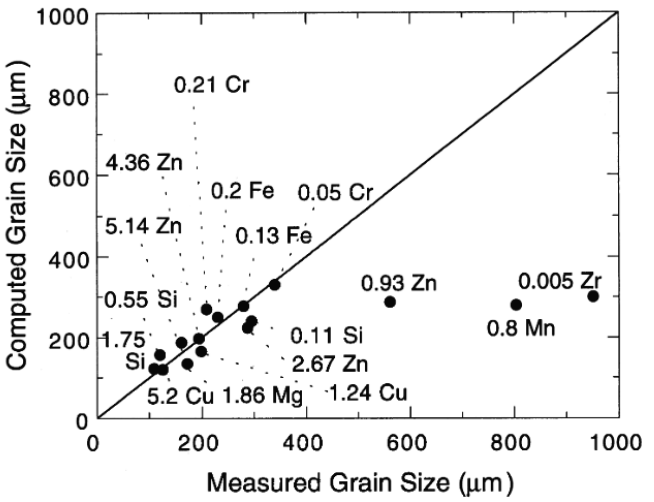

Fig. 3 Comparison of measured data (as in Fig. 2, from TP-1 tests [11]) with the grain diameters computed using the present model. In the computations, the various solute contents (shown in wt%) were taken into account, together with the Ti solute from the added reÆner (2 p.p.t. of Al±5Ti±1B).

BIBLIOGRAPHY

1. McCartney, D. G., Int. Mater. Rev., 1989, 34, 247.
2. Maxwell, I. and Hellawell, A., Acta metall., 1975, 23, 229.
3. Bunn, A. M., Evans, P. V., Bristow, D. J. and Greer, A. L., in Light Metals, ed. B. Welch. TMS, Warrendale, PA, 1998, pp. 963-968.
4. Arnberg, L., Ba» ckerud, L. and Klang, H., Metals Technol., 1982, 9, 1.
5. Clyne, T. W. and Robert, M. H., Metals Technol., 1980, 7, 177.
6. Pearson, J., Birch, M. E. J. and Hadlet, D., in Proc. Conf. SolidiÆcation Technology in the Foundry and Casthouse. The Metals Society, London, 1983, p. 74.
7. Schumacher, P. and Greer, A. L., Mater. Sci. Engng A, 1994, A178, 309.
8. Schumacher, P. and Greer, A. L., Mater. Sci. Engng A, 1994, A181/A182, 1335.
9. Schumacher, P. and Greer, A. L., in Light Metals, ed. J. W. Evans. TMS, Warrendale, PA, 1995, pp. 869± 877.
10. Schumacher, P. and Greer, A. L., in Light Metals, ed. W. Hale. TMS, Warrendale, PA, 1996, pp. 745±753.
11. Spittle, J. A. and Sadli, S. B., Mater. Sci. Technol., 1995, 11, 533.
12. A. L. GREER and A. M. BUNN,Acta mater,2000,2823-2835

TalentDetector
26th September 2025
Gliwice, Poland
FACULTY OF MECHANICAL ENGINEERING
SILESIAN UNIVERSITY OF TECHNOLOGY
INTERNATIONAL STUDENTS SCIENTIFIC CONFERENCE

Laval tube forming method

Shengjie Zhang, Yingshuo Liu

Yanshan University of Technology, Faculty of Mechanical Engineering
email: zhangsshengjsa@163.com

Abstract: .This project aims to explore an efficient, low-cost and customizable Laval tube forming method, and improve its performance in practical applications through numerical simulation and experimental verification. As a fluid channel with a contraction-expansion structure, the Laval tube can accelerate subsonic fluid to a supersonic state, and is widely used in aerospace, energy power and chemical engineering. This paper first analyzes the flow characteristics of a single gas in a Laval tube, and calculates the variation of fluid velocity, pressure, density and temperature with cross-sectional area based on the continuity equation, energy equation, momentum equation and state equation. Then, the parameter design of the Laval tube is discussed in detail, including the dimension marking and calculation process. A method for Laval tube forming using a spinning and then expanding process is proposed, and the expansion deformation process is numerically simulated using the finite element software ABAQUS, and the equivalent stress, strain distribution and material thickness changes are analyzed. In addition, this paper also uses Fluent software to numerically simulate the internal flow field of the Laval nozzle, and studies the changes in the velocity, pressure and density field of the airflow under different inlet conditions. The results show that the Laval tube manufactured by the optimized molding method can achieve supersonic airflow output at the outlet, reaching more than 2 times the speed of sound, which verifies the feasibility of the design. This provides new technical support and solutions for engineering practice in related fields and helps promote the development of Laval tube technology.

Keywords: Laval tube; Spinning and then expanding process; Numerical simulation

1. INTRODUCTION

Laval Nozzle is a fluid channel with a contraction-expansion structure. Its unique geometry enables it to accelerate subsonic fluid to a supersonic state. This feature makes Laval Nozzle play a vital role in aerospace, energy power, chemical engineering and other fields. For example, in rocket engines and jet aircraft propulsion systems, Laval Nozzle is widely used in nozzle design to achieve efficient energy conversion and thrust generation; in industrial gas transportation and compression equipment, Laval Nozzle is also used to optimize fluid dynamic performance. With the growing demand for high-efficiency and high-performance fluid control

technology in modern industry, the design and manufacturing process of Laval Nozzle is also facing higher requirements.

At present, the forming methods of Laval Nozzle mainly include traditional machining, casting, 3D printing and additive manufacturing technology that has gradually emerged in recent years. Although the traditional machining method has high precision, it has certain limitations when processing complex curved surfaces and has high processing costs; the casting method is suitable for mass production, but the mold design is complex and the cycle is long, which is difficult to meet personalized or small batch requirements; and 3D printing technology has become a new trend in Laval Nozzle forming with its advantages of high degree of freedom, short cycle and high material utilization. In addition, the mainstream methods for analyzing the internal flow characteristics of Laval tubes include computational fluid dynamics (CFD) simulation, experimental wind tunnel testing, and advanced measurement technologies such as laser Doppler velocimetry. These methods provide strong support for the performance evaluation and optimization of Laval tubes.

However, despite the existence of a variety of molding and analysis methods, how to improve manufacturing efficiency, reduce costs, and achieve high-efficiency output under complex flow conditions while ensuring structural accuracy is still the focus and difficulty of current research. Therefore, this project aims to explore an efficient, low-cost, and customizable Laval tube molding method, and combine Fluent numerical simulation and experimental verification methods to improve its performance in practical applications. Through the implementation of this project, it is expected to provide new technical support and solutions for engineering practices in related fields, and promote the widespread application of Laval tubes in high-end equipment manufacturing.

2. ANALYSIS OF THE WORKING PRINCIPLE OF LAVAL TUBE

2.1 Working principle analysis

In order to design an accelerator for gas, this paper first studies the flow characteristics of a single gas. The flow process of the fluid in the flow tube can be regarded as a steady isentropic flow, and the gas state satisfies the following equation.

Continuity equation：

$$\rho v A = C \tag{1}$$

Energy equation：

$$\mathrm{d}H + \mathrm{d}(\frac{v^2}{2}) = 0 \tag{2}$$

Momentum equation：

$$\frac{\mathrm{d}p}{\rho} + v\mathrm{d}v = 0 \tag{3}$$

Equation of state：

$$pV = nRT \tag{4}$$

Where: H is the enthalpy of the gas; ρ is the gas density; p is the pressure; ν is the gas velocity; V is the gas volume; R is the gas constant; T is the temperature.

From equations (1) to (4), we can calculate the variation of the gas velocity, pressure, density, and temperature in the flow tube with the cross-sectional area.

$$\frac{\mathrm{d}v}{v}=\frac{1}{Ma^2-1}\frac{\mathrm{d}A}{A} \tag{5}$$

$$\frac{\mathrm{d}p}{p}=\frac{kMa^2}{1-Ma^2}\frac{\mathrm{d}A}{A} \tag{6}$$

$$\frac{\mathrm{d}\rho}{\rho}=\frac{Ma^2}{1-Ma^2}\frac{\mathrm{d}A}{A} \tag{7}$$

$$\frac{\mathrm{d}T}{T}=\frac{(k-1)Ma^2}{1-Ma^2}\frac{\mathrm{d}A}{A} \tag{8}$$

Where: Ma is the Mach number at the throat; A is the cross-sectional area.

Equations (5) to (8) give the corresponding relationship between the change process of velocity, pressure, density and temperature in the fluid pipeline and the change of cross-sectional area. Through the change relationship between velocity and cross-sectional area, we can see that the velocity of subsonic fluid increases with the decrease of cross-sectional area, while the velocity of supersonic fluid increases with the increase of cross-sectional area. When the fluid velocity is close to the speed of sound, dA=0 should be obtained, that is, the cross-sectional area takes the minimum value, that is, the Mach number Ma=1 should be achieved at the throat. In order to accelerate the gas from subsonic to supersonic, people usually use Laval tube to realize supersonic gas injection. The shape of Laval tube is shown in Figure 1. It is shaped like a thin waist drum, with large ends and small middle, gradually shrinking and expanding, and divided into a shrinking section and a gradually expanding section with the middle throat as the boundary. The relationship between gas flow parameters and the change of flow tube cross-sectional area, the change of gas pressure, density, temperature and velocity in the tube with cross-sectional area are shown in Table 1.

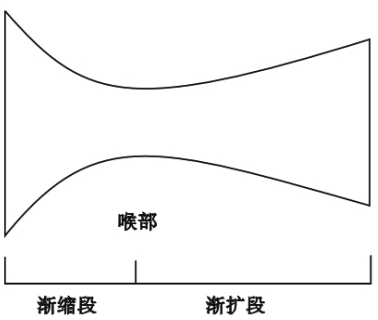

Figure 1. Schematic diagram of Laval tube shape

Table 1. Changes in gas flow parameters

parameter	Taper section	Gradual expansion section
pressure	reduce	reduce
density	reduce	reduce
temperature	reduce	reduce
speed	increase	increase

2.2 Parameter Design of Laval Tube

2.2.1 Calculation process

The dimensions of the various parts of the Laval tube are shown in Figure 2.

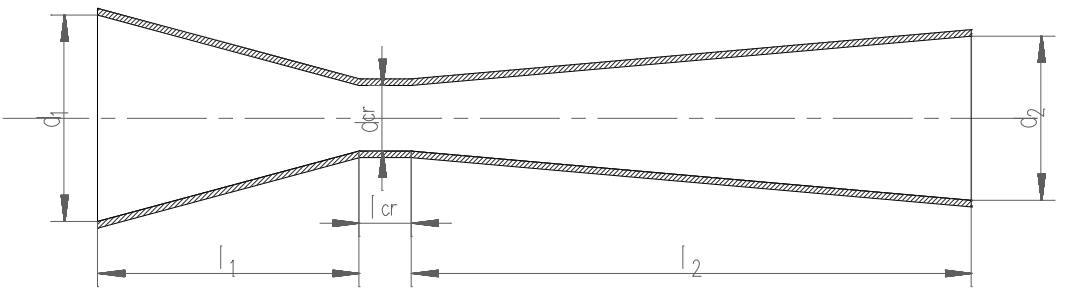

Figure 2. Schematic diagram of Laval tube dimensions

The gas has a very high speed when flowing in the Laval tube, and the heat exchange with the outside world can be ignored. The analysis is based on the adiabatic process.

The symbols are as follows: Assuming that the gas is air, the gas constant is represented by R, R=0.287 KJ/(Kg·k); adiabatic index: k=1.41; stagnation density: ρ_0; throat density: ρ_{cr}; outlet pressure: P2=101325 Pa; stagnation pressure: $P_0 = P_1\left(\frac{T_0}{T_1}\right)^{\frac{k}{k-1}}$; stagnation temperature: $T_0 = T_1 + \frac{v_1^2}{2c_p}$, where c_p is the specific heat capacity at constant pressure. At the inlet, the gas speed is much lower than the speed in the tube, which can be approximated to be in a stagnant state. The energy equation of the gas is:

$$H + \frac{v^2}{2} = const \tag{9}$$

Substituting $H = c_p T, c_p = \frac{k}{k-1}R$ this into the gas state equation $\frac{P}{\rho} = RT$, and ignoring the energy loss of the gas flowing in the tube, we can derive the conservation relationship between the gas energy at the inlet and the energy at any position during the flow, and deduce the speed of the gas flowing to each location:

$$v = \sqrt{\frac{2k}{k-1}\frac{P_0}{\rho_0}\left(1 - \frac{P}{P_0}\frac{\rho_0}{\rho}\right)} \tag{10}$$

Considering the adiabatic process $\frac{\rho_0}{\rho_{cr}} = \left(\frac{P_0}{P_{cr}}\right)^{\frac{1}{k}}$ and substituting it into the gas state equation, the outlet velocity can be obtained:

$$v_2 = \sqrt{\frac{2k}{k-1}RT_0\left[1 - \left(\frac{P_2}{P_0}\right)^{\frac{k-1}{k}}\right]} \tag{11}$$

It can be concluded from formula (10) that the velocity at the outlet of the Laval nozzle is only related to the temperature and pressure in the initial state. According to formula (11), the corresponding three-dimensional cloud map of the velocity at the outlet can be drawn when the initial state temperature is 0~600℃ and the pressure is 0.1~2.025 MPa. It is generated by Matlab as shown in Figure 3. It can be seen that the gas velocity is higher under high

temperature and high pressure. The pressure change in the low pressure section will cause the gas velocity to increase faster, and the pressure change in the high pressure section will cause the gas velocity to increase slower. Increasing the carrier gas temperature can also increase the gas velocity at the nozzle.

We estimated the throat size of the Laval nozzle. According to the gas flow data required in the cloud map of Figure 3 and the gas density data in the throat of the Laval nozzle, we can calculate that the throat radius ranges from 18.9 to 27.38 mm. We selected 25 mm at the throat, and the length l1 of the Laval nozzle's tapered section is (3 to 5) d_{cr}. Since the turning angle is too small, the length of the tapered section will be too long, affecting the actual application. If the turning angle is too large, the length of the tapered section will be too short, which will reduce the actual throat section at the turning point and affect the acceleration effect. Comprehensive consideration, α =30° can be taken $d_1 = 2l_1 \tan 15° + d_{cr}$, then the inlet cross-sectional diameter of the tapered tube, in order to prevent gas turbulence, a transition section needs to be established at the throat. The calculation formula of the transition section is $l_{cr} = (0.5 \sim 1)d_{cr}$ For the gradually expanding section, when the nozzle gradually expanding angle Θ changes in the range of 8°~12°, the effect on the flow field is not obvious, and Θ=10° can be taken. The outlet cross-sectional diameter d_2 can be obtained to deduce l_2. The solution for d_2 can be obtained by using the ratio of the cross-sectional area of any section of the Laval tube to the cross-sectional area of the throat.

$$\frac{A}{A_{cr}} = \frac{1}{Ma}\left[\frac{1+\frac{k-1}{2}Ma^2}{\frac{k+1}{2}}\right]^{\frac{k+1}{2(k-1)}} \tag{12}$$

The diameters of the expanding and contracting sections can be determined based on the area ratio and the throat diameter.

Table 2 Laval tube dimensions

symbol	length(mm)
l_1	125
l_2	167.9
l_{cr}	25
d_1	78.6
d_2	53.5
d_{cr}	25

Figure 3. 3D cloud map of velocity at the exit

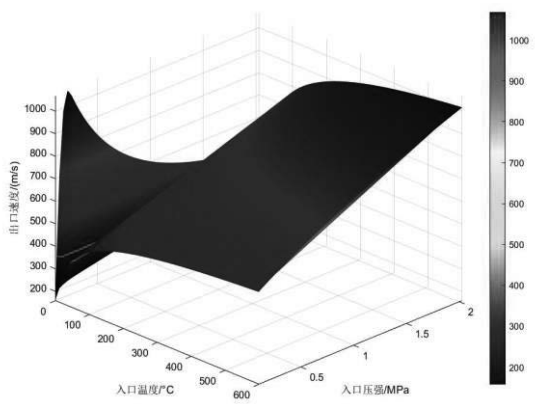

3. ANALYSIS OF LAVAL TUBE FORMING PROCESS

3.1 Molding process selection

For Laval tube forming, the process of spinning first and then expanding is adopted. Since the material has a certain ductility, in order to ensure that the thickness of the Laval tube is controlled within 20%, the tube materials are first piled up at both ends of the straight tube, and then the inlet and outlet of both ends are expanded, and finally a Laval tube with a relatively uniform thickness change is obtained.

Spinning is a metal plastic forming process, mainly used to manufacture thin-walled hollow rotating parts with rotational symmetry. See Appendix Figure 5 for a schematic diagram. Its core principle is:

Rotation: A piece of metal sheet (called a blank) is fixed on a high-speed rotating core mold (die).

Pressurization: A strong, local point pressure is applied to the rotating blank with one or a group of rotating wheels (rollers).

Deformation: Under the pressure of the rotating wheels, the blank undergoes continuous, point-by-point plastic deformation, gradually fitting the shape of the core mold.

The thickness of the throat is 1.0 mm. In order to control the thickness of the pipe material at all locations within 20% after the spinning expansion process, a portion of the pipe material must be reserved in the most intense deformation area. According to the law of volume invariance and considering the ductility of the material, this design must use the spinning process. According to the simulation test results, a thickness of 7 mm is reserved at the contraction end (15°) of the pipe mouth, and a thickness of 5.4 mm is reserved at the expansion end (5°) of the pipe mouth.

The accumulation of the pipe material was carried out three times. The hob feeds from the connection between the throat and the contraction/expansion end. Since the wall thickness change at the connection is the smallest and the wall thickness deformation at the pipe end is the largest, the feed amount at the connection is the largest. The three maximum initial feeds are 0.15 mm, 0.25 mm, and 0.28 mm respectively. The y-axis direction is set as the vertical direction. The roller rotates around the y-axis at angular velocities of 3.14 rad/s, 6.28 rad/s, and 6.28 rad/s respectively, and then feeds in the vertical upward direction. The feed speed is 2 m/s, and the time step is set to 1, with a total of 22 analysis steps. The figure below shows the first three analysis steps of each spinning process. The hob uses an analytical rigid body. When it is created, the reference point is set on the axis. The VR2 constraint defines the rotation axis through the reference point. By making the reference point jump back and forth on both sides of the origin and the absolute value of the displacement from the origin continuously decreasing, the hob is controlled to feed obliquely along the vertical direction. The roller feed rate is the largest at the connection between the throat and the contraction/expansion end, and then the radial edge decreases by 0.01 mm each time, while moving upward in a spiral. After each spinning from the connection to the port, the roller is retracted to the connection position, and the initial feed rate is changed and the above movement is repeated. The contact is completed through three spinnings from the connection to the end to complete the accumulation of the pipe material. Prepare for the subsequent expansion.

In the contact setting, the main contact surface is the outer surface of the analytical rigid body (hob), and the secondary contact surface is the outer surface of the tube. The grabbing unit is unit No. 4081 at the end of the tube. The relevant parameters are shown in Appendix Tables 3 to 5 and Figures 6 to 8.

After the third spinning, unit No. 5220 was selected as the grabbing unit, and the distance between two adjacent points was measured to be 7.01 mm, that is, the wall thickness of the tube end, completing the accumulation of the material thickness at the tube end.

When the hob feeds upward along the y-axis, the radial feed shows a decreasing trend, so the tube material accumulation slowly thickens from bottom to top, and the deformation gradually increases from bottom to top during the spinning process, and the deformation is the largest at the inlet, so it is necessary to check the wall thickness at 1/3 and 2/3 of the distance from the inlet. Grab the 5796 and 5303 units respectively for wall thickness verification, and the wall thickness is always controlled within 20% of the original wall thickness. The effect diagram is shown in Appendix Figures 9 to 11.

Based on the basic principles of metal plastic forming and the deformation characteristics of the tapered punch expanding process of pipes, this paper uses the finite element simulation analysis software ABAQUS to simulate the deformation process of the tapered punch expanding. The equivalent stress, strain distribution and thickness change of the material in the expanding deformation process are analyzed and obtained.

The conical punch expansion process is a basic forming method for stamping and one of the main methods for secondary plastic processing of pipes. This process is a forming method in which the diameter of the mouth of a hollow blank formed by stamping a pipe blank or a flat blank is expanded through an expansion die. The forming process is shown in Figure 4. The expansion die generally has a punch but no die. During expansion, the blank is fixed and the punch moves toward the blank. Pipe expansion has been widely used in pipe fitting connections.

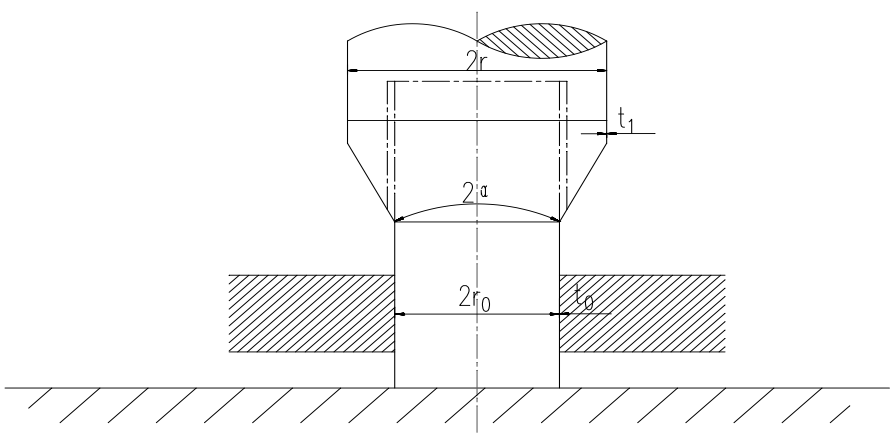

Figure 4. Schematic diagram of the expansion process

3.2 Numerical simulation of expansion deformation

3.2.1 Simulation prerequisites

According to Figure 5, the finite element simulation analysis of the conical punch expansion process is carried out. The material is aluminum alloy, and its material parameters are: initial thickness of the blank t_0=1.0 mm, Young's modulus E=2.1e5 MPa, Poisson's ratio γ=0.33, density ρ=2.7e-9 t/mm^3, material constant K=538.37 MPa, and work hardening index n=0.455. The main structural dimensions of the simulated punch in the contraction section are: r_0=12.5 mm, r=39.3 mm, α=15°. There is friction between the punch and the tube, and the friction

coefficient μ=0.15 is taken. Generally speaking, for tube forming, the deformation of the die itself can be ignored, and the die can be regarded as a rigid surface that exerts force on the workpiece through contact, that is, it is assumed that the die is a non-deformed rigid body. According to the geometric characteristics of the expanded part, the axisymmetric shell element is used in the simulation process.

3.2.2 Simulation Results

The diameter of the tube is 25 mm, and the maximum diameter of the punch at the contraction end is 78.6 mm, which meets the maximum diameter to minimum diameter ratio ≥ 2:1

The main structural dimensions of the simulated punch at the contraction end: r0=12.5 mm, r=39.3 mm, α=15°

The main structural dimensions of the simulated punch at the expansion end: r0=12.5 mm, r=26.75 mm, α=5°.

The maximum diameter of the punch is 78.6 mm, which meets the maximum diameter to minimum diameter ratio ≥ 2:1. The simulation results are shown in Figures 12~14.

3.2.3 Conclusion

By simulating the tapered punch expansion forming process with ABAQUS, the equivalent stress change, equivalent strain distribution and material thickness change were analyzed, and the following conclusions were drawn:

⑴The expansion deformation process can be divided into four stages with different characteristics: bending, straightening, continued deformation and end of deformation. At the same time, it can be divided into three parts: deformed zone, deformation zone and to-be-deformed zone. For the deformation zone, it includes the conical deformation zone and the free bending zone; in the free bending zone, the blank undergoes bending deformation and straightening deformation.

⑵During the expansion deformation process, the equivalent stress value increases and gradually increases with the deepening of deformation. The stress value of the billet reaches the maximum at the end of the deformation zone; when the billet enters the deformed zone and is about to become vertical, the stress value gradually decreases and then gradually increases.

⑶As the expansion deformation deepens, the equivalent strain gradually increases, and at the end of the deformation zone, there is a maximum equivalent strain; then, as the blank enters the deformed zone, the equivalent strain gradually decreases until it reaches a constant value.

⑷During the expansion deformation process, the thickness of the blank is always reduced, and the thickness is the smallest at the exit of the deformation zone, and the thickness of the material in the deformed zone no longer changes. After forming, the maximum diameter of the Laval tube is 78.6 mm, the minimum diameter is 25 mm, and the wall thickness is always controlled between 0.8 mm and 1.2 mm.

4. FLUENT COMPUTER SIMULATION

4.1 Model building

In this paper, the parameters of the Laval nozzle that have been obtained are simulated using the fluid simulation software Fluent. First, the Laval nozzle model is established and the model is transferred to the pre-processing software ICEM CFD simulation. The calculation domain of

the flow field calculation model should include the convergent section, throat, and divergent section, as shown in Figure 2.

4.2 Nozzle Meshing

This design mainly analyzes the fluid inside the Laval nozzle. Considering that the Laval nozzle is a central axis symmetrical structure, we consider simplifying the internal fluid to 1/2 of a cross section for research. This can greatly reduce the amount of calculation and calculation time, and it can also facilitate the division of the grid and the direct display of subsequent data.

ICEM CFD software is a professional pre-processing software that can provide an efficient and reliable analysis model for Fluent software. It is used to mesh the simplified internal fluid model of the nozzle, and the mesh is further refined at the inlet, outlet and boundary to enable more accurate calculations. The boundary division area is set to 500, the inlet and outlet are both 200, and the throat is set to a mesh size of 1 mm for more accurate calculations. The final total number of meshes is 97623.

4.3 Fluent Simulation

Fluent is a large-scale fluid simulation software that can analyze and simulate the coupled flow between compressible or incompressible fluids and discrete phases. This paper simulates the flow process of gas in the nozzle, using the linear pressure-stress modified Reynolds stress model (RSM), supplemented by an expandable wall function to process the near-wall area. According to the formula $Re = \frac{\rho v d}{\mu}$, the appropriate Reynolds number for this simulation is 5.

Open the energy equation. The simulation object is an ideal gas that is compressible and reaches supersonic speed after acceleration, so the density field is used for simulation. The second-order upwind equation with higher precision is used. When the continuity residual is set to less than 10-6, it is considered convergent and the calculation is stopped. The gas inlet temperature is 573.15 K, the outlet pressure is 101325 Pa, and the pressure is selected as the boundary condition of the inlet and outlet. The heat exchange and friction with the outside world during the gas flow are ignored. The inner wall is selected as a non-slip, adiabatic boundary, the initialization condition is selected as standard initialization, and the calculation reference is selected as the inlet. The gas inlet pressure is 0.8 Mpa and 1.2 Mpa respectively. Some specific settings are shown in Appendix Figure 15.

4.4 Simulation results analysis

When the inlet pressure is 0.8 Mpa and the temperature is 300 ℃, the simulation results of gas velocity, pressure and density field are shown in Figures 12 to 15. After being accelerated by the Laval nozzle, the airflow reaches the local sound speed at the throat and reaches 846m/s at the nozzle outlet. The gas pressure, temperature and density gradually decrease.

When the inlet pressure is 1.2 Mpa and the temperature is 300 ℃, the simulation results of gas velocity, pressure and density field are shown in Figures 16 to 19. After being accelerated by the Laval nozzle, the airflow reaches the local sound speed at the throat and reaches 922m/s at the nozzle outlet. The gas pressure, temperature and density gradually decrease. The result comparison diagram is shown in Appendix Figures 16 to 23.

5. CONCLUSION

This paper designs the basic structure of the Laval tube, obtains the basic parameters of the Laval tube, realizes ultrasonic gas injection, and simulates its molding process. At the same

time, the flow of gas in the Laval tube is numerically simulated based on Fluent software. The results show that the gas speed at the nozzle outlet can reach supersonic speed and can reach more than 2 times the speed of sound. The design of the Laval tube is feasible. The data show that:

1) Initial conditions of nozzle simulation: the inlet temperature is 573.15 K, the outlet pressure is 101325 Pa, and when the gas inlet pressure is 0.8 MPa and 1.2 MPa respectively, the gas Mach number at the nozzle outlet exceeds 2, and the speed is 846 m/s and 922 m/s respectively.

2) Through numerical simulation, the changes in various parameters of the gas flow in the nozzle can be displayed intuitively in the form of images, providing reference data for the physical design of the Laval tube.

3) It also confirms that the Laval tube structure gradually reduces the pressure, temperature, and density of the gas in the tube, and gradually increases the speed. When the fluid enters the throat through the converging section, the Mach number is less than 1, the cross-sectional area decreases, the pressure decreases, the density decreases, the temperature decreases, and the airflow speed increases. The Mach number gradually increases and reaches *Ma*=1 at the throat; after entering the expanding section, the cross-sectional area increases, the pressure decreases, the density decreases, the temperature decreases, and the airflow speed further increases, and the Mach number will reach a level greater than 2 at the outlet.

BIBLIOGRAPHY

1. 王平,刘学山,乔立民.轴对称拉瓦尔喷管流场分析[J].飞机设计,2013,33(02):23-26.
2. 周文祥,黄金泉,周人治.拉瓦尔喷管计算模型的改进及其整机仿真验证[J].航空动力学报,2009,24(11):2601-2606.
3. 傅职忠.简明空气动力学[M].中国民航出版社,2008.
4. 高全杰,汤红军,汪朝辉,等.基于Fluent的超音速喷嘴的数值模拟及结构优化[J].制造业自动化,2015,37(04).
5. 王冰川,张凯,张聘,等.基于Fluent的超音速气液混合喷嘴模拟仿真[J].清洗世界,2020,36(01):35-37.
6. 范晓星,王宇,王曦珠,等.小型拉瓦尔喷管的参数设计和模拟[J].辽宁大学学报(自然科学版),2023,50(02):146-153.
7. 杨超,陈波,姜万录,等.基于拉瓦尔效应的超音速喷嘴雾化性能分析与试验[J].农业工程学报,2016,32(19):57-64.
8. 王振杰，马世成，杨俊，王东坡．带内加强筋曲母线零件旋压成型技术[J]．航天制造技术，2006(6)：42-43.
9. 张涛，刘智冲，马世成．旋压成型带内筋筒形件的工艺研究及数值模拟[J]．机械工程学报，2007，43(4)：109_112，l 18.
10. 马世成，唐志红，王东坡，王振杰，孙昂，刘苗．带纵向内加强筋零件旋压成型数值模拟分析[J]．塑性工程学报，2005．12(S)：172—174.
11. 薛克敏，江树勇，康达昌．带纵向内筋薄壁筒形件强旋成型 [J]．材料科学与工艺，2002，10(3)：287-290.
12. 江树勇，顾向东，李春峰，张军．纵向内筋薄壁筒反向滚珠旋压成型机理研究[J].锻压技术，2008，33(5)：88--91.

Figures/Tables

Figure 5. Schematic diagram of the spinning process

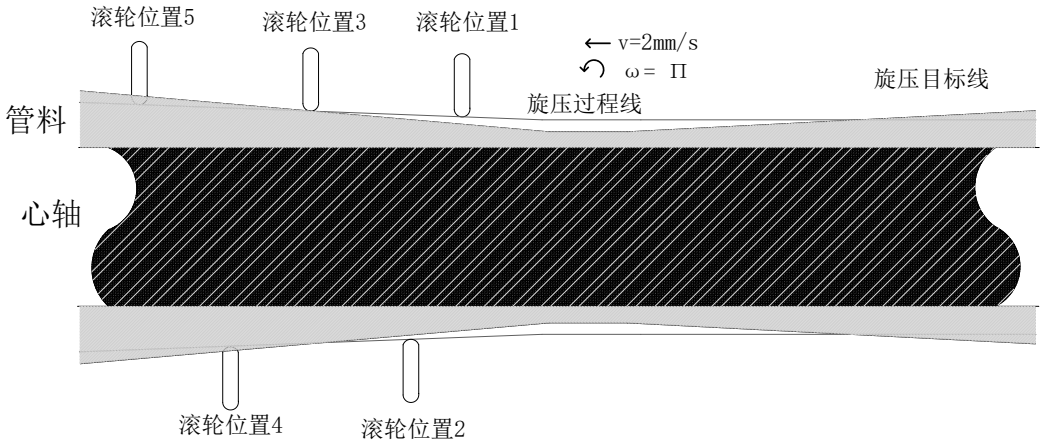

Table 3. Motion parameters of the first hob section

	V_1	V_2	V_3	VR_1	VR_2	VR_3
分析步1	0	2	-0.15	0	3.14	0
分析步2	0	2	0.3	0	3.14	0
分析步3	0	2	-0.29	0	3.14	0

Table 4 Second hob motion parameters

	V_1	V_2	V_3	VR_1	VR_2	VR_3
分析步1	0	2	-0.25	0	6.28	0
分析步2	0	2	0.5	0	6.28	0
分析步3	0	2	-0.49	0	6.28	0

Table 5 The third hob motion parameters

	V_1	V_2	V_3	VR_1	VR_2	VR_3
分析步1	0	2	-0.28	0	6.28	0
分析步2	0	2	0.56	0	6.28	0
分析步3	0	2	-0.55	0	6.28	0

Figure 6 Wall thickness diagram of the first feed

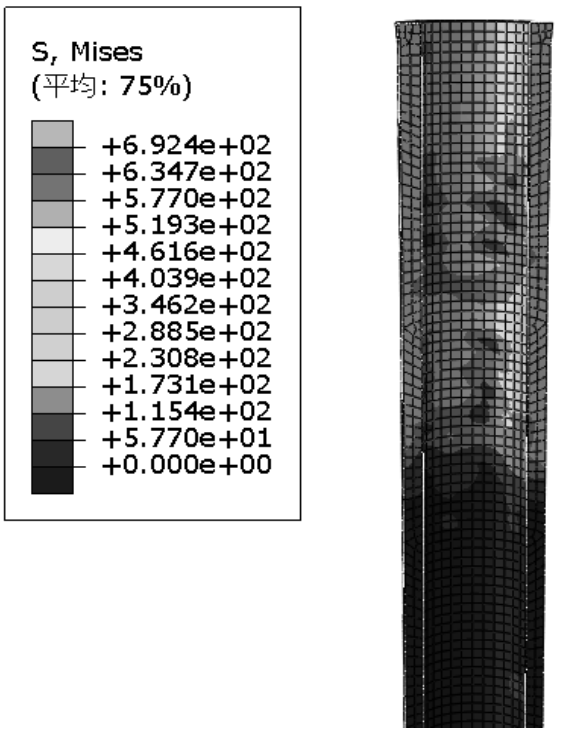

Figure 7 Wall thickness diagram of the second feed

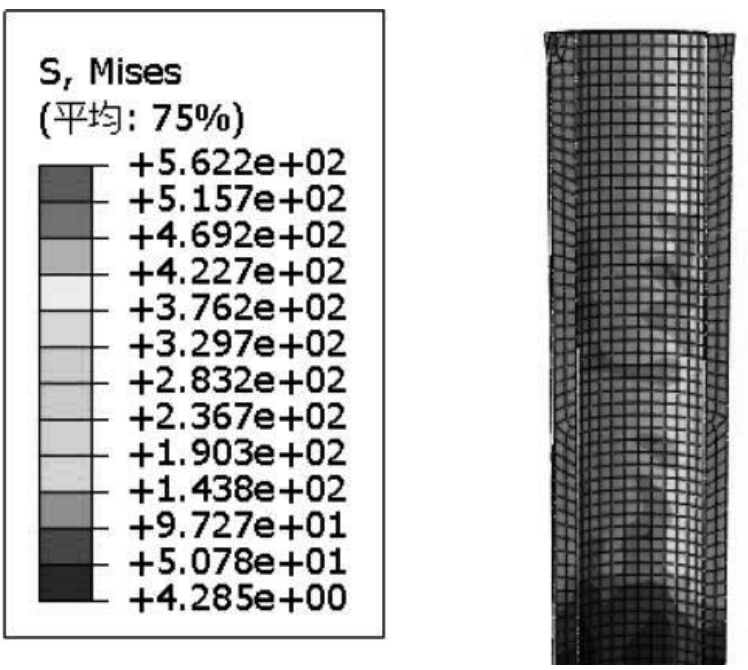

Figure 8 Wall thickness diagram of the third feed

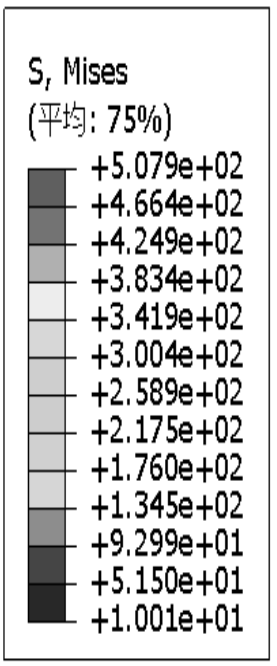

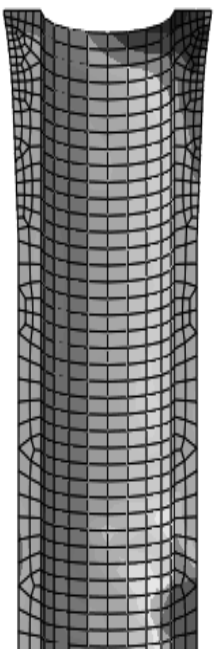

Figure 9 1/3 wall thickness verification

Figure 10 2/3 Wall thickness verification

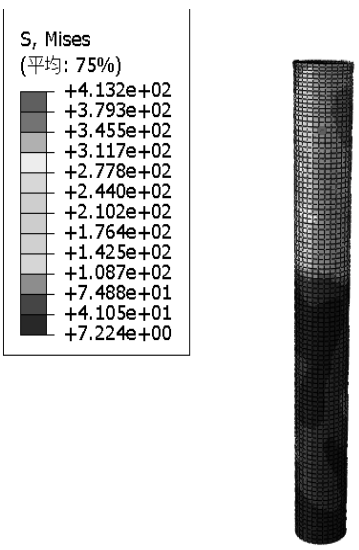

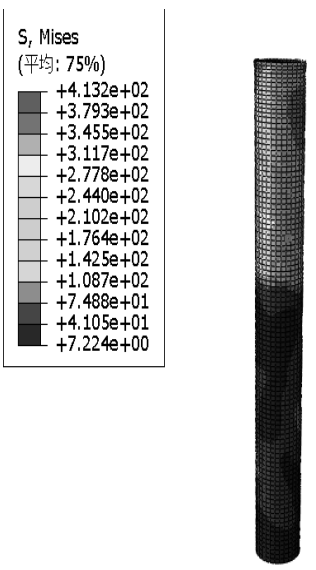

Figure 11 Thickness curve comparison

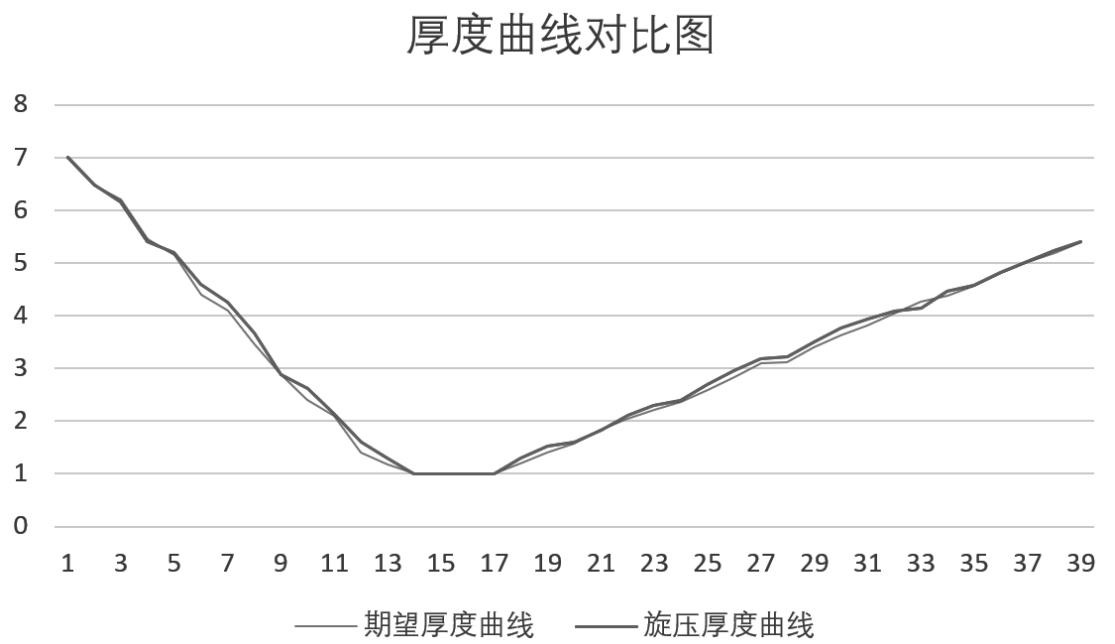

Figure 12 Wall thickness at contraction end

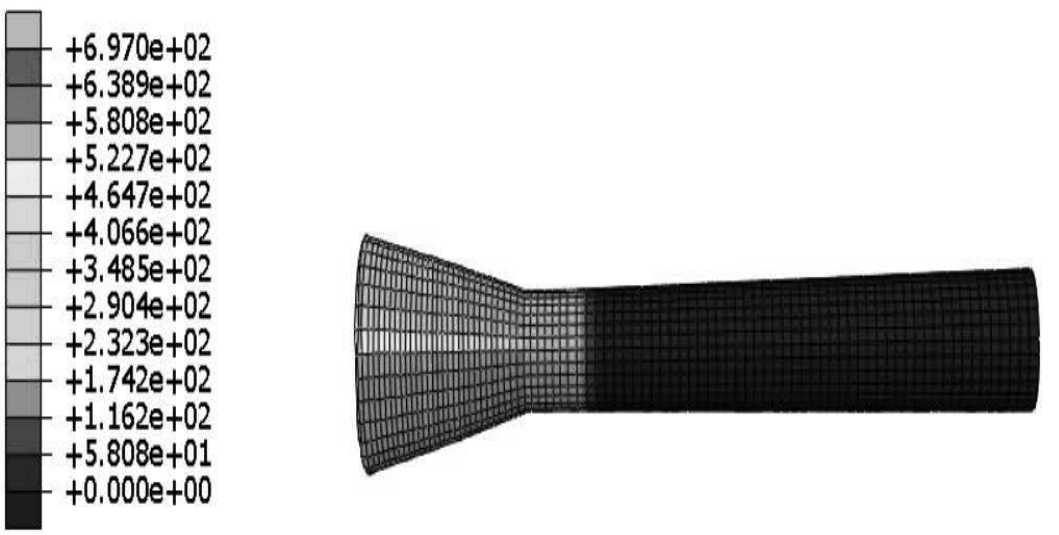

Figure 13 Wall thickness at expansion end

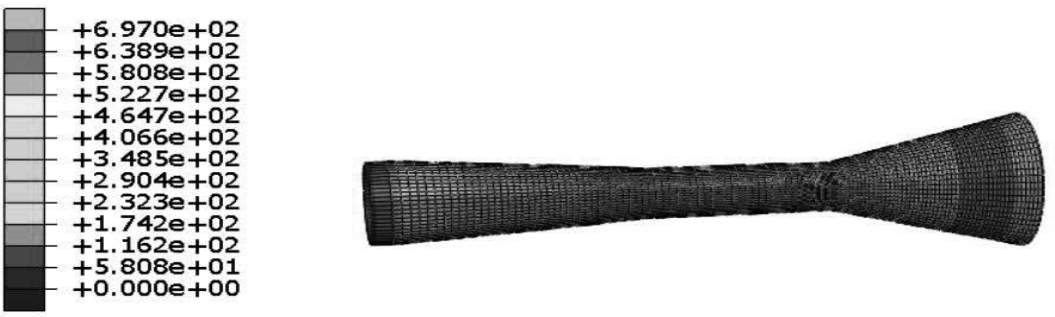

Figure 14 Wall thickness distribution of Laval tube after stamping

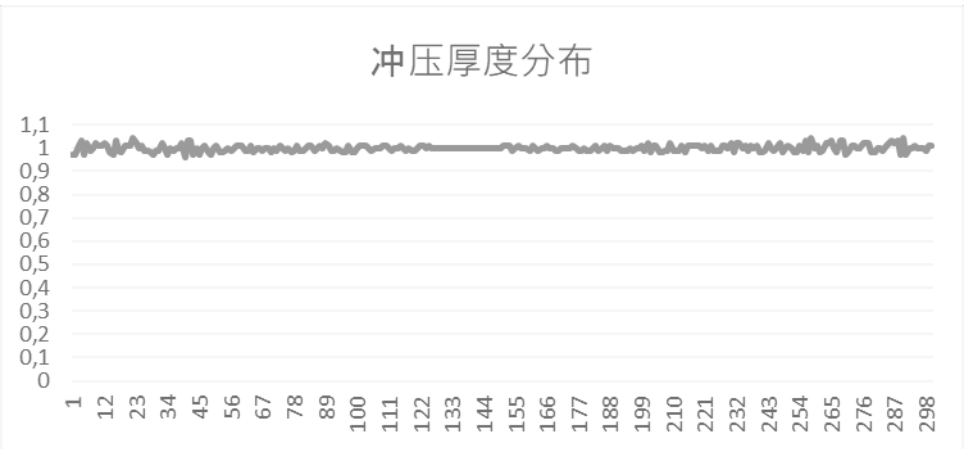

Figure 15 Model settings and initialization settings

Figure 16 Velocity cloud diagram at 0.8MPa

Figure 17 13 0.8MPa pressure cloud diagram

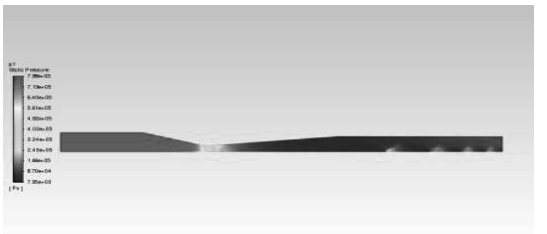

Figure 18 Density cloud map at 0.8MPa

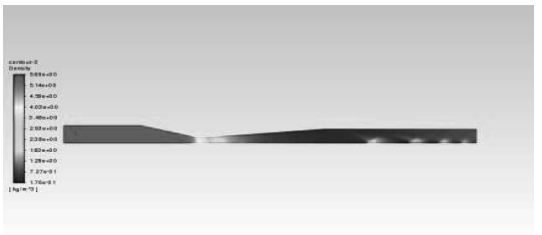

Figure 19 Temperature cloud diagram at 0.8MPa

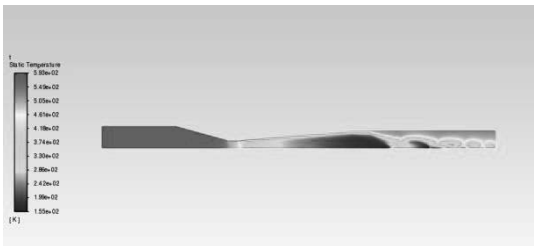

Figure 20 Velocity cloud diagram at 1.2MPa

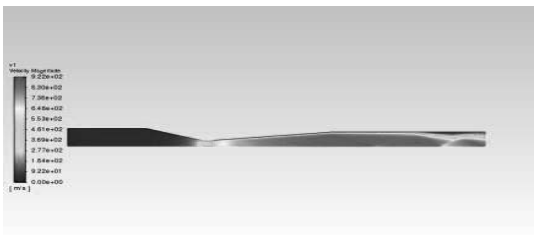

Figure 21 1.2MPa pressure cloud diagram

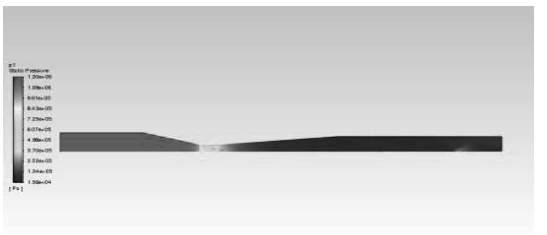

Figure 22 Density cloud map at 1.2MPa

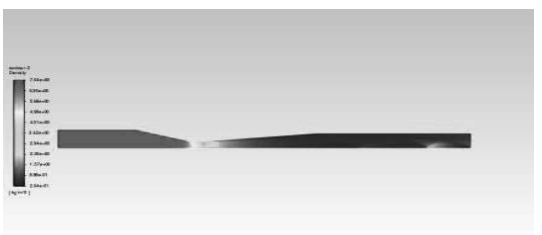

Figure 23 Temperature cloud diagram at 1.2MPa

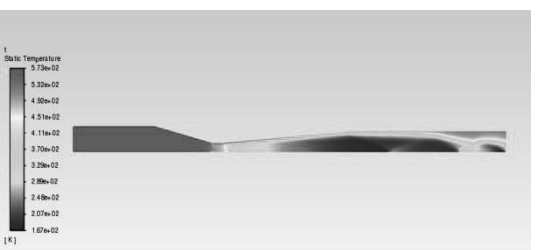

TalentDetector
26th September 2025
Gliwice, Poland
FACULTY OF MECHANICAL ENGINEERING
SILESIAN UNIVERSITY OF TECHNOLOGY
INTERNATIONAL STUDENTS SCIENTIFIC CONFERENCE

Mechanical Structure Design for Continuous Fiber-Reinforced FDM 3D Printing System

Qiankun Zhang, Zibo Zhou, Yize Zhao

Yanshan University of Technology, Faculty of Mechanical Engineering

Abstract: 3D printing technology is an additive manufacturing method that is different from traditional processing, which has the advantages of high material utilization, convenient processing of various complex parts, and fast processing speed, but because its printing materials are often nylon, PLA materials, etc., the printed parts cannot bear too much load, and the manufactured parts cannot meet the actual production and processing needs. The new continuous fiber is a material that has attracted much attention at present, with many advantages, such as high strength, low density, high temperature resistance, corrosion resistance, etc., and is widely used in various countries and fields around the world, especially in industrial manufacturing fields such as aerospace. If 3D printing technology is combined with new continuous fibers, it is possible to quickly and accurately manufacture molded parts that conform to the material, which has high engineering application value.
In this paper, a new printer is designed to improve the strength of prints by using fused deposition modeling (FDM technology) and using new continuous fiber as the material (carbon fiber is used as the experimental material in this design). The focus of this design is on the mechanical structure design of the new 3D printer. Including extruder structure design, transmission design and frame design.

Keywords: materials, laser treatment, polymers

1. INTRODUCTION

As an additive manufacturing technology, 3D printing is widely used in industrial, medical, and other fields due to its advantages of high material utilization, easy processing of complex parts, and fast speed. It not only reduces carbon emissions in traditional manufacturing but also reduces material waste and improves living standards. However, this technology has the shortcoming of insufficient strength of printed parts. Common materials such as nylon and PLA are difficult to bear large loads and cannot meet production needs.

The new continuous fiber has high strength, low density, resistance to high and low temperatures, and corrosion. It is widely used in aerospace and other fields. Combining it with 3D printing can quickly manufacture high-strength molded parts, which has great engineering value. The existing FDM process uses dual nozzles to extrude filaments and then combines them for printing: one nozzle extrudes continuous fibers, and the other extrudes molten

materials, which are attached after heating. However, the formed parts have obvious delamination. Therefore, this paper designs a device that can real-time mix deposition materials and continuous fibers and extrude the mixed materials to attach to the build platform, so as to solve the delamination problem and improve the quality of printed parts.

2. RESEARCH DESCRIPTION

2.1 Research Objectives

Based on the existing FDM 3D printer technology, a new printer adapted to the UM-style box structure is developed using new continuous fibers and common materials such as PLA. The core is to design a nozzle extrusion system that can real-time mix fibers and deposition materials without preprocessing the fibers. The uniform fusion of materials is achieved through synchronous wire feeding by dual friction wheels (the fiber wheel is made of rubber to enhance friction).

The printer needs to meet the following requirements: the maximum speed in the XY direction is 200mm/s, the positioning accuracy of the motion axis (including the Z-axis) is ±0.01mm, the layer thickness is 0.1-0.4mm, and the printing space is 500mm×500mm×500mm. The overall structure draws on the existing FDM mechanical design, with a focus on optimizing the nozzle extruder and three-axis transmission system. The nozzle integrates a real-time mixing mechanism and a shearing component to ensure material fusion and printing continuity. The three-axis transmission adopts high-precision optical axes, synchronous belts, and lead screws to ensure stability under high-speed movement.

This design breaks through the limitations of traditional dual-nozzle delamination, improves the strength of printed parts while simplifying the process, and provides an efficient solution for high-strength composite material printing.

2.2 Design of Extruder Nozzle

The focus of this nozzle design is on the extruder system, which also includes other components such as the shearing mechanism.

2.2.1 Extruder Mechanism

The extruder mechanism adopts short-range extrusion for wire feeding. The main friction wheel is fixedly installed on the motor shaft, and the auxiliary friction wheel is connected to the extruder frame with a spring and a wrench (see Figure 2-1). As shown in Figure 2-2, when not in operation, the spring stretches to make the two wheels fit; when preparing, press the wrench to compress the spring, and the frame drives the auxiliary friction wheel to rotate about 30° to form a gap larger than the diameter of the filament (1.75mm). After inserting the filament, release the wrench, and the spring retracts to make the two wheels clamp the filament. The stepper motor drives the main friction wheel to rotate, and the filament is fed into the throat by friction.

On the basis of the short-range extruder, two sets of friction wheels are designed, and the main friction wheels are connected coaxially to ensure that the instantaneous filament output of PLA and continuous fiber is consistent. Since the unpreprocessed continuous fiber filament is thin (about 0.1mm), the friction of ordinary friction wheels is insufficient. Therefore, the friction wheel for feeding fibers adopts a rubber wheel. When not in operation, the two wheels are in close contact, and the preparation operation is the same as above.

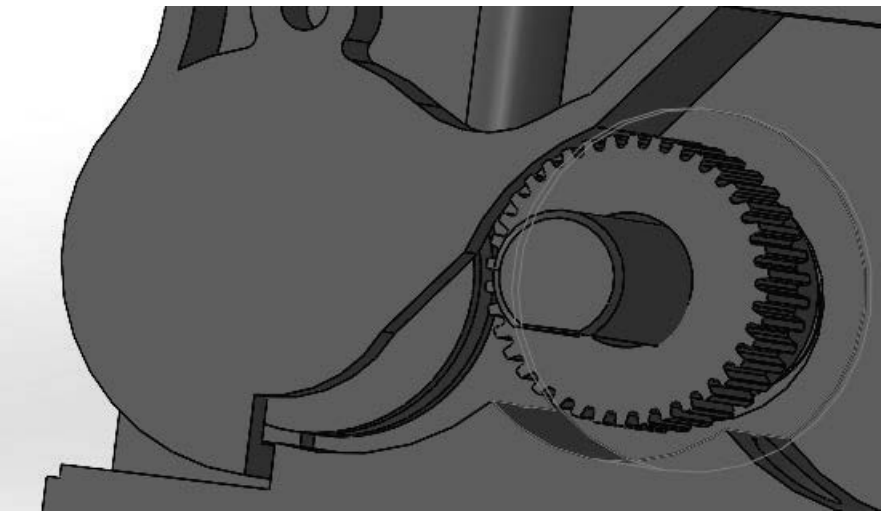

Figure 2-1. Main friction wheel and auxiliary friction wheel diagram

Figure 2-2. Schematic diagram of the extruder model

Selection of Extruder Motor:

In the design of the extruder mechanism, the most important factor is the printing speed of the printer, followed by the friction force generated during filament conveying and the mechanical structure of the extruder.

In this new continuous fiber FDM 3D printer, the average printing speed v should not be less than 50mm/s, and the maximum printing speed v_{max} should not be greater than 200mm/s.

1)The power required for the extruder motor is calculated as follows:

$$P_d=\frac{p_w}{\eta}=\frac{28.23}{0.85}=33.21W \tag{2-1}$$

Where, P_W — power required by the extruder:

η— efficiency from the motor to the extruder;

The working power required by the extruder can be calculated according to the working resistance and motion parameters:

$$P_w=\frac{F_{w\times v_w}}{\eta_W}=\frac{120\times0.2}{0.8501}=28.23W \quad (2\text{-}2)$$

Where, F_W—resistance of the extruder (N);
v_w—speed of the extruder (m/s);
η_w—efficiency of the working machine.

2) Required rotational speed of the motor
The working rotational speed of the main friction wheel is:

$$n=\frac{60\times1000v}{\pi\times d}=\frac{60\times1000\times0.1}{\pi\times6}318.3r/min \quad (2\text{-}3)$$

According to the working conditions and calculation, the selected motor parameters are as shown in Table 2-1.

Table 2-1. Main parameters of the selected motor

Motor Model	Rated Power (W)	Rotational Speed (r/min)
42 stepper motor	50	1000

2.2.2 Design and Selection of Shearing Mechanism and Other Components

The shearing mechanism is composed of a micro stepper motor lead screw slider set and a small blade, which is used to cut off the continuous fiber in time when the Z-axis is lifting, ensuring the accuracy of subsequent printing. Figure 2-3 shows the drawing of the selected micro stepper motor lead screw slider set.

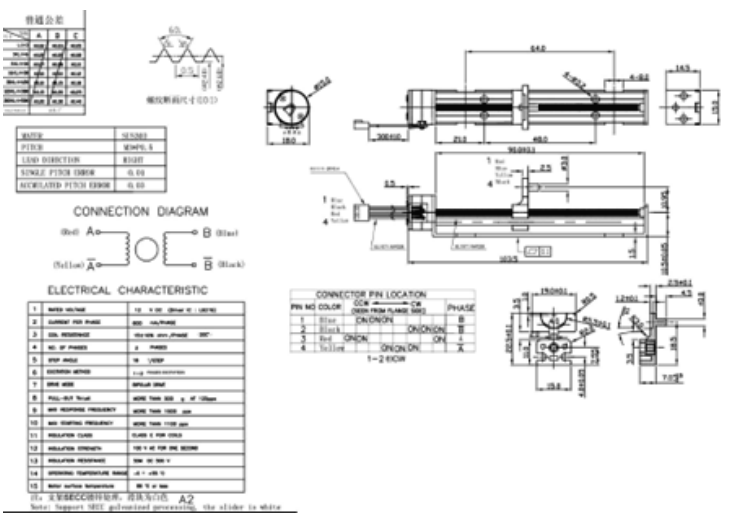

Figure 2-3. Micro stepper motor lead screw slider set

Design and selection of other components:

Heating rod: A low-power heating rod is used to heat the nozzle, and the heated bed is heated with a 1Ω resistance wire using 12V DC power.

Nozzle: A brass nozzle with a diameter of 0.4mm is selected to meet the requirements of size and material heat resistance.

Heating block: An aluminum heating block is used to reduce weight and load.

Throat: It is mainly made of aluminum alloy, with a Teflon hose added inside to prevent material adhesion, resist high temperature and corrosion, and improve printing quality.

Fan: A fan with a size of 30×30×10mm, voltage of 5V, power of 0.25W, and weight of 8g is selected to dissipate heat for the throat.

2.3 Design of Three-Axis Transmission System

2.3.1 Z-Axis Transmission System

The Z-axis transmission system converts rotational motion into linear motion through a lead screw to drive the heated bed to lift. The core of its design is the selection of the lead screw.

The axial load of the Z-axis is only the printer's heated bed, which is low. Selecting a T8 lead screw and two 8mm optical axes as guide rails is more than sufficient. In addition, an anti-backlash nut can be selected to eliminate the backlash of the lead screw. The selection of the anti-backlash nut is as shown in Table 2-2.

Table 2-2. Selection of anti-backlash nut

Model	Thread	Inner Diameter (mm)	Pitch (mm)	Lead (mm)
T8	T-type	8	2	2

The printing height in the Z-axis direction is 500mm, and the length of the nozzle system is about 12mm. A sufficient working height L1 of the workbench should be 512mm. In addition, for the assembly of the lead screw and the printer's heated bed, a certain margin should be left. The margin L2 for the lead screw is about 118mm, and the margin for the optical axis is about 148mm. Therefore, the length L of the lead screw is calculated as:

$$L = L_1 + L_2 = 630mm \tag{2-4}$$

$$L = L_1 + L_2 = 660mm \tag{2-5}$$

From the above, the diameter of the lead screw is 8mm, the length is 630mm, and the optical axis slide rail is about 660mm with a diameter of 8mm.

Design and selection of other parts:

1. Vertical pillow block bearing

The vertical bearing is used to install the X and Y optical axes on the aluminum profile. Therefore, the bearing should be selected according to the X and Y optical axes. The diameter of both X and Y optical axes is 8mm, so a vertical bearing with an inner diameter of 8mm should be selected. Table 4-3 shows the key parameters of the selected vertical pillow block bearing. Figure 2-4 shows the schematic diagram of the selected vertical pillow block bearing.

Table 4-3. Key parameters of vertical pillow block bearing

H	L	J	A2	N	H1	H2	B	Bolt
16	55	42	12	.5	5	30	12	M5

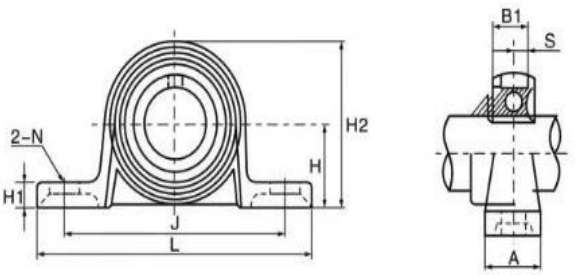

Figure 2-4. Drawing of vertical pillow block bearing

2. DESIGN OF Z-AXIS CONNECTING PLATE

The Z-axis connecting plate is mainly used to connect the Z-axis optical axis and the lead screw, and is made of acrylic plate. The two holes with a diameter of 15mm on the left and right are assembled with extended linear flange bearings, and 4mm hexagon socket cap screws are used to connect the extended linear flange bearings to the connecting plate. The inner diameter of the extended linear flange bearing is 8mm, which is assembled with the optical axis. There is one such hole on each side. The two optical axes and the lead screw act as slide rails. The small holes with a diameter of 3.3mm around are through holes, and the connecting plate is assembled with 1020 aluminum profiles through 3mm hexagon socket screws and profile nuts. The hole with a diameter of 8mm in the center is assembled with the lead screw. The design dimensions of the connecting plate are shown in Figure 2-5.

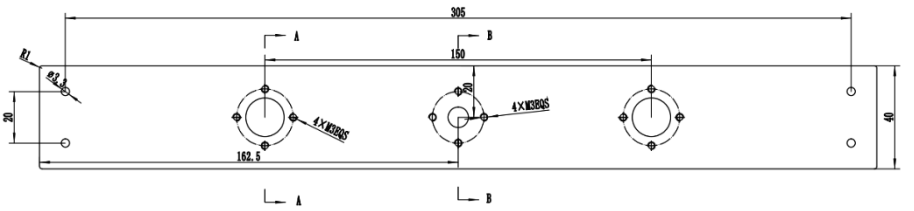

Figure 2-5: Partial design dimensions of the Z-axis connecting plate

2.3.2 Design of XY-Axis Transmission System

The XY-axis transmission system realizes the movement of the nozzle in the x and y directions through belt transmission, and its core design is the selection and calculation of the xy-axis optical axes and belts.

X-axis

(1) Length calculation: The assembly length with the vertical pillow block bearing is 20mm (one at each end), the assembly dimension of the synchronous belt is 16mm (one at each end), the movement distance of the slider is 540mm (including 40mm of the slider itself), and the movement margin is 78mm. The total length = 2×20 + 2×16 + 540 + 78 = 690mm.

(2) Shaft diameter selection and strength check: As shown in Figure 2-6, an 8mm chrome-plated stainless steel optical axis is used. The X-axis bears the total weight of the nozzle system and the cross slider, which is about 1.5kg, simplified as a uniformly distributed load.

Bending moment calculation: The maximum bending moment occurs at the midpoint of the optical axis, and the calculation formula is Mmax=Fl/4 (F is the load, l is the shaft length)

F=1.5kg×9.8N/kg=14.7N Mmax=14.7N×0.69m/4≈2.52N·m

Strength check: The section modulus of resistance to bending of the 8mm stainless steel optical axis $W=\pi d^3/32\approx\pi\times8^3/32\approx50.27mm^3$

Bending stress $\sigma=Mmax/W\approx2.52\times10^3N\cdot mm/50.27mm^3\approx50.1MPa$

The yield strength of stainless steel is ≥200MPa, and the safety factor is ≥4, which meets the strength requirements.

Figure 2-6. Bending moment diagram of the simplified force model of the X-axis optical axis

(3) Material selection: Chrome-plated stainless steel is wear-resistant, with a straightness error of ≤0.05mm/m, ensuring stable movement.

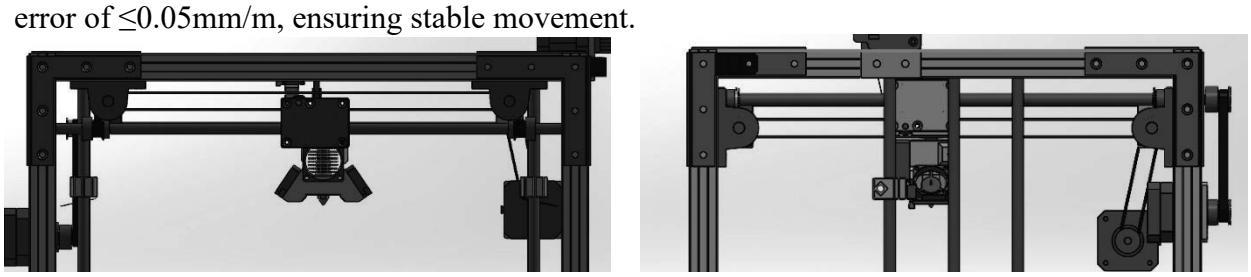

(a) (b)

Figure 2-7. Schematic diagram (a) X-axis (b) Y-axis

Y-axis

(1) Length calculation:

Short axis: Assembly with vertical pillow block bearings is 20mm×2, assembly with synchronous belts is 16mm×2, the movement distance of the slider is 540mm, and the margin is 28mm. Total length = 2×20 + 2×16 + 540 + 28 = 640mm.

Long axis: Adding a 20mm section connected to the synchronous pulley, the total length = 640 + 20 = 660mm.

(2) Shaft diameter selection: As shown in Figure 2-7, the optical axis bears a vertical load of 15N and a horizontal tension of 10N.

Calculation of support reaction: 10.7N at point A and 14.3N at point B (obtained through the moment balance equation).

The maximum bending moment Mmax≈1.8N · m, which is less than that of the X-axis. The bending stress σ≈35.8MPa, and the safety factor is ≥5.6.

Force analysis: In the simplified model, the reaction force at point A is 10.7N, and at point B is 14.3N. The maximum bending moment is less than that of the X-axis, so the 8mm shaft diameter is safe.

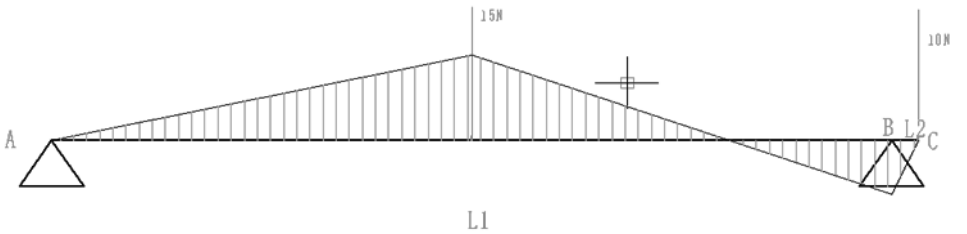

Figure 2-8. Bending moment diagram of the 660mm Y-axis optical axis

Calculation of synchronous belt transmission

1. Calculation and selection of the number of teeth: To ensure stable and accurate transmission, the synchronous belt and pulley must mesh with at least 6 teeth, so the number of teeth must be ≥12. Considering the need to reduce the step length to improve surface quality, 20 teeth are selected.

2. Calculation of force and motion parameters:

Slider friction resistance: f = μmg=0.002×1.2×9.8=0.024N

Tension provided by the motor: F=M/L=0.5/(5×10^{-3})=100N

Acceleration provided by the motor: a=F/m=100/1.2≈83m/s²

Slider deceleration distance (initial speed v0=0.09m/s): s=v0²/(2a)=0.09²/(2×83)≈0.049mm

3. Determination of synchronous belt parameters:

Model: HTD series circular-arc tooth synchronous belt, pitch P=3mm, number of teeth Z=20

Pitch circle diameter: d=pz/π=3×20/π≈17.20mm

Safety check: When the printing speed is 90mm/s, the motor rotational speed n=v/(Pz)=5.4/(3×20×10^{-3})≈90r/min≈1.5r/s≤3r/s, which is qualified.

4. Calculation of synchronous belt length:

X-axis: L1=2a1+pz=2×566+3×20=1182mm

Y-axis: L2=2a2+pz=2×569.3+3×20=1198.6mm

The width of both belts is 6mm.

5. Selection of motor connection belt: 6mm wide 200mm and 300mm closed-loop synchronous belts are used to match the connection between the motor and the shaft, reducing costs.

3. DESCRIPTION OF RESEARCH RESULITS

3.1 Design Results of Nozzle System

A real-time mixing nozzle system without fiber preprocessing is designed, which adopts short-range extrusion. Synchronous wire feeding through two sets of friction wheels (the fiber wheel is a rubber wheel) ensures that the instantaneous filament output of PLA and fiber is consistent, solving the problem of insufficient friction due to too thin fibers. The selection of components such as heating rods and nozzles is reasonable, meeting the requirements of heating, heat dissipation, and anti-adhesion, ensuring sufficient melting and mixing of materials. The shearing mechanism can cut off fibers in time during Z-axis movement, ensuring continuous and accurate printing. The total weight of the nozzle system is ≤700g, effectively controlling the transmission load.

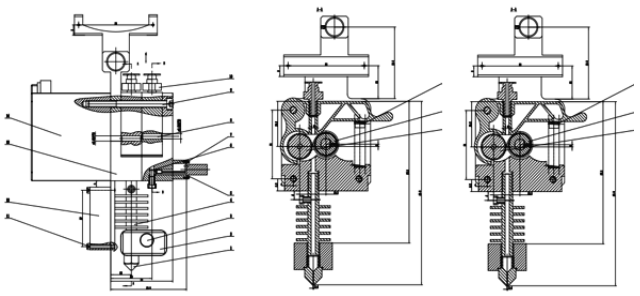

Figure 3-1. Nozzle system

3.2 Design Results of Three-Axis Transmission System

The X-axis optical axis is 690mm long, the two Y-axis optical axes are 640mm and 660mm long, the Z-axis lead screw is 630mm long, and the optical axis is 660mm long. All are 8mm diameter chrome-plated stainless steel, which can bear bending stress and load. The synchronous belt is H series circular-arc tooth, with 20 teeth, lengths of 1182mm and 1198.6mm, and a width of 6mm, ensuring synchronous and stable transmission and reducing vibration errors. The cross-axis X-axis is 590mm long, the Y-axis is 586mm long, with a shaft diameter of 8mm, and the strength is qualified. The selection of vertical pillow block bearings and Z-axis connecting plates is reasonable, ensuring assembly accuracy and stability.

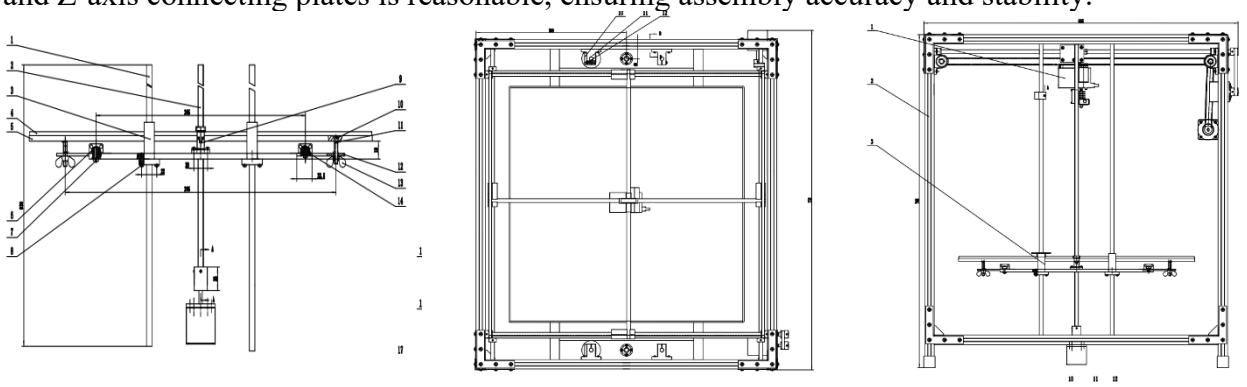

(a) *Z-axis transmission system* (b) *XY-axis transmission system* (c) *Three-axis transmission system*

Figure 3-2. transmission system

3.3 Performance Verification Results

The printing space is 500mm×500mm×500mm, the maximum XY speed is 200mm/s, the positioning accuracy is ±0.01mm, the Z-axis accuracy is ±0.01mm, and the layer thickness is 0.1-0.4mm. The maximum heating temperature of the printing platform is 100℃, and the power supply is 220VAC, which meets the standards. The strength of printed parts is 3-5 times that of ordinary FDM, and the efficiency is not lower than that of similar models, meeting the needs of industrial high-strength parts.

4. SUMMARY

This paper focuses on the structural design of a new continuous fiber FDM 3D printer, aiming to solve the problems of insufficient strength of ordinary FDM printed parts and delamination of traditional dual nozzles. At the initial stage of the research, the technical status was analyzed, and the goal of designing a new printer with real-time material mixing was clarified.

After comparing the overall structure options, the UM-style structure was selected for its stability, stable transmission, and high space utilization. The core design focuses on the extruder nozzle system and three-axis transmission system: the nozzle adopts short-range extrusion and dual friction wheels (rubber wheels for fibers) for synchronous wire feeding, realizing real-time mixing of fibers and PLA without fiber preprocessing, simplifying the process. The supporting shearing mechanism ensures printing continuity, and the reasonable selection of components controls the total weight. The three-axis transmission system accurately calculates the sizes of X, Y-axis optical axes and Z-axis lead screws, uses chrome-plated stainless steel, and the synchronous belt is H series circular-arc tooth, ensuring a positioning accuracy of ±0.01mm, a speed of 200mm/s, and meeting the 500mm³ printing space requirement.

Performance verification and economic analysis show that the strength of printed parts reaches 3-5 times that of ordinary parts, with moderate cost, indicating industrial application potential. In conclusion, this research completes the structural design of a new printer, providing a feasible solution for high-strength part manufacturing.

5. CONCLUSION

This paper successfully designs a new continuous fiber FDM 3D printer that can real-time mix continuous fibers and deposition materials, solving the delamination problem of traditional dual-nozzle technology and significantly improving the strength of printed parts (reaching 3-5 times that of ordinary FDM parts).

Structurally, it is based on the UM-style. The nozzle adopts short-range extrusion and dual friction wheels for synchronous wire feeding, without fiber preprocessing, simplifying the process and reducing costs. The parameters of the three-axis transmission system are reasonable, meeting the requirements of 500mm×500mm×500mm printing space, 200mm/s maximum speed, and ±0.01mm positioning accuracy.

Economic analysis shows moderate cost and market competitiveness. However, the structure and material compatibility still need to be optimized. Future improvements can further enhance performance, providing a new way for manufacturing industrial complex high-strength parts.

BIBLIOGRAPHY

1. B. Kromoser, P. Preinstorfer, J. Kollegger, Building lightweight structures with carbon-fiber-reinforced polymer-reinforced ultra-high-performance concrete: research approach, construction materials, and conceptual design of three building components, Struct. Concr. 20 (2) (2019) 730–744.
2. W. Zhu, J. Li, H. Du, Z. Yao, M. Lv, Y. Xu, Influence of material properties and structural parameters on the performance of near-space use lightweight insulation structure, Appl. Therm. Eng. 124 (2017) 432–441.
3. C. Schneider, M.N. Velea, S. Kazemahvazi, D. Zenkert, Compression properties of novel thermoplastic carbon fibre and poly-ethylene terephthalate fibre composite lattice structures, Mater. Des. 65 (2015) 1110–1120.
4. Q. Wu, L. Ma, L. Wu, J. Xiong, A novel strengthening method for carbon fiber composite lattice truss structures, Compos. Struct. 153 (2016) 585–592.
5. J. Xu, Y. Wu, X. Gao, H. Wu, S. Nutt, S. Yin, Design of composite lattice materials combined with fabrication approaches, J. Compos. Mater. 53 (3) (2018) 393–404.
6. H. Luo, F. Chen, F. Wang, X. Wang, W. Dai, S. Hu, R. Gong, Preparation and microwave absorption properties of honeycomb core structures coated with composite absorber, AIP Adv. 8 (5) (2018), 056635.
7. J.M. Chacon, M.A. Caminero, P.J. Nunez, E. Garcia-Plaza, I. Garcia-Moreno, J. M. Reverte, Additive manufacturing of continuous fibre reinforced thermoplastic composites using fused deposition modelling: effect of process parameters on mechanical properties, Compos. Sci. Technol. 181 (Sep.8) (2019), 107688. P. Cheng, Y. Peng, K. Wang, Y.-Q. Wang, C. Chen, Study on intralaminar crack propagation mechanisms in single- and multi-layer 2D woven composite laminate, Mech. Adv. Mater. Struct. (2021) 1–11.
8. F. Quadrini, E. Squeo, Injection molding of bushes made of tribological PEEK composites, Express Polym. Lett. 1 (2007) 817–823.
9. B.G. Compton, J.A. Lewis, 3D-Printing of lightweight cellular composites, Adv. Mater. 26 (34) (2014) 5930–5935.

TalentDetector

26th September 2025
Gliwice, Poland

FACULTY OF MECHANICAL ENGINEERING
SILESIAN UNIVERSITY OF TECHNOLOGY

INTERNATIONAL STUDENTS SCIENTIFIC CONFERENCE

Analysis on Faults and Diagnostic Technologies of Mechanical Hydraulic Transmission Systems

Zhuge Shao, Yanchao Hao, Jingkun Zhou

Yanshan University, Faculty of Mechanical Engineering, Department of Mechatronic Control Engineering.
email: 2279156392@qq.com

Abstract: As a core power transmission device in fields such as construction machinery, automobiles, and aerospace, the mechanical hydraulic transmission system realizes power transmission through hydraulic energy conversion. Its stable operation relies on the coordinated work of key components such as hydraulic pumps and control valves. However, due to long-term use wear and harsh working environments (such as high temperature, dust, and vibration), the system is prone to various faults, which seriously restrict the operation efficiency and safety of equipment. To identify and solve faults in a timely manner, this paper systematically sorts out the core diagnostic methods of mechanical hydraulic transmission systems, including the observation diagnosis method for identifying leaks and abnormal noises through intuitive observation, the instrument diagnosis method for obtaining accurate data with professional equipment, the component replacement method for locating fault sources by replacing components, and the regular inspection method for troubleshooting hidden dangers periodically. At the same time, it elaborates on practical diagnostic and treatment technologies in detail, covering hydraulic oil quality detection (viscosity and moisture analysis), pressure testing (static and dynamic measurement), leak detection (application of tools such as fluorescent dyes), function verification of valves and governors, as well as filter element inspection and replacement. The organic combination of these methods and technologies can help engineering and technical personnel quickly locate the root cause of faults and solve problems efficiently, which is of great significance for improving the reliability and safety of mechanical hydraulic transmission systems and extending the service life of equipment.

Keywords: Mechanical Hydraulic Transmission System; Fault Diagnosis Method; Hydraulic Oil Quality Detection; Pressure Testing; Leak Detection

1. OVERVIEW OF MECHANICAL HYDRAULIC TRANSMISSION SYSTEMS

The mechanical hydraulic transmission system is essential in modern engineering, widely used in construction machinery (excavator slewing mechanism, crane luffing cylinder), automotive industry (hydraulic braking, automatic transmission) and aerospace (aircraft landing gear hydraulic control, engine fuel hydraulic control). Its core working mechanism is "energy

conversion": hydraulic pump converts prime mover (motor/engine) mechanical energy into high-pressure hydraulic oil pressure energy; high-pressure oil is transported to executive components (hydraulic motor/cylinder) via closed pipelines, which convert pressure energy back to mechanical energy to drive mechanical parts for rotation, expansion, lifting, etc.

It has advantages like high power density, smooth operation and flexible regulation, but its performance depends on multi-component coordination. Core components include: power components (hydraulic pumps like gear pumps, piston pumps), executive components (hydraulic motors for rotation, cylinders for linear movement), control components (control valves like directional, pressure, flow valves; governors like speed control valves) and auxiliary components (oil tanks, filter elements, seals, pressure gauges/flow meters).

2. FAULT DIAGNOSIS METHODS OF MECHANICAL HYDRAULIC TRANSMISSION SYSTEMS

2.1.Observation Diagnosis Method

This basic method relies on intuition to initially locate fault areas and causes by observing system operation, component dynamics and abnormalities, without complex equipment, suitable for on-site rapid troubleshooting.

Check if executive components (hydraulic cylinder expansion, motor rotation) move smoothly, with no jamming, delay or incoordination (e.g., slow excavator bucket lifting with "strain" may indicate power/control component issues); focus on hydraulic pump, control valve, pipeline joints to check for oil leaks (aging seals, loose joints), abnormal noises (pump "buzzing" for internal wear, "sharp scream" for air/impurities) and component overheating (obvious temperature difference without burns may mean poor oil circulation); check if pressure gauge pointer is stable in design range (rated 150-250 bar; continuous below 150 bar or violent fluctuation is abnormal), flow meter speed is normal (sudden drop may mean pipeline blockage) and thermometer reading is within oil allowable temperature (≤60°C; overheating causes oil oxidation).

2.2. Instrument Diagnosis Method

This method uses professional testing equipment to accurately collect system parameters (pressure, flow, temperature) and judge faults by comparing with design standards, featuring "dataization" and "precision" to locate hidden faults.

2.2.1 Pressure Detection (Pressure Gauge/Pressure Sensor)

Pressure is a core parameter, measured by pressure gauge (range covering rated pressure, e.g., 0-400 bar) or sensor. System static pressure (shutdown) lower than design value may be due to pump internal leakage, pipeline rupture or seal leakage; dynamic pressure (operation) sharply exceeding rated value may be due to control valve jamming (e.g., relief valve failure) or pipeline blockage.

2.2.2 Flow Detection (Flow Meter)

Flow affects executive component speed, measured by flow meter for pump displacement and cylinder oil intake. Pump displacement below rated value may be due to internal rotor wear

or blade jamming; insufficient cylinder flow may be due to pipeline blockage (filter element blockage) or improper flow valve adjustment. Flow tracking locates blockages (e.g., normal pump outlet flow but insufficient cylinder inlet flow means pipeline/filter element blockage).

2.2.3 Temperature Detection (Thermometer/Temperature Sensor)

The system generates heat during operation; excessive temperature reduces oil viscosity and ages seals, monitored by thermometer. Oil temperature in tank over 60°C may be due to cooling system fault (radiator blockage), insufficient oil or pump/motor internal leakage (energy loss as heat); local component (e.g., control valve) temperature much higher than others may be due to valve core jamming causing local throttling heating.

2.3 Component Replacement Method

This method locates fault sources by replacing suspected faulty components (pump, motor, control valve) and observing if faults are eliminated, suitable for "single-component fault causing system abnormalities". Understand component functions and principles before operation.

Narrow suspected component scope by symptoms (e.g., insufficient equipment walking power: first check hydraulic pump; if normal via pressure gauge, replace motor and cylinder in sequence); replace one component at a time, test after replacement and record (e.g., power recovery after motor replacement means motor fault); shut down and depressurize the system during replacement to prevent oil spraying injury, retain original components for later disassembly analysis, and prioritize replacing low-cost vulnerable parts (valve cores, seals) over high-cost ones (pump).

2.4 Regular Inspection Method

Based on "prevention first", this method formulates standardized inspection plans to periodically check potential faults, reducing sudden faults, with core "regularity" and "comprehensiveness".

2.4.1 Setting of Inspection Cycles

Adjust cycles by equipment use frequency and environment: high-intensity use (comprehensive inspection every 3 months), medium-intensity (every 6 months), low-intensity (simple monthly, comprehensive every 2 months), harsh environment (more frequent as needed).

2.4.2 Core Inspection Items

During the inspection, there are four main core inspection items, namely oil condition, sealing and leakage, component wear, and auxiliary components.

Among them,check oil appearance (clear light yellow normal; turbid, black or precipitated needs replacement) and level (between tank scale lines; supplement same model if insufficient).

For sealing and leakage,check pipeline joints and seals (O-rings) for leakage; disassemble to check seal aging if oil stains are found.

For component wear, it is mainly to check the shaft end seals of the hydraulic pump/motor and the surface of the hydraulic cylinder piston rod (whether there are scratches or rust, which can easily cause damage to the seals).

For auxiliary components, it is necessary to clean the oil tank filter screen, check the filter element pressure difference (if the pressure difference exceeds 0.3 MPa, it needs to be replaced), and verify the accuracy of the pressure gauge/flow meter.

2.4.3 Inspection Records and Maintenance

Record parameters (oil viscosity, pressure, filter element pressure difference) during each inspection to form a system operation ledger; judge system trend by comparing historical data (e.g., increasing filter element pressure difference needs pollution source investigation); maintain based on results (replace aging seals, clean blocked pipelines, supplement oil).

3. DIAGNOSTIC AND TREATMENT TECHNOLOGIES FOR FAULTS OF MECHANICAL HYDRAULIC TRANSMISSION SYSTEMS

3.1 Hydraulic Oil Quality Detection

Hydraulic oil is the "blood" of the system, with quality affecting service life, detected from appearance, viscosity and moisture.

3.1.1 Appearance Detection

Normal oil is clear, transparent and light yellow; abnormal oil (turbid with dust/metal debris, black from oxidation, stratified with moisture) must be replaced immediately, and tank/pipelines cleaned to avoid secondary pollution.

3.1.2 Viscosity Detection (Viscometer)

Viscosity determines oil fluidity and lubrication. Excessive viscosity increases pump oil suction resistance, causing cavitation (insufficient power, high energy consumption); insufficient viscosity fails to form enough oil film (severe component wear, increased internal leakage). Detection must comply with system oil viscosity grade (e.g., ISO VG46 oil: 41.4-50.6 mm^2/s at 40°C); replace if exceeding range.

3.1.3 Moisture Detection (Hygrometer)

Moisture is harmful to oil, causing emulsification (lubricity loss), metal rust (cylinder inner wall) and seal swelling (sealing performance reduction). Use a hygrometer to measure water content; if over 0.1% (volume ratio), dehydrate with an oil-water separator or replace oil.

3.2 Pressure Testing

Pressure testing follows "static-dynamic" steps to ensure normal system pressure regulation, with specific parameters in Table 1.

If insufficient pressure, operator should check pump internal leakage (disassemble to observe rotor wear), pipeline leakage (soapy water for bubbles), damaged seals (replace same model);If excessive pressure, operator should disassemble relief valve to clean valve core impurities (replace if worn), check pipeline blockage (unclog with compressed air).

Table 1

Testing Item	Technical Parameter	Judgment Standard
Pressure Measuring Instrument	Pressure gauge (range 0-400 bar, accuracy class 1.6)	The instrument must be calibrated, with an error $\leq \pm 1\%$
Static Pressure Test	Measured in the system shutdown state	The deviation between the pressure value and the designed static pressure $\leq 5\%$
Dynamic Pressure Test	The system operates at full load for 10 minutes continuously	Pressure fluctuation range $\leq \pm 5$ bar
Testing Pressure Range	0-300 bar (covering the rated system pressure of 150-250 bar)	No sudden pressure rise/drop

3.3 Leak Detection

Leakage is common, wasting oil and causing pressure drop/ slow executive components; locate leak points via "observation + tools".

3.3.1 Key Inspection Parts

The key inspection parts mainly include four types: pipeline joints, control valves, hydraulic cylinders, and oil tanks. The respective problems that are prone to occur are as follows:

Pipeline joints: Loose threads or aging gaskets (flange joint gasket deformation).

Control valves: Excessive valve core-sleeve clearance (internal leakage) or damaged valve cover seals (external leakage).

Hydraulic cylinders: Aging piston rod seals (dust rings, Y-rings) causing oil leakage.

Oil tanks: Poor tank cover sealing (air/dust mixing) or weld cracking (long-term vibration).

3.3.2 Detection Tools and Methods

Fluorescent dye method: Inject fluorescent dye into the system, and after operating for Fluorescent dye method: Inject dye, operate for 30 minutes, irradiate with ultraviolet lamp; leak points emit fluorescence (locates tiny leaks).

Pressure sensor method: Install sensors at pipeline key nodes; sharp pressure drop in a section means leakage (e.g., sensor 1:200 bar, sensor 2:180 bar - leak between them).

Soapy water method: Apply to suspected joints/flanges; bubbles indicate leakage (for external leakage).

3.3.3 Leak Treatment

External leakage: Replace aging seals (O-rings, gaskets), tighten joint threads (comply with torque standard). Internal leakage: Disassemble control valve/pump, grind valve core or replace worn components (pump distribution plate); replace the whole component if leakage is severe.

3.4 Valve and Governor Inspection

Valves (directional valves, pressure valves, flow valves) and governors (e.g., speed control valves) are the "control centers" of the system. Abnormalities in their functions will directly lead to action control failure, so they need to be inspected with emphasis.

3.4.1 Valve Inspection

Manually operate valves to check if valve cores move smoothly (no jamming; disassemble, clean and grease if jammed due to wear/impurities); close valves and measure inlet-outlet pressure difference (relief valve difference ≤90% of rated pressure means internal leakage - grind sealing surface or replace valve core); adjust pressure valves (relief valve) and check if pressure changes linearly with knobs (no response - check electromagnet fault for electric valves or spring break for manual valves).

3.4.2 Governor Inspection

Governors adjust executive component speed (cylinder expansion speed). Set governor output flow (e.g., 10 L/min), measure actual flow with a flow meter (deviation ≤ ±5%; adjust speed control valve core clearance or replace orifice if excessive); check governor inlet-outlet seals (replace if leaking to avoid adjustment failure); observe executive component speed stability (unstable - check for blocked damping hole, unclog with thin iron wire).

3.5 Filter Element Inspection and Replacement

Filter elements filter oil impurities (metal debris, dust) to protect precision components; blockage increases system pressure difference and reduces flow, requiring regular inspection and replacement.

3.5.1 Filter Element Inspection

Disassemble filter elements to check for obvious impurity accumulation (metal debris, oil sludge) or damage (filter paper tearing) - replace immediately if present; check filter element-filter seat sealing surface (rubber O-ring; replace if aging/deformed to avoid unfiltered oil bypass); measure inlet-outlet pressure difference with a differential pressure gauge (replace if over 0.3 MPa, even with no obvious surface impurities).

3.5.2 Precautions for Filter Element Replacement

Select filter elements matching system design (filtration accuracy, size, flow grade; e.g., 10μm required, not 20μm); shut down and depressurize the system during replacement to prevent oil spraying; ensure tight sealing between filter element and seat (no bypass), comply with torque standard when tightening bolts; run the system under no load for 5 minutes after replacement to discharge residual air/impurities, then conduct load test.

4. CONCLUSION

Fault diagnosis and treatment of mechanical hydraulic transmission systems are key links to ensure the stable operation of equipment, which need to combine "prevention" and "governance". A "four-in-one" diagnosis system is formed by using the observation diagnosis

method for rapid preliminary troubleshooting, the instrument diagnosis method for precise positioning, the component replacement method for verifying fault sources, and the regular inspection method for preventing hidden dangers. At the same time, relying on treatment technologies such as hydraulic oil quality detection, pressure testing, and leak detection, efficient fault resolution is realized.

In practical applications, it is necessary to flexibly combine diagnostic methods and treatment technologies according to the type of fault (such as external leakage, abnormal pressure, slow movement). For example, for "slow movement of executive components", the observation diagnosis method can be used first to check for leaks, then the instrument diagnosis method to detect pressure and flow rate, and finally the component replacement method to verify whether the hydraulic pump or motor is faulty. The methods and technologies sorted out in this paper can provide practical references for engineering and technical personnel, help improve the reliability and safety of mechanical hydraulic transmission systems, and promote the efficient operation of equipment in fields such as construction machinery, automobiles, and aerospace.

BIBLIOGRAPHY

1. Liu, Q. Y. (2023). Fault Analysis and Maintenance Scheme Research of Hydraulic Transmission System for Construction Machinery. Southern Agricultural Machinery, 54(24), 155-157+165.
2. Chen, M. X. (2023). Fault Diagnosis and Maintenance Research of Hydraulic Transmission System for Construction Machinery. Fluid Measurement and Control, 4(03), 61-63.
3. Zheng, S. Y. (2023). Fault Diagnosis and Elimination Countermeasures of Hydraulic Transmission System for Construction Machinery. Construction Mechanization, 44(03), 93-95.
4. Liu, J. (2023). Fault Diagnosis Analysis and Countermeasures of Hydraulic Transmission System. Mining Equipment, (01), 139-141.
5. Lü, Y. (2014). Analysis of Faults and Diagnostic Treatment Technologies of Mechanical Hydraulic Transmission Systems. Henan Science and Technology, (15), 98.